

NON-INVASIVE DETECTION OF PRE-MALIGNANT LESIONS USING SUB-  
ABLATIVE, DEEP ULTRAVIOLET LASER-TISSUE INTERACTIONS COUPLED WITH  
ENDOGENOUS TISSUE FLUORESCENCE: PROOF-OF-CONCEPT,  
COMPUTATIONAL MODELING, AND DETECTION-THEORY STRATEGIES FOR  
CLINICAL INSTRUMENT DESIGN AND TESTING

By

RAYMOND THOMAS KOZIKOWSKI, III

A DISSERTATION PRESENTED TO THE GRADUATE SCHOOL  
OF THE UNIVERSITY OF FLORIDA IN PARTIAL FULFILLMENT  
OF THE REQUIREMENTS FOR THE DEGREE OF  
DOCTOR OF PHILOSOPHY

UNIVERSITY OF FLORIDA

2012

© 2012 Raymond Kozikowski

To my parents and sister

## ACKNOWLEDGMENTS

I would like to take this opportunity to acknowledge and thanks those people that made this work possible. This undertaking was in no way a one-person effort and without the support and help of these people, none of this would have been possible.

First is my advisor, Dr. Brian Sorg. Even before coming to Florida, I heard great things about him, from his colleagues at Duke as well as other universities. His research vision, passion for his work, and his high level of regard in the research community were the preeminent factors in my decision to attend UF.

Second is Dr. David Hahn. Without his technical vision and his close collaborative relationship with Dr. Sorg, this work never would have materialized. Despite how busy he always was, there was always a little bit extra time he could find to provide critical help and guidance through my time here.

Additionally, a big thank you to my committee members Dr. Brandi Ormerod and Dr. Benjamin Keselowsky, for helping me to understand how to take the raw output of my research efforts and mold it into something more meaningful.

Without several key collaborators on this work, this project never would have materialized, including Sarah Smith, Jennifer Lee, Se-woon Choe, Dr. William Castleman, and Dr. Indraneel Bhattacharyya. Thanks for all of the extra effort, I could not have done it without all of you.

Finally, I would like to thank my family and friends: Mom, Dad, Teal, Lauren, Olive, Joon, Jeff, Craig, Flo, Wiley, and all of ATO Xi '06 (VTL guys!). Without their support and patience throughout the years, I never would have made it.

## TABLE OF CONTENTS

	<u>page</u>
ACKNOWLEDGMENTS.....	4
LIST OF TABLES.....	8
LIST OF FIGURES.....	9
LIST OF ABBREVIATIONS.....	12
ABSTRACT.....	14
CHAPTER	
1 INTRODUCTION.....	16
Motivation.....	16
Specific Aims.....	17
Background.....	18
Oral Epithelium Anatomy and Physiology.....	19
Progression to Malignancy.....	21
Oral Cancer Detection.....	23
Tissue Optics Fundamentals.....	26
Excimer Laser-Tissue Interactions.....	30
DLIPS: State of the Technology.....	32
DLIPS: A Signal-to-Noise Perspective.....	33
In vivo Optical Diagnostics: Problem Formalization.....	35
Experimental Outline.....	37
2 COMPARATIVE EVALUATION OF DIFFERENTIAL LASER-INDUCED PERTURBATION SPECTROSCOPY AS A TECHNIQUE TO DISCRIMINATE EMERGING SKIN PATHOLOGY.....	47
Motivation.....	47
Materials & Methods.....	51
DLIPS System.....	51
Chemical Initiation and Promotion of Mouse Skin Tumors.....	53
Histopathology.....	53
Collection of DLIPS and Fluorescence Spectra.....	54
Multivariate Statistical Analysis.....	55
Detection Theory Analysis of Classification Performance.....	56
Results.....	58
Histopathology.....	58
DLIPS and Laser-Induced Fluorescence Spectra.....	59
Multivariate Statistical Analysis.....	60
Pathology Detection Performance.....	62

Discussion .....	64
<b>3 DLIPS SPECTRA OF ORAL MUCOSA PATHOLOGY: MONTE CARLO MODELING OF SITE-SPECIFIC OPTICAL AND FLUORESCENT PROPERTIES AND THE CHANGES INDUCED BY 193 NM PHOTOCHEMICAL PERTURBATION.....</b>	<b>81</b>
Motivation .....	81
Materials & Methods .....	85
Simulation Workflow .....	85
Monte Carlo Model Construction .....	86
Multi-Layer Tissue Model .....	87
Fluorescent Interactions .....	89
Photochemical Interactions .....	90
Pathology Models .....	92
Simulation Details.....	93
Results.....	93
Model Validation.....	93
Pre-Perturbation Fluorescence.....	93
Excimer Laser Perturbation Patterns.....	94
Post-Perturbation Fluorescence .....	95
Computed Spectral Remittance and Layer-Specific Signals .....	95
Discussion .....	98
<b>4 DETECTION THEORY ANALYSIS OF DLIPS-BASED SENSING OF ORAL DYSPLASIA: IMPLICATIONS FOR CLINICAL INSTRUMENT DESIGN AND TESTING .....</b>	<b>117</b>
Motivation .....	117
Materials & Methods .....	119
Chemically-Induced Cheek Pouch Pathology.....	119
Collection of DLIPS and Fluorescence Spectra.....	120
Histopathology.....	122
Dimensional Reduction and Subspace Analysis .....	122
Classification Framework and Detection Performance .....	125
Results.....	126
Histopathology.....	126
Spectral Analysis.....	127
Subspace Analysis .....	128
Measurement Classification .....	131
Discussion .....	132
<b>5 CONCLUSION.....</b>	<b>151</b>
APPENDIX MATLAB® CODE FOR MONTE CARLO SIMULATIONS.....	156
LIST OF REFERENCES .....	181

BIOGRAPHICAL SKETCH..... 191

## LIST OF TABLES

<u>Table</u>		<u>page</u>
1-1	Common endogenous tissue fluorophores .....	43
2-1	Detection performance metrics using DLIPS, laser-induced fluorescence, or a decision fusion approach.....	77

## LIST OF FIGURES

<u>Figure</u>	<u>page</u>
1-1	Commercially available systems for augmenting oral cancer detection..... 40
1-2	Layers of epithelial tissue in the two general types of oral mucosa. A) keratinized ..... 41
1-3	Pictures and histology from patients presenting with different types of oral pathology ..... 42
1-4	Laser-tissue interaction possible as a function of exposure time and irradiance ..... 44
1-5	Cleavage of peptide bonds due to direct photolysis induced by absorbance of 193 nm photons from an excimer laser source ..... 45
1-6	Signal propagation and transformation map for non-invasive optical diagnosis of disease ..... 46
2-1	DLIPS acquisition scheme..... 70
2-2	Schematic of the DLIPS system ..... 71
2-3	H&E stained histology sections of skin ..... 72
2-4	Average spectra at weeks two (n=6, 7), six (n=5, 4), and eight (n=7, 8) ..... 73
2-5	Spectra at weeks two, six, and eight ..... 74
2-6	Score plots for the principal component analysis..... 75
2-7	Proportion of variance in Principal Component 1 accounted for by each wavelength ..... 76
2-8	ROC curves for the detection of DMBA-induced skin pathology using the DLIPS technique..... 78
2-9	ROC curves for the detection of DMBA-induced skin pathology using laser-induced fluorescence..... 79
2-10	ROC curves for the fused decision incorporating both fluorescence and DLIPS spectra to boost the optimal performance in detecting DMBA-induced skin pathology in the “late” timeframe, weeks nine to eleven. .... 80
3-1	Simulation workflow for modeling DLIPS fluorescence tissue spectroscopy .... 105
3-2	Tissue optical properties for layer-specific modeling ..... 106

3-3	Modeled layer-specific optical properties.....	107
3-4	Bland Altman plots comparing the total remitted light from the experimental Monte Carlo model versus a previously validated Monte Carlo system.....	108
3-5	Fluence ( $\text{cm}^{-2}$ ), in logarithmic units of photons through the tissue models .....	109
3-6	Relative per-layer absorption and fluorescence emission .....	110
3-7	Fluence ( $\text{cm}^{-2}$ ) of 193 nm light (logarithmic scale) through the superficial epithelium .....	111
3-8	Photochemical events stimulated by 193 nm irradiation as a fraction of the total number of incident photons.....	112
3-9	Relative contributions to the remitted DLIPS signal from each layer of epithelial tissue.....	113
3-10	Relative contributions to the remitted fluorescence signal from each layer of epithelial tissue .....	114
3-11	Simulated fluorescence spectra for the three tissue models .....	115
3-12	Binned spectral DLIPS data from Monte Carlo simulations .....	116
4-1	Fiber probe used for DLIPS and fluorescence measurements in the hamster cheek pouch .....	136
4-2	Pictures of everted cheek pouches displaying the model pathologies used in this study .....	137
4-3	H&E stained histology sections of cheek pouches .....	138
4-4	Average fluorescence spectra from 10 SLS-treated benign irritation cheek pouches (blue), 10 carrier only-treated control cheek pouches after 8 or 9 weeks of application (green), and 10 DMBA-treated dysplastic cheek pouches after 8 or 9 weeks of application (red).....	139
4-5	Average DLIPS spectra from 10 SLS-treated benign irritation cheek pouches (blue), 10 carrier only-treated control cheek pouches after 8 or 9 weeks of application (green), and 10 DMBA-treated dysplastic cheek pouches after 8 or 9 weeks of application (red).....	140
4-6	Percent of variance explained by each of the first ten principal components, p-values for the ANOVA between the three experimental groups (in each principal component), and post-hoc analysis to determine which group means are significantly different for the laser-induced fluorescence data .....	141

4-7	Percent of variance explained by each of the first ten principal components, p-values for the ANOVA between the three experimental groups (in each principal component), and post-hoc analysis to determine which group means are significantly different for the DLIPS data.....	142
4-8	Data groups used to derive the six FLD transformations as well as the corresponding SNR between the $H_0$ and $H_1$ data group pre- and post-transformation.....	143
4-9	ANOVA and Tukey-HSD post-hoc analysis of the transformed fluorescence measurements.....	144
4-10	ANOVA and Tukey-HSD post-hoc analysis of the transformed DLIPS measurements.....	145
4-11	Confusion matrix for the fluorescence data under transformation T1 .....	146
4-12	Confusion matrix for the fluorescence data under transformation T2 .....	147
4-13	Confusion matrix for the fluorescence data under transformation T4 .....	148
4-14	Confusion matrix for the DLIPS data under transformation T4 .....	149
4-15	Confusion matrix for the DLIPS data under transformation T2 .....	150

## LIST OF ABBREVIATIONS

ArF	Argon Fluorine
AUC	Area under the curve
DLIPS	Differential Laser-Induced Perturbation Spectroscopy
DMBA	7, 12-Dimethylbenz(a)anthracene
DNA	Deoxyribonucleic acid
ECM	Extracellular Matrix
FAD	Flavin adenine dinucleotide
FDA	Food and Drug Administration
FPR	False positive rate
H&E	Hematoxylin and eosin
HPV	Human Papilloma Virus
ICCD	Intensified Charge Coupled Device
IEEE	Institute of Electrical and Electronics Engineers
IHC	Immunohistochemical
MAP	Maximum a Posteriori
MCC	Matthews Correlation Coefficient
NADH	Nicotinamide adenine dinucleotide
Nd:YAG	Neodymium-doped yttrium aluminum garnet
NIR	Near-Infrared
PCA	Principle Component Analysis
ROC	Receiver Operating Characteristic
RF	Relative layer fluorescence
RTE	Radiative Transport Equation
SCC	Squamous cell carcinoma

SLS	Sodium Lauryl Sulfate
SNR	Signal-to-Noise Ratio
TNM	Tumor, Nodes, Metastasis
TOST	Two one-sided tests
TPR	True positive rate
UV	Ultraviolet
UVA	Ultraviolet A

Abstract of Dissertation Presented to the Graduate School  
of the University of Florida in Partial Fulfillment of the  
Requirements for the Degree of Doctor of Philosophy

NON-INVASIVE DETECTION OF PRE-MALIGNANT LESIONS USING SUB-  
ABLATIVE, DEEP ULTRAVIOLET LASER-TISSUE INTERACTIONS COUPLED WITH  
ENDOGENOUS TISSUE FLUORESCENCE: PROOF-OF-CONCEPT,  
COMPUTATIONAL MODELING, AND DETECTION-THEORY STRATEGIES FOR  
CLINICAL INSTRUMENT DESIGN AND TESTING

By

Raymond Thomas Kozikowski, III

December 2012

Chair: Brian Sorg  
Cochair: Brandi Ormerod  
Major: Biomedical Engineering

Half of all cancers are superficial in nature, originating in the stratified squamous epithelia including cervical, colorectal, skin, and oral cancer. Some of these diseases have seen a dramatic reduction in lethality due to the benefits of improved screening and diagnosis promoting earlier interdiction. Others, while treatable if caught at an early stage, have overall five year survival rates below 50% because they are challenging to identify early. These superficial carcinomas provide an opportunity for technological approaches to early detection due to the nature of their development: malignancy is invariably preceded by dysplastic precancerous cellular changes, which are often confined to the epithelial layer. These earliest changes are often not detectable visually, but are accessible using in vivo spectroscopy.

Optical spectroscopies have been widely investigated as techniques for identifying pathological tissue; however, unrelated subject-to-subject variations in spectra complicate interpretation and consequently clinical adaptation has been limited. In this dissertation a new biosensing technique, differential laser-induced perturbation

spectroscopy (DLIPS), is described and evaluated. This technique combines fluorescence probing (pre- and post-perturbation) with sub-ablative deep UV perturbation and difference spectroscopy to provide a new spectral dimension, facilitating two improvements over traditional techniques. First, this technique eliminates significant variations in absolute fluorescence within subject populations. Second, UV perturbations alter superficial protein layers, directly coupling the response to the spatio-biomolecular structure.

This work is focused on the confluence of this innovation and the unmet clinical need for tools to detect pre-cancerous transformations earlier and with greater accuracy. In a proof-of-concept study, this technique is shown to work at least as well as fluorescence spectroscopy alone in detecting cancer but couples more specifically to changes induced by the dysplastic state, and putative relationships are drawn between tissues spectra and their biomolecular basis. To further understand the benefits of this technique, Monte Carlo modeling of DLIPS tissue spectroscopy is also presented, demonstrating that excimer perturbation enhances the returned molecular signatures from tissue layers and specifically emphasizes important disease biomarkers. Finally in a pre-clinical model of both oral dysplasia and benign pathology, detection performance and optimization of DLIPS and fluorescence technologies are considered from a detection-theory perspective.

## CHAPTER 1 INTRODUCTION

### **Motivation**

More than half of all cancers are superficial in nature, originating in the stratified squamous epithelia, including cervical, colorectal, skin, and oral.<sup>1</sup> Some of these diseases have seen a dramatic reduction in lethality or number of cases, due in a large part to the benefits of improved screening and earlier diagnosis promoting earlier interdiction.<sup>2</sup> To continue to succeed, primary caregivers need new instruments and methods to continue pushing forward the time lines for cancer detection and diagnosis. Of particular utility are strategies that reduce the need for highly trained personnel and healthcare infrastructure to support screening and diagnosis, instead offering sample-to-answer capabilities at the point of care.

As an example, oral cancer is the sixth most common cancer worldwide and in the year 2007 accounted for over 400,000 new cases.<sup>3</sup> The lethal nature of oral cancer is not related to an inability to treat the disease, but rather the fact that it is often not discovered until the cancer has metastasized. The 5-year survival rate has hovered around 50% for 50 years, but if oral cancers are diagnosed at stage I, the likelihood of survival after treatment improves to nearly 90%.<sup>3-5</sup> When caught early, oral cancers are often smaller and treatable with a far lower incidence of morbidity.<sup>4, 5</sup> In some countries, oral cancers account for up to 40% of all cancers, further exacerbating the lethality.<sup>6</sup> Although this dramatically larger fraction is primarily a consequence of differential epidemiological risk-factors, the fact remains that earlier detection and diagnosis are essential to driving down the death rate due to oral cancer.

Despite the presence of advanced diagnostic aids available to clinicians (Figure 1-1), there is no evidence to support the ability of these devices to detect dysplastic changes at any earlier stage than what a trained clinician can detect using an unaided visual and tactile exam. Because of the specifics of these systems, detection relies upon discovering changes that are characteristic of dysplasia, but not necessarily unique to the malignant or pre-malignant state. As a result, these devices only serve to confirm what the physician already knows, adding limited new information regarding diagnosis or prognosis. Further, these techniques exacerbate the burden of disease by erroneously detecting false cancerous transformations; leading to unnecessary biopsies, interventions, and stress for the patient.

### **Specific Aims**

This dissertation describes the use of a new fluorescence spectroscopy technique, differential laser-induced perturbation spectroscopy (DLIPS), as a potential technique for the detection and staging of epithelium-derived dysplasia, like oral cancer. Here using both in vivo techniques and modeling it is demonstrated that this technology realizes a powerful new spectral dimension that is strongly coupled to the underlying biology and was previously inaccessible using other optical techniques. Presented in this dissertation are results from a proof-of-concept animal study, Monte Carlo simulations, and a preclinical study of oral dysplasia that all support future work translating this technique into a clinical instrument for the enhanced detection of cancer.

The long-term vision for this work is to develop DLIPS technology into a clinical system that impacts cancer morbidity and mortality by facilitating earlier, non-invasive detection and diagnosis of pre-malignancies. The primary objectives of this work were to develop and test the first DLIPS tissue spectroscopy system, continue to develop the

understanding of the molecular mechanisms underlying this technique, and consider how to integrate this enhanced tissue information into a clinical detection scheme. To accomplish these goals, this work was divided into the following specific aims:

- **Aim 1-** Show proof-of-concept for using DLIPS to detect dysplasia against healthy skin in a murine model of emerging malignancy
- **Aim 2-** Use Monte Carlo simulations of tissue fluorescence and photochemical interactions to develop a biochemical and pathophysiological basis for the DLIPS spectral signature
- **Aim 3-** Investigate DLIPS in the hamster cheek pouch model for the detection of oral dysplasia, in contrast to both healthy buccal tissue and benign pathology. Use these results to motivate strategies for clinical instrument design and testing

In total, the results of these three investigations show that the detection of dysplasia is possible using the DLIPS techniques, even in the presence of confounding benign pathology. These in vivo results are further supported by an exploration of the molecular signatures associated with the DLIPS signal. Further, by considering DLIPS both as a stand-alone and adjuvant detection technique, the flexibility and interoperability of this technique is demonstrated. These results provide strong evidence for developing this technique further for detection of oral dysplasia in clinical studies as well as transferring the DLIPS platform to other pathologies that would benefit from improved non-invasive diagnosis. This technology will have potential positive impacts by facilitating earlier cancer diagnosis (reducing mortality), showing proof-of-concept for the development of DLIPS sensing as a platform detection technology for other cancers and pathologies, and bridging the technology gap between in vitro molecular diagnostic techniques and in vivo optical and fluorescence spectroscopy.

## **Background**

To understand both the problem of detecting the pre-cancerous state as well as the opportunities for technological innovations that support enhanced cancer diagnosis,

there are several areas of knowledge that must be considered foundational to understanding the biology of cancer detection. First are the fundamentals of epithelial physiology and the changes associated with benign and pre-malignant pathology of the oral mucosa. Building off of these topics a treatment of current available diagnostic aids for enhanced oral cancer detection is discussed to round out the definition of the opportunity available for innovating in oral cancer diagnostics.

To support the development of biophotonics-based strategies in approaching solutions to this challenging diagnostic setting, a review of tissue optics concepts and current approaches is covered. From there, support is built for the scientific basis of the DLIPS technique by discussing the laser-tissue interactions and the photochemistry induced by excimer lasers. Additionally, the details of the DLIPS system are discussed from a signal to noise perspective, highlighting the advantages and susceptibilities associated with the DLIPS technique. Finally, the problem of optical cancer diagnostics is considered from a signal processing perspective, critical for properly framing the problem, understanding the needs and opportunities for innovation, and identifying rational approaches to solving these problems. A summary of these topics is presented here to motivate and support the experimental work discussed in the subsequent chapters of this dissertation.

### **Oral Epithelium Anatomy and Physiology**

The structure of epithelial tissues is roughly conserved throughout the body, consisting of thin, superficial, avascular layers of epithelial cells, supported by a basement membrane. Below this is a thicker stromal layer that supports the superficial cellular layers structurally with a dense collagen fiber matrix and nutritionally as it is vascularized. This deeper, thicker stromal layer attaches the epithelium to underlying

tissues. This structural archetype extends across skin, colon, cervix, and the oral cavity.<sup>7</sup> However, these tissues can vary greatly in the composition and function of the cells, altering the presentation of these tissues dramatically at both the macroscopic and molecular levels. Even in the oral cavity there are at least two structurally-unique epithelial tissues types, masticatory mucosa and lining mucosa (Figure 1-2 A, B).

The superficial layer of stratified squamous epithelium in the lining mucosa is the most apparently differentiator from the masticatory mucosa because it is non-keratinized. Despite not having a stiff, tough top layer of keratin, these superficial cells still accumulate significant amounts of keratin (in that sense, “non-keratinized” is a misnomer) as they push towards the surface. However these cells retain nuclei and organelles as they flatten and join this protein cross-linked network.<sup>7</sup> These non-keratinized tissues are softer and more flexible than their keratinized counterparts and most closely resemble the epithelial lining of the cervix.<sup>7</sup> In the intermediate and basal epithelial layers, cells grow and differentiate in as they push up from the basal layer into spinous intermediate layer. Here the cells form a coherent network of cells attached by spiny cellular processes and desmosomes.<sup>8</sup> Ultimately, these cells will flatten and increase their intracellular keratin density as they are pushed towards the superficial layer by cell from the basal layer. Between the basal epithelium and the lamina propria, the basement membrane is a flat interface, unlike in the masticatory region.<sup>7</sup> This supporting region of the oral mucosa is composed primarily of fibroblasts, collagen (20-25% by volume) and capillary networks (0.25% blood by volume).<sup>7, 9</sup> The extracellular matrix of this region is primarily collagen type I, with significant fractions of type III fibers

and elastin.<sup>10</sup> Lining mucosa covers oral regions including the cheek and the floor of the mouth.

Most noticeably, the masticatory region is covered by a tough keratinized, cornified layer that provides protection from mechanical injury, similar to the role of the keratinized surface of the epidermis.<sup>7</sup> These cornified cells are flat and hexagonal in shape, packed with keratin, and bound by a lipid matrix derived from interactions as cell fuse into this layer from the intermediate region.<sup>7</sup> Unlike the flat basement membrane junction of the non-keratinized epithelium, in the masticatory region there are ridges and connective tissue papillae into the epithelial layers; adding extra mechanical stability to these regions.<sup>7</sup> In between, the basal layers and spinous layers are the primary layer of cellular differentiation from basal cells into cornified superficial cells. This variety of tissue structure can make diagnosing disease challenging as the gross morphological changes between regions and those induced by pathology may be hard to deconvolve, there is thus a need for technologies to address subsurface sensing approaches to the in vivo detection and discrimination of pathology at the point of care.

### **Progression to Malignancy**

Still another layer of ambiguity exists in detecting carcinomas, cancers derived from the epithelium, or more importantly those earlier changes that will lead to a malignancy. This is because in back-tracing the progression to a carcinoma, the pattern of behaviors leading to the emergence of a malignant neoplasm are a mix of prognostic pre-neoplastic identifiers as well as many other morphological change highly non-specific to the cancerous transformation. In the case of oral cancer, definite visual identification is often not possible until a tumor actually begins to form at the latest stages of localized disease: the malignant neoplasm.<sup>11</sup> Although diagnosis at this stage

is unambiguous, the efficacy of intervention is limited because the cancer has disrupted and penetrated the basement membrane of the epithelium, providing access to the lymphatic and circulatory systems for the cancer to metastasize systemically. In the epithelium of the oral mucosa, this stage of disease is preceded by a period of disease in which the neoplastic cells are confined locally above the basement membrane, carcinoma in situ (TNM stage 0).<sup>11</sup> At this point the disease presents as an incipient cancer that if left untreated will definitely become a malignant neoplasm. The abnormal cells contained in this area have progressed into a stage of neoplastic growth; unchecked proliferation and an ambiguous state of cellular differentiation, among other abnormal cellular features.<sup>11</sup> This definite pathological state is brought about only following a much longer pre-interventional state of dysplasia, where both the presentation of disease (visually and histopathologically) as well as the fate of the lesion are unclear. Oral dysplasia is defined clinically using a cohort of abnormal cellular features including:<sup>12</sup>

- *loss of basal cell polarity*- loss of specific functions, shape or structures unique to the apical or basal faces of basal cells
- *parabasal hyperplasia*- abnormally large numbers of the smallest oral epithelial cells
- *increased nuclear:cytoplasmic ratio*- abnormally enlarged nuclei
- *drop-shaped rete ridges*- abnormally large regions of epithelial thickening extending down into the stroma
- *abnormal epithelial maturation*- highly differentiated cells observed in basal layers and non-differentiated cells observed in the superficial layers
- *increased mitotic activity*
- *mitosis in the superficial epithelium*
- *cellular pleomorphism*- abnormally-shaped cells

- *nuclear hyperchromaticity*- abnormal increase in the density of nuclear material in the nucleus
- *enlarged nucleoli*
- *loss of cellular cohesiveness*- decrease in the organization and packing of the cells within and between epithelial layers
- *cellular keratinization in the spinous epithelial layer*- abnormal keratin density in the cytoplasm of non-superficial epithelial cells

It is at this point where an ability to identify and assess the malignant potential of lesions would add a clear benefit to patients, improving 5-year survival rates to over 90%.<sup>4,5</sup> Diagnosis prior to this point is likely not possible given the current understanding of these earlier stages of neoplasm development as well as the development of benign pathologies. Still there is opportunity in continuing to identify pre-malignant conditions, morphologies with an associated risk of malignant tumor formation (eg: chronic oral ulceration), as a means of screening the population for high-risk patients, but that is not within the scope of this work. With the current state of disease understanding and non-invasive technologies, one is limited to attempting to evaluate and discover pre-malignant lesions, those morphologies containing dysplastic cells that will definitely progress to malignancy (eg: cervical epithelial dysplasia, adenomatous polyps).<sup>13-15</sup> Fundamentally, a new detection technique for oral cancer must not just detect dysplasia, but must be able to further determine if that lesion has malignant potential or will simply persist as a benign lesion.

### **Oral Cancer Detection**

Oral cancer provides an excellent example of both a problematic diagnosis as well as an opportunity in that early diagnosis and intervention can have a dramatic impact on survival.<sup>3-5</sup> Because of the high value associated with improved diagnosis of oral

cancer, there are multiple strategies both in the laboratory and in the marketplace to address this need, but with uniformly disappointing results. In review articles published in 2007, 2008 and 2010, the authors all reached similar conclusions regarding these systems: there is insufficient evidence to support claims of improved oral cancer diagnosis over conventional oral examination.<sup>3, 13, 15</sup>

Principally, the problem is an inability to sort dysplastic from benign disease. This is because the preclinical phase of the dysplastic transformation into oral squamous cell carcinoma is varied, often asymptomatic, and easily misdiagnosed as benign inflammation, hyperkeratosis, or ulceration.<sup>16</sup> Conversely, several benign oral abnormalities are often mistaken for oral cancer including morsicatio buccarum, melanotic macules, or leukodema.<sup>16</sup> And these benign diseases are in fact more prevalent than oral cancer, as up to 15% of the population presents with oral mucosal disease (non-malignant or pre-malignant) at any given time.<sup>17, 18</sup> Further complicating the issue, dysplastic changes may be associated with some other oral pathologies (proliferative verrucous leukoplakia, lichen planus), poor oral hygiene (leading to chronic inflammation), or chronic mucosal infections (HPV and herpes simplex).<sup>19, 20</sup> These co-morbidities mask the slow pre-malignant transformations from both the dental professional and currently available diagnostic aids. As a result, most dental professionals choose to follow suspicious lesions over time, watching for clear signs of the malignant transformation before opting for biopsy to confirm diagnosis or begin treatment Figure 1-3 illustrates this, showing cases investigated by Dr. Indraneel Bhattacharyya (Department of Oral & Maxillofacial Diagnostic Sciences, University of Florida, Gainesville, FL), where visual inspection alone would miss dysplastic changes,

another where a benign lesion resembles an oral pre-malignant lesion (but histology confirms the lack of cancer), and a final example where a suspicious lesion is confirmed as cancerous after histopathological analysis.

Figure 1-1 covers the most pervasive detection technologies for oral cancer and compares them to unaided examination. A common sentiment within the scientific and medical community is there is a lack of rigorous clinical testing of these devices, with manufacturers instead relying on studies of high risk (or previously diagnosed) populations where the incidence of cancer was often above 20% and in some cases as high as 100% or anecdotal evidence from individual case studies.<sup>3, 13</sup> This introduces a large spectrum bias between the diagnostic performance of these devices on the tested (virtual certainty in presence of cancer) and target population (uncertainty in clinical presentation). Further, many of the studies either point out directly or it has been noted by others, that the investigational devices were not able to perform better than unaided visual/tactile examination by a physician; likely due to the obvious presentation of dysplastic transformation or outright squamous cell carcinoma.<sup>3, 13</sup> Compounding this issue is that many of the studies have a limited data set to compare against the gold standard, biopsy. This is not a shortcoming of the studies but rather due to the fact that it would be unethical to biopsy tissue that did not present with clinical indications warranting such an invasive procedure. However this inadvertently screens out many potential false negatives from the data collected on the performance of these devices. Therefore, the diagnostic performance numbers reported in the literature (Figure 1-1) should be understood to represent the best-case performance metrics and ultimately do not reflect how well this devices perform at the point-of-care. Despite that, all of these

systems are highly susceptible to reporting false positives; detecting oral cancer when in fact there is no dysplasia present. The explanation is a complex mix of the following factors:

- The high cost associated with missing dysplastic lesions (false negatives) leads to an unacceptable amount of false positives
- The sources of tissue contrast employed in these devices is not unique to the molecular changes of the oral dysplastic transformation (erroneous detection of benign conditions)
- High degree of intra-patient variation in tissue properties (source of noise in non-referential detection schemes)

This low specificity, regardless of the tradeoff for improved sensitivity to finding pre-malignant lesions or cancer, is troubling for a number of reasons. Tests with low specificity have little diagnostic merit due to the high prevalence of disease finding when none is present. This nullifies the utility of the test as a positive result will always require a confirming follow-up test. In the case of oral cancer, this gold standard for follow-up would be biopsy. However, when these techniques are tested in independent clinical trials or by practitioners, there is little evidence to support the claims of improved sensitivity; the devices do not show improved ability to detect dysplasia and additionally report unacceptably high numbers of false positives.<sup>3, 13</sup>

### **Tissue Optics Fundamentals**

In this work, well-established relationships between changes in tissue structure and disease state are exploited with a novel light-based sensing scheme to enhance discrimination of dysplastic tissue in vivo. The field of tissue optics is concerned with a fundamental understanding of these associations, and these principles form the basis for the application of light-based strategies to disease detection and diagnosis. As a gross over-generalization, when a photon interacts with matter it is either absorbed by

that material or it is not.<sup>21</sup> When the light is not absorbed it will exit the material, with its trajectory potentially altered by scattering. On the other hand, once the light is absorbed, there are multiple possible fates. To connect this basic idea with biological tissue, tissue optical analysis is concerned with two basic ideas. First is an understanding of the light energy per time interacting with a chromophore at a fixed position in the tissue, known as the fluence rate.<sup>21</sup> Unfortunately, this information is not directly observable; however by modeling the optical properties of tissues and incorporating information about the radiance and remitted/transmitted light, it can be approximated. Second, and more relevant to the task of applying biomedical optics to disease diagnosis, is to measure the optical properties of tissue.<sup>21</sup> This is essentially the inverse problem of the first task, in the sense that with an accurate picture of the fluence in tissue and incident radiance, the optical properties can be inferred.

Although the absorption and scattering properties of tissue are a direct result of the molecular structures and the chemical environment surrounding them, in tissue regions are often assumed to have bulk scattering and absorption properties, described by a scattering coefficient,  $\mu_s$ , where the inverse of this parameter describes the average distance between scattering events, and an absorption coefficient,  $\mu_a$ , where the inverse of this parameter describes the average distance a photon travels between absorption events.<sup>21</sup> Empirically, these values represent the superimposed effects of all the constituent chromophores in the tissue, but realistically calculations are often not possible and these bulk optical properties must be measured or estimated using less-direct approaches.<sup>22</sup> Absorption in tissue around the visible light range is highly

wavelength-dependent and driven by several key diagnostic chromophores with high extinction coefficients including hemoglobin, myoglobin, and melanin.<sup>23</sup>

Scattering in biological tissues is equally important for tissue optical diagnostics, as scattering effects tend to dominate absorption in the UVA, visible, and near infrared portions of the optical spectrum.<sup>21</sup> This will determine the volume of interaction for incident light as well as how well a beam is able to maintain its original collimated structure.<sup>21</sup> Elastic scattering, the redirecting of light without a loss of energy, is the most common effect observed in tissue and thus inelastic scattering will not be considered here. Sources of scattering arise at three size levels, macroscopic from muscle fibers and tissue layers, microscopic from cells and organelles, and submicroscopic from macromolecules and their structures (protein fibers and lipid membranes).<sup>24</sup> In tissue, the scattering of light is often approximated by combining the effects from a Rayleigh description of scattering as well as Mie Theory. The combination is harmonious as each describes scattering events at a different scale, for structures much smaller than a wavelength of light and for structures on the scale of or larger than a wavelength respectively. Around the visible portion of the spectrum, Mie Theory tends to contribute substantially, including dictating the angle through which the incident light is scattered. This is defined as the anisotropy factor,  $g$ . Using the Henyey-Greenstein function, this parameter can be used to approximately describe the probability of light be scatter off of a particle at a particular angle.<sup>24</sup> Tissue, as a generally rule, is highly forward-scattering, with anisotropy factors in the range of 0.65 to 0.95.<sup>23</sup>

When light is absorbed that energy must be dissipated as the excited absorber returns to its ground state from its excited molecular state. Typically, this energy is

dissipated through collision quenching or converted in heat, but for certain molecular systems, more complex photochemical interactions are possible. The most well-known photochemical reaction is that of fluorescence generation. This occurs when the excited electron moves from one energy level to a lower energy level within the excited state. Upon relaxing back to the ground state, the emitted photon is at a lower energy (longer wavelength) than the excitation photon.<sup>21</sup> Although this is not the only photochemical process possible from the excited state, it is the most common in biomolecules and the most germane to this particular optical diagnostic technique. Generally, fluorescence is a nondestructive and sensitive technique that allows *in vivo* detection of organic and biological materials under different environmental conditions in very short times. Because the excitation/emission wavelength pair is a combination of the molecular structure and the overall molecular environment (e.g. biological matrix), fluorescence emission may provide discrimination among emitting materials. Tissue autofluorescence is primarily derived from several major endogenous tissue fluorophores are shown in Table 1-1, with their most prominent excitation and emission ranges listed as well.<sup>25</sup> It has been shown that many of these molecules are correlated with certain pathological conditions and have unique distributions in tumors, and that these fluorescent molecules can be used to distinguish benign from malignant tumors.<sup>26, 27</sup>

Light propagation in tissue can be considered analytically with the Radiative Transport Equation (RTE) shown in Equation 1-1.<sup>22</sup>

$$\frac{1}{c} \frac{\partial L(\vec{r}, \hat{s}, t)}{\partial t} = -\hat{s} \cdot \nabla L(\vec{r}, \hat{s}, t) - \mu_t L(\vec{r}, \hat{s}, t) + \mu_s \int_{4\pi} L(\vec{r}, \hat{s}', t) P(\hat{s}' \cdot \hat{s}) d\Omega' + S(\vec{r}, \hat{s}, t) \quad (1-1)$$

This equation relates both the goals of tissue optical diagnostics (understanding light propagation in the context of the optical properties of tissue) into a single unifying

relationship that is driven by a source term and the losses of light energy from that incident beam in terms of divergence and extinction, considers the light incident on and propagating from infinitesimally small spherical region of the medium, and describes the absorption and scattering properties of the medium.<sup>22</sup> However, there is often no closed form solution to this equation without introducing approximations such as the diffusion approximation and these approximations only apply under highly contrived situations.<sup>21</sup> A more flexible method for estimating the fluence and remission of light from tissue are Monte Carlo-based numerical simulations. These methods have the added benefit of permitting extension of the model to other photo-effects including fluorescence and photochemical reactions.<sup>9, 28-30</sup>

Although still emerging as a platform for disease diagnostics, the systematic study of light-tissues interactions both in vivo and in vitro has yielded a wealth of information regarding the optical properties of biological samples at nearly all scales: individual molecules, macromolecular structures, cells and organelles, as well as whole tissues and entire organs. As an example, a summary of research into the optical properties of the oral mucosa is given in Figure 3-2 to drive model development for studying the DLIPS system. This has allowed for refinement of optical disease detection strategies, designed to probe these properties and the changes associated with disease, into clinical instruments capable of dramatically improving healthcare providers' ability to detect and diagnose disease.

### **Excimer Laser-Tissue Interactions**

Generally, tissue optical properties for diagnostic applications are only considered in the range of visible and near-infrared frequencies that have relatively low absorbance by water, nucleic acids, and most proteins (aside from those with transition metal

complexes such as hemoglobin). However, for the application presented here, a discussion of the light-tissue interactions for coherent deep ultraviolet light is necessary as well. For the wavelength range of ArF excimer lasers there is considerable absorption of light in tissue by peptide bonds, aromatic compounds, and nucleic acids.<sup>31, 32</sup> Although there are few studies measuring the optical properties of tissue for the deep UV range, estimates range from  $1000 \text{ cm}^{-1}$  up to  $20,000 \text{ cm}^{-1}$ , with these properties varying greatly depending upon the biomolecular target tissue composition.<sup>24, 31, 32</sup> While there are no studies exploring the scattering properties of light in tissue in the deep UV range, it is expected that scattering should increase by a factor of 16 from that observed at 400 nm because of the dominance of Rayleigh scattering at shorter wavelengths.<sup>24</sup> It is further assumed that the scattering of light will be fairly isotropic as well given the heavy weighting towards Rayleigh scattering. It is also known that excitation of some amino acids at 193 nm can induce fluorescence, but this effect is minimal when compared to the range of other energy-emissive effects possible at this wavelength. Figure 1-4 summarizes the possible effects of tissue exposure to laser irradiation, as a function of both pulse duration and intensity. The perturbation pulses from the deep-UV excimer laser (193 nm, 6.4 eV) are strongly absorbed by biological tissue and used to cleave molecular bonds within the extracellular matrix (ECM) as shown schematically in Figure 1-5. Irradiation of biological matrices at 193 nm can cause photoionization, including strand breakage, locally denatured sites, interstrand cross-linking, reactions via photo-hydrates,  $\pi$ -dimers, and other products.<sup>33</sup> The primary absorbers of 193 nm light in vivo are peptide bonds and aromatic amino acid side chains with respective extinction coefficients around  $5.5 \times 10^3 \text{ M}^{-1}\text{cm}^{-1}$  and  $2 \times 10^4 - 5 \times$

$10^4 \text{ M}^{-1}\text{cm}^{-1}$  and are roughly found at concentrations of 1 M and 0.1 M in the cytosol of epithelial cells.<sup>32</sup> Although nucleic acids also have high absorbance cross-sections for 193 nm light, it has been shown that due to the high concentration of peptide bonds in the cytosol, limited photochemical reactions are realized on the nuclear material contained within the nucleus.<sup>31</sup> While no direct ablation is realized for the low energy densities used in this application, around  $2\text{-}3 \text{ mJ}/\text{cm}^2$  (see Figure 1-4), a single photon of 193 nm radiation exceed nearly all bond energies (around 4 eV for peptide bonds and aromatic ring systems) in the biological matrix and for cytosolic proteins, hence permanent photochemistry is induced despite being below the critical photon flux to affect material removal. In some studies the quantum yields for the scission of peptide bonds,  $\Phi_{\text{sc}}$ , has been found to vary from about 2% to 3% while the quantum yield for the photodissociation of aromatic amino acids,  $\Phi_{\text{d}}$ , was reported to be in the range of 10% to 12%.<sup>34, 35</sup>

### **DLIPS: State of the Technology**

The DLIPS sensing scheme incorporates two complementary techniques to improve upon previous biosensing strategies: ultraviolet laser perturbation of tissue, and difference spectroscopy (Figure 1-5).<sup>36</sup> This technique is flexible in that it can be applied to multiple spectral domains, creating a means to extending existing equipment and analytical techniques into a new domain of biochemical analysis. These domains could include fluorescence spectroscopy, Raman spectroscopy, or even non-optical techniques such as nuclear magnetic resonance. In this work, fluorescence is used to measure endogenous tissue fluorescence before and after the tissue is laser-perturbed. Despite the excimer laser intensity being well below the threshold for tissue ablation, permanent alteration of the underlying tissue structure is induced, with resulting

changes within the fluorescence spectrum, specifically with respect to photoreactive biomolecules. The proposed cancer detection technology is rooted in previous research demonstrating that the biological matrix (collagen and amino acids) may be altered by low intensity (i.e. subablative) coherent UV light such that the resulting fluorescence properties are perturbed.<sup>36, 37</sup> Initial proof of concept was shown using dye fluorophores, collagen, and bovine corneas. In testing this technique using peptides, a photochemical efficiency of around one peptide bond cleavage event per 50 incident photons was reported.<sup>36, 37</sup> These initial tests with excised tissue confirmed the proof of concept for coupling this technique with both fluorescence and Raman spectroscopy. In these experiments, the excimer laser was used at a fluence more than 20 times below the fluence used for refractive surgery (marked on Figure 1-4). Further, using this technique in collagen films, the fluorescence signal was found to actually be enhanced by photochemical perturbation, suggesting some mechanism for releasing the fluorescence crosslinking compounds (hydroxylysyl pyridinoline and lysyl pyridinoline) from the collagen matrix as a result of perturbation.<sup>10, 25</sup> Details of computing the DLIPS spectrum as well as the system used for subsequent in vivo applications can be found in Chapters Three and Five of this document.<sup>38</sup>

### **DLIPS: A Signal-to-Noise Perspective**

Approaching the DLIPS technique and fluorescence spectroscopy from a stochastic signals-in-noise perspective obviates several important considerations for actual applications of this technique. Equations 1-2 through 1-8 in the scheme below describe a single observation of a signal (DLIPS or fluorescence), in the presence of additive white Gaussian noise, here assumed to be due to the measurement technique alone, and not capturing signal variability between targets. In estimating the signal-to-

noise ratio (SNR) for each technique, the SNR is defined as the average observed signal, divided by the standard deviation for multiple observations. Since the DLIPS measurement is a differential measurement, the signal strength scales to the size of that difference, in this case to between 10% and 1% of the original fluorescence signal. This large difference in signal magnitude between DLIPS and fluorescence is shown in Equation 1-8. The white noise from the background does not scale and in fact the variance is marginally amplified during the computation of the DLIPS signal from the parent fluorescence measurements (Equations 1-2 and 1-3). The very best case scenario then is that the noise is only amplified by a factor of root two, but is likely worse for low signal levels as the contribution from the denominator must be factored into the equation as well and can no longer be approximated as having no contribution. This implies that the very best case scenario is that the DLIPS SNR is approximately 14 times lower than measurements made using fluorescence alone. The reality however is that the measurement SNR is possible more than 140 times lower when low signal fluorescence measurements are made.

$$DLIPS(\lambda = \lambda_x) = \frac{[Em_{post}(\lambda_x) + N(\mu_{bkgd}, \sigma^2)] - [Em_{pre}(\lambda_x) + N(\mu_{bkgd}, \sigma^2)]}{Em_{pre}(\lambda_x) + N(\mu_{bkgd}, \sigma^2) - Dark(\mu_{bkgd}, \sim 0)} = \dots$$

$$\dots = \frac{Em_{post}(\lambda_x) - Em_{pre}(\lambda_x) + N(0, 2\sigma^2)}{Em_{pre}(\lambda_x) + N(0, \sigma^2)} = \frac{\Delta Em(\lambda_x) + N(0, 2\sigma^2)}{Em_{pre}(\lambda_x) + N(0, \sigma^2)} \quad (1-2)$$

$$SNR_{DLIPS} (lowFluor) < \frac{\Delta Em(\lambda_x)}{\sqrt{2}\sigma} \quad (1-3)$$

$$SNR_{DLIPS} (highFluor) \approx \frac{\Delta Em(\lambda_x) / Em_{pre}(\lambda_x)}{\sqrt{2\sigma^2 / Em_{pre}(\lambda_x)^2}} = \frac{\Delta Em(\lambda_x)}{\sqrt{2}\sigma} \quad (1-4)$$

$$Fluor(\lambda = \lambda_x) = Em_{pre}(\lambda_x) + N(\mu_{bkgd}, \sigma^2) - Dark(\mu_{bkgd}, \sim 0) = Em_{pre}(\lambda_x) + N(0, \sigma^2) \quad (1-5)$$

$$SNR_{Fluor} = \frac{Em_{pre}(\lambda_x)}{\sigma} \quad (1-6)$$

$$\Delta Em(\lambda_x) \ll Em_{pre}(\lambda_x) \quad (1-7)$$

$$SNR_{DLIPS} \ll SNR_{Fluor} \quad (1-8)$$

To complete this description of measurement SNR for DLIPS versus fluorescence alone, the effect of repeated measures must be considered as well. For the fluorescence measurements alone, the SNR will improve directly as a factor of the number of repeated observations. This is analogous to a maximum likelihood estimation of the fluorescence signal. But for the DLIPS SNR, this scaling is reduced during the computation of the DLIPS signal, since repeated measures can only be made for the  $Em_{pre}$ ,  $Em_{post}$ , and the *Dark* signals but not the DLIPS signal directly. So the DLIPS SNR will improve by averaging repeated individual measurements, but the effect will be diminished during the computation.

### **In vivo Optical Diagnostics: Problem Formalization**

From a signal processing or information propagation perspective, the problems of understanding the experimentally-accessible optical properties of disease, and making a non-invasive diagnosis can be described as a cascade of change of bases; propagating information from the actual disease state to the detected disease state as shown in Figure 1-6. As the goal is detection of a disease state, the underlying information begins as a (in this case) one-dimensional representation of the true state, with examples including: healthy, benign, pre-malignant, or malignant. This information is projected into the “feature space” of disease through some subspace change of basis transform which converts the information encoded in the disease state into an n-dimensional vector of all of the features that describe any tissue disease state. Features

in this case might include nuclear-cytoplasmic ratio, shape, or basement membrane. And “states” of the feature “nuclear-cytoplasmic ratio” could include integers from 1 to  $n$ . A priori knowledge or accurate modeling of this projection for each of the disease state is critical for both traditional diagnostic medicine or to understand the characteristics to exploit in designing optical diagnostic systems. In the case of a pathologist examining histological slides, that physician computes an approximation of the inverse transformation between the disease state and the observable features; to arrive at an estimate of the disease state, his diagnosis. If one is interested in building a device for detecting the disease state, then understanding the layer of detectable feature is critical for tuning that sensing system to use the optimal combination of those features to estimate the disease state.

If a non-invasive optical sensing scheme is the desired sensing modality, then this feature space is further transformed via a change of basis into a matrix of spatio-optical properties, where in the first dimension, the relevant optical properties such as absorbance, scattering, and fluorescence are defined, and the second the unique position in the tissue for those properties are defined. When a measurement is actually made, this information is then transformed into the subspace of remitted light, a matrix of the spatial position of the light versus the wavelength of the light. This is the state of information readily accessible for non-invasive optical diagnostics. In the final transform, this information is transformed into an estimate of the disease state, the diagnosis. Again this hinges on being able to accurately approximate the inverse transformation to convert the collected light back into its original form of “disease state”. Unfortunately when considering this transformation cascade, no assumptions of linearity or

uniqueness were made, making a closed form solution to the inverse transform impossible. Further, for an in vivo experiment or clinical measurement, many of these information representations are inaccessible, essentially contained within a black box.

By framing the problem in this way, there are two appropriate approaches to understanding the remitted spectral signature in the context of detecting the disease state: developing model-based approximations to the transfer functions contained within the tissue black box, or defining an arbitrary transform for the remitted light that minimizes the error between the estimate of the disease state and the actual disease state. Using this framework for the problem-space of oral cancer detection, the experiments presented here seek to define this black box of disease for DLIPS tissue spectroscopy through both experimental approaches as well as modeling. In combining these two approaches, a deeper understanding of these transformations is realized with the potential for improving the state of the technology as a future high-impact clinical diagnostic tool.

### **Experimental Outline**

After this chapter the remainder of this dissertation is organized into four subsequent sections:

Chapter Two is adapted from a paper published in *Journal of Biomedical Optics* that demonstrates the proof-of-concept for using DLIPS in vivo. This work represents the first use of DLIPS in vivo, specifically monitoring the progression of pre-cancerous skin lesions. Using multivariate statistical methods and optimal detection theory, the DLIPS technique is shown to provide a more robust measure of pre-neoplastic tissue differentiation in this model. Further, the unique molecular underpinning of the source of

tissue contrast detected by DLIPS is considered and shown to vary spectrally from that of tissue fluorescence alone.

The third chapter is a paper that is being prepared for submission to IEEE Transactions in Biomedical Engineering, where Monte Carlo modeling of DLIPS-tissue interactions is employed to consider the molecular underpinnings of this technique as a disease detection technology. This work represents the first attempt to model both the DLIPS technique as well as excimer laser tissue photochemistry using Monte Carlo methods. The results demonstrate that the nature of the DLIPS technique permits specific coupling to the most superficial epithelial tissue layers, accessing molecular information that is obscured when analyzing normal tissue fluorescence signatures. This unique access to complimentary molecular information further promotes previous finding that DLIPS may compliment fluorescence spectroscopy using orthogonal sensing methodologies.

Chapter Four presents a study of both dysplastic changes and benign pathology in the hamster cheek pouch using DLIPS that is being prepared for publication in Optics Letters. This work explores the inherent contrast between oral dysplasia and a confounding non-cancerous oral pathology for both DLIPS and fluorescence spectroscopy; particularly germane as these non-cancerous inflammatory lesions are most commonly mistaken for dysplasia (and vice versa). Using discriminant analysis and optimal detection theory, this work demonstrates that clinical detection systems must be trained to recognize the contrast between dysplastic lesions and benign lesions; a non-trivial result as this is not a common practice for either the development of clinical testing of commercially-available devices.

The final chapter summarizes these finding, considers the implications of this work, and provides future directions to build off of these results.

System	Technique	Contrast Mechanism	Claimed dysplastic target	Diagnostic Performance Ranges	Limitations
 <b>Toluidine Blue</b>	Tissue Staining	preferential tissue binding	rapidly dividing cells	Sens: 38-98%, <b>Spec: 9-93%</b> , PPV: 33-93%, NPV: 22-92%	high degree of operational/interpretational variability
 <b>VELscope</b>	Visualization	loss of fluorescence	structural changes, metabolic activity	insufficient published data	loss of signal may be due to non-pathological changes (eg: hemoglobin absorbance)
 <b>Identafi</b>		fluorescence and reflectance	structural changes, metabolic activity, inflammation	insufficient published data	highlights non-specific molecular changes
 <b>ViziLite Plus</b>	Wash + Visualization	wash, wavelength-specific enhanced visualization	altered epithelial thickness, higher density nuclear or mitochondrial content	Sens: 100%, <b>Spec: 0-14%</b> , PPV: 18-80%, NPV: 0-100%	benign hyperkeratinization is indistinguishable from dysplasia
 <b>Microlux DL</b>		see above (virtually identical technique)	see above	insufficient published data	see above
 <b>Oral CDx</b>	Cytopathology	Brush swab with Papanicolaou stain	abnormal nuclei, keratin content, other cellular abnormalities	Sens: 71-100%, <b>Spec: 27-94%</b> , PPV: 38-88%, NPV: 60-100%	Does not return a diagnosis. Time lost for treatment during analysis
<b>Visual/Tactile Exam</b>	Current standard of care	physical examination under white light	pigmentation, ulcerations, time-course, patient information	<b>Sens: 40-93%</b> , Spec: 50-75%, PPV: 36-78%, NPV: 71-90%	requires highly trained personnel to achieve acceptably low rates of false negatives

Figure 1-1. Commercially available systems for augmenting oral cancer detection

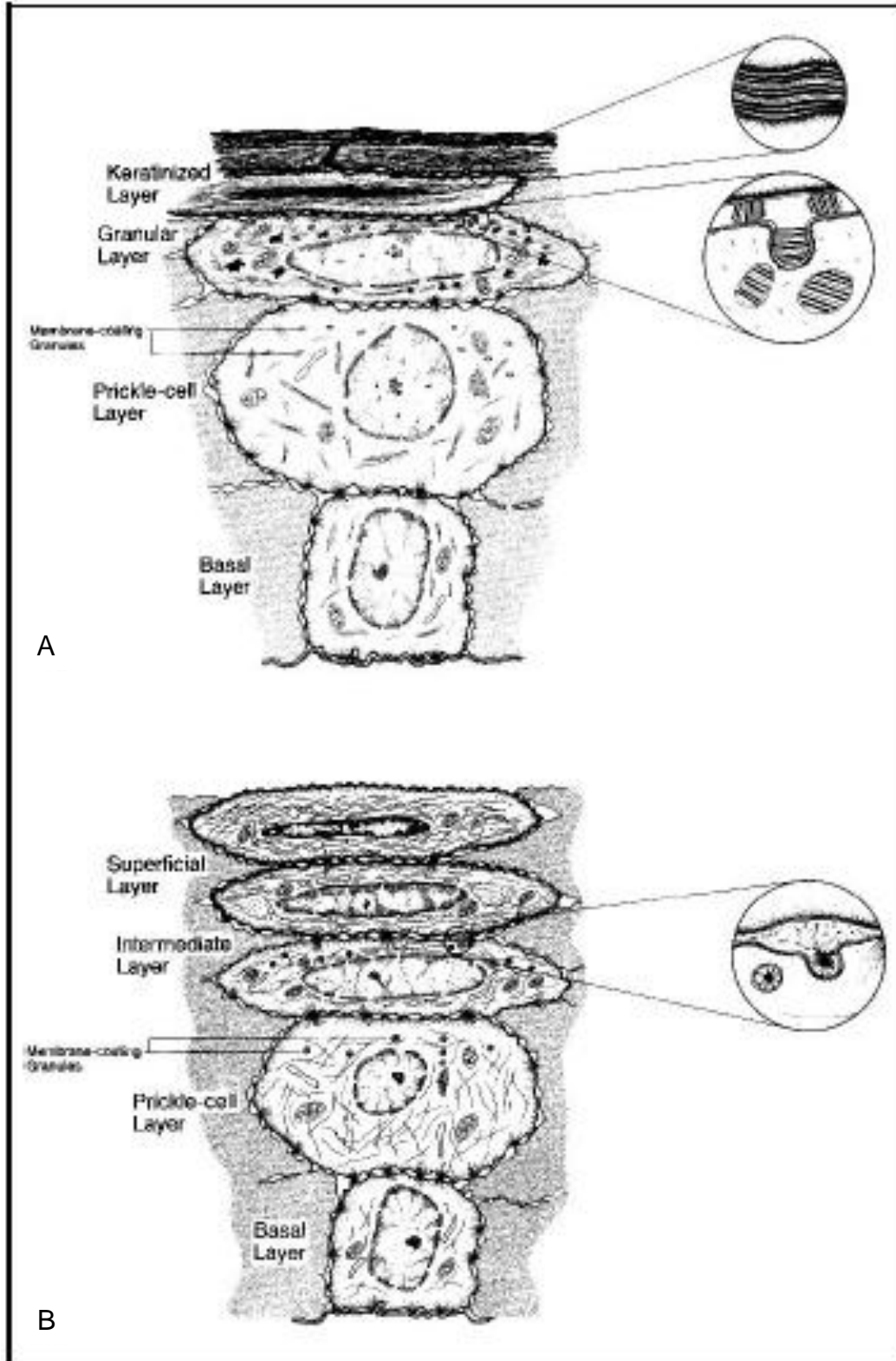


Figure 1-2. Layers of epithelial tissue in the two general types of oral mucosa. A) keratinized. B) non-keratinized [CA Squier, and MJ Kremer, "Biology of Oral Mucosa and Esophagus," J Natl Cancer Inst Monogr 29, 7-15 (2001)]

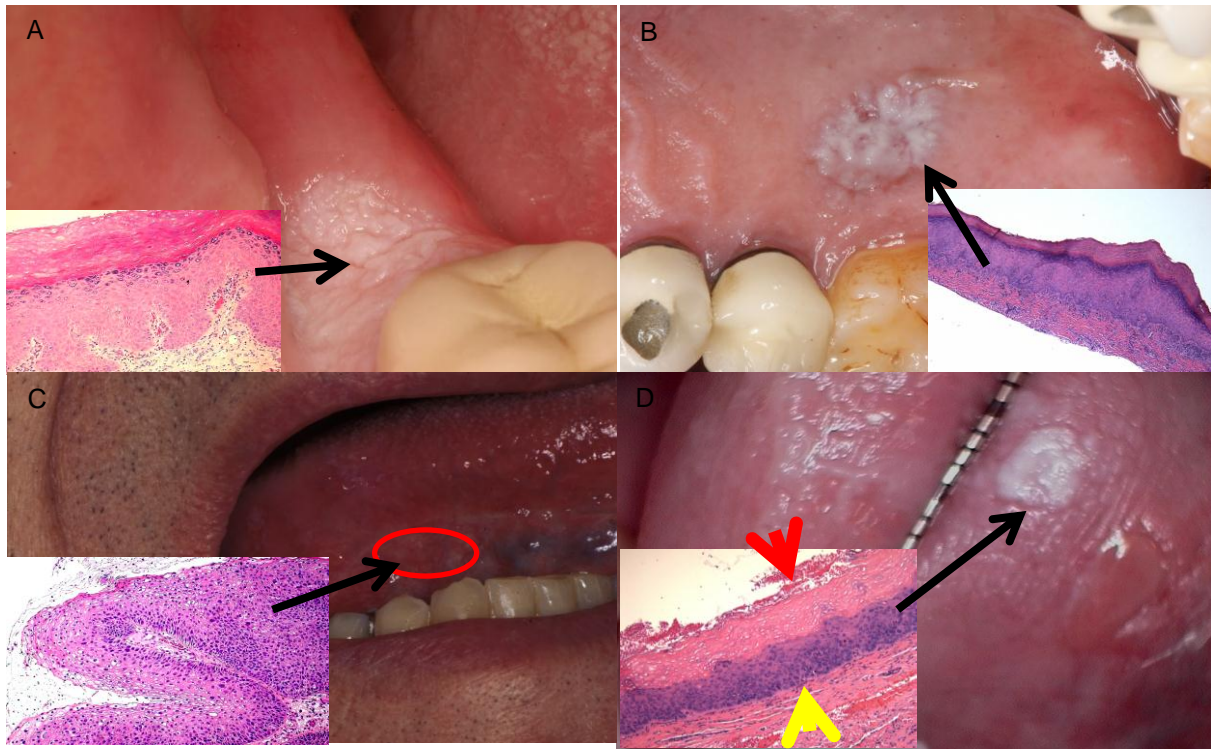


Figure 1-3. Pictures and histology from patients presenting with different types of oral pathology. Visual and cellular/molecular presentation often do not agree, thus the need for new diagnostic tools to detect oral dysplasia with a biopsy. A) Significant leukoplakia in a low risk site without dysplastic changes. This would often register as cancer using currently available diagnostic aids. B) Significant verrucoid leukoplakia in a low risk site without visible dysplasia, but a very worrisome histologic profile. This normally would not be biopsied. C) Subtly visible lesion, but severe dysplasia reveal in the biopsy. D) Severe verrucoid/papillary hyperkeratosis. Keratin layer is equal in thickness to the rest of the epithelial layers. Severe dysplasia with increased nuclear/cytoplasmic ratios, nuclear pleomorphism and basilar hyperplasia. [Photos and histology courtesy of Indraneel Bhattacharyya, 2012]

Table 1-1. Common endogenous tissue fluorophores

Chromophore		Excitation Min	Excitation Max
Metabolism Markers	NADH	290 nm	440 nm
	FAD	340 nm	450 nm
Peptides	Tryptophan	280 nm	350 nm
	Tyrosine	275 nm	300 nm
	Phenylalanine	260 nm	280 nm
Structural Proteins	Collagen	280 nm	310 nm
		265 nm	385 nm
		330 nm	390 nm
	Elastin	450 nm	530 nm
		350 nm	420 nm
		410 nm	500 nm
		450 nm	520 nm
	Hydroxylysyl Pyridinoline Lysyl Pyridinoline	325 nm	400 nm
		325 nm	400 nm
		325 nm	400 nm
Lipid Degradation Products	Ceroid	340-395 nm	430-460 nm
	Lipofuscin	410-470 nm	500-695 nm
Vitamin B6 and derivatives		310-340 nm	375-430 nm
Porphyrin derivatives		~400 nm	600-650 nm

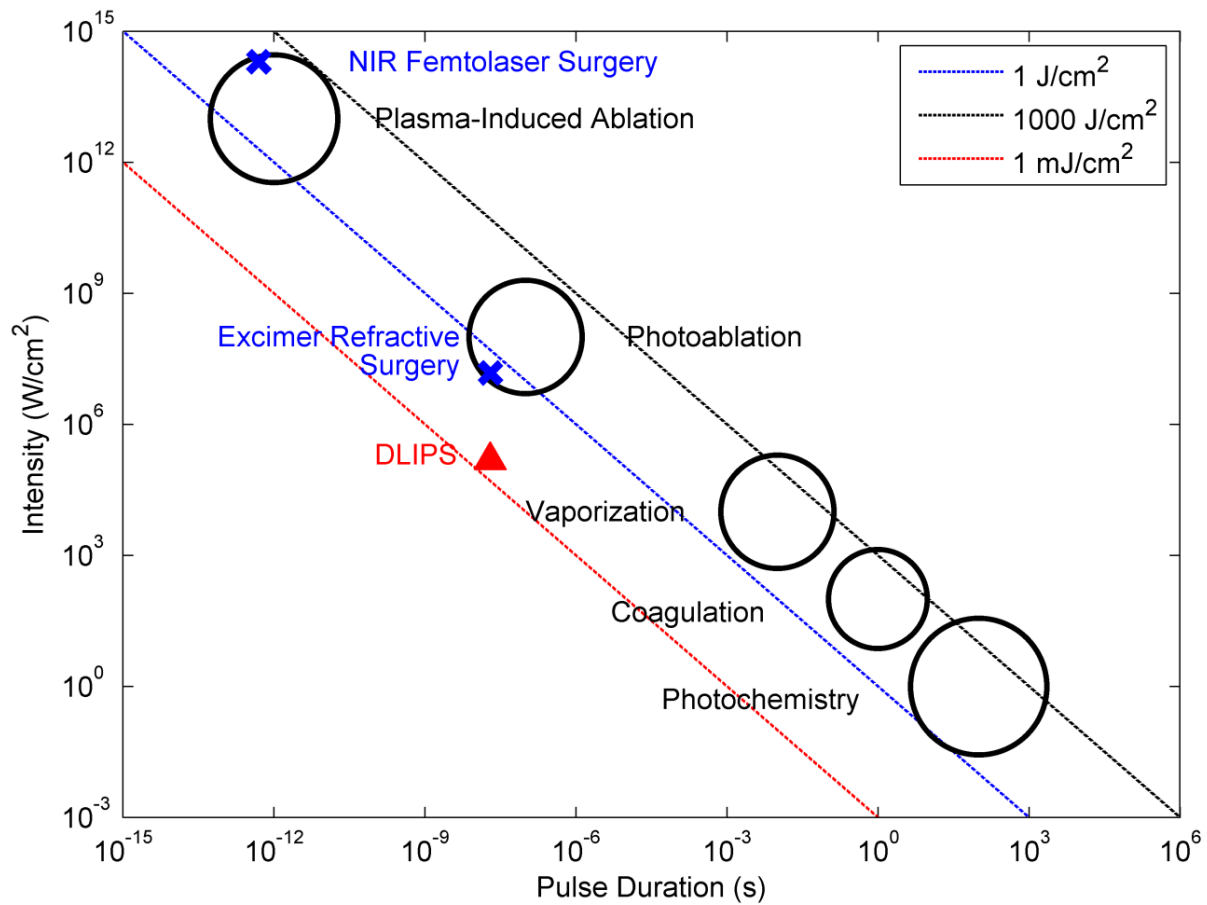


Figure 1-4. Laser-tissue interaction possible as a function of exposure time and irradiance [Modified from Boulnois JL. Photophysical processes in recent medical laser developments: a review. Laser Med Sci. 1986; 1:47-66]

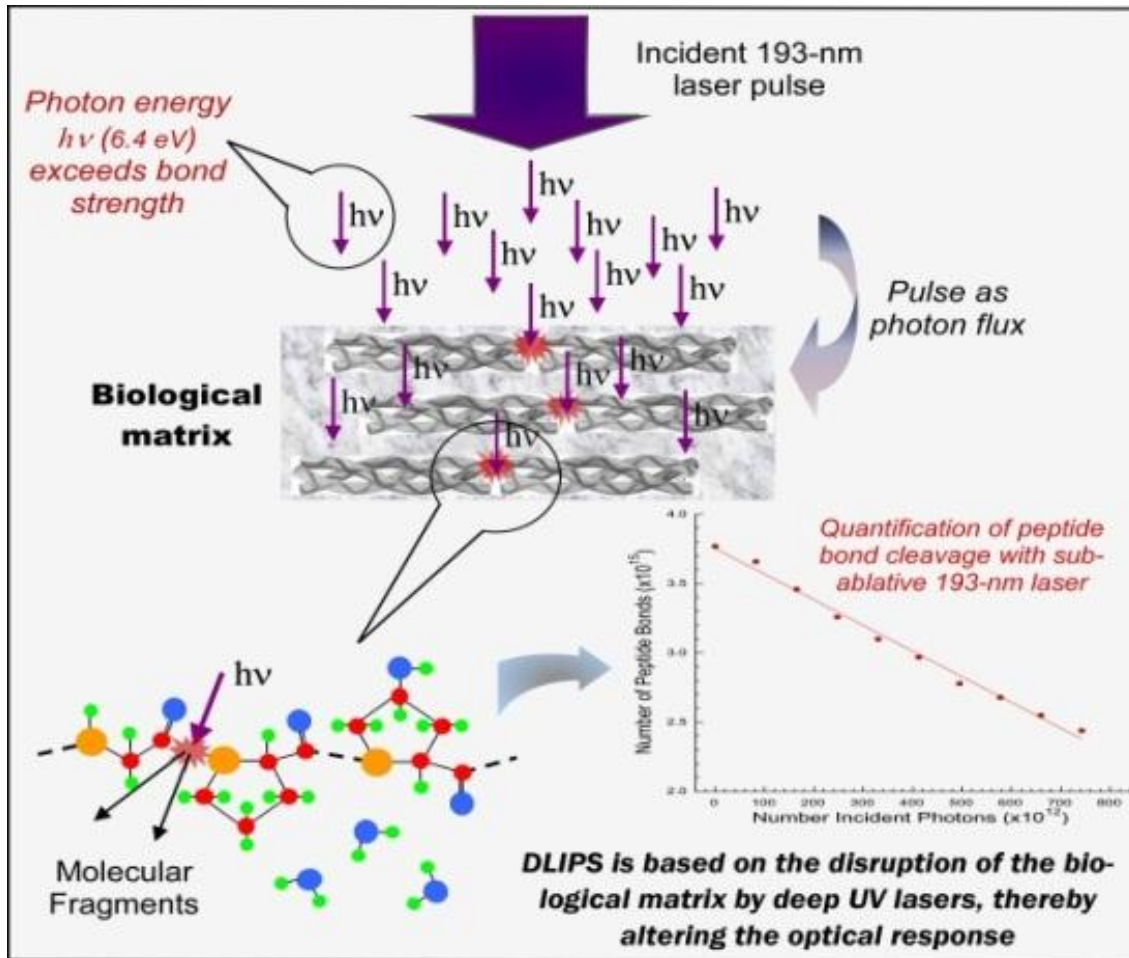


Figure 1-5. Cleavage of peptide bonds due to direct photolysis induced by absorbance of 193 nm photons from an excimer laser source [Unpublished figure, used with permission, David Hahn, 2012]

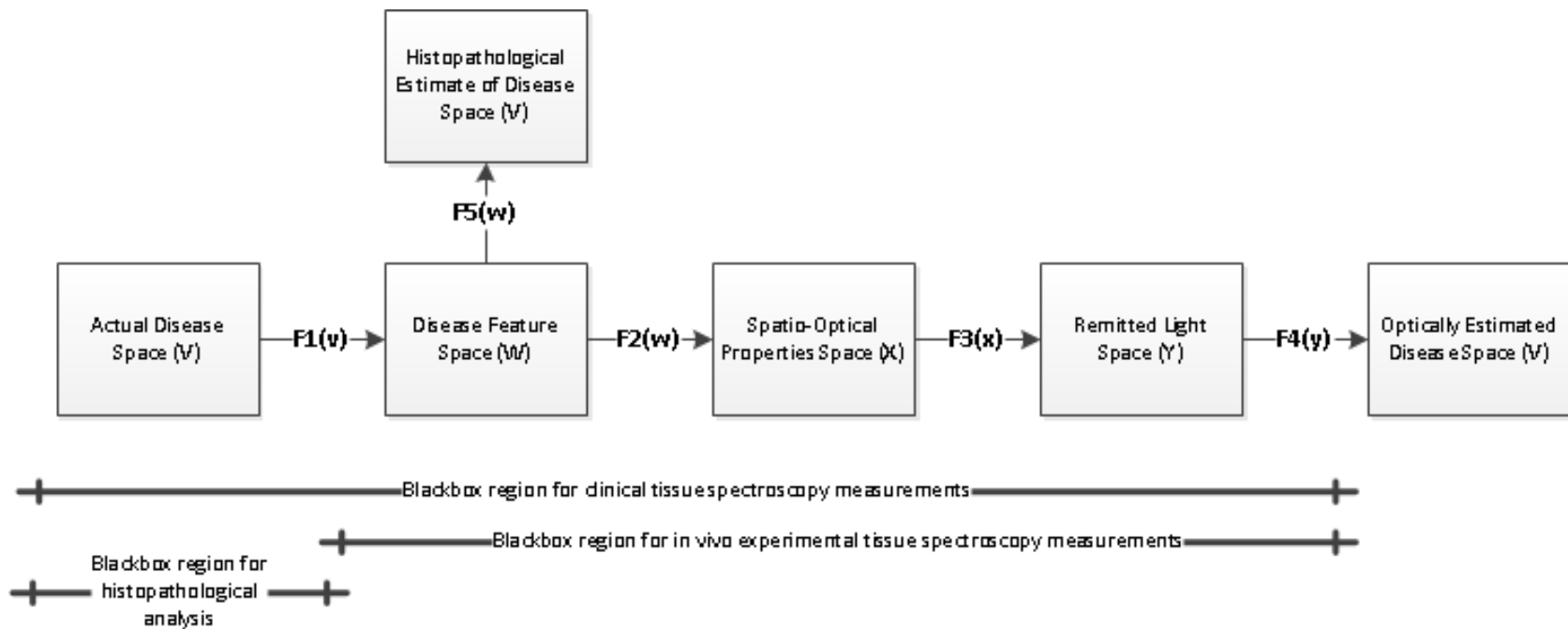


Figure 1-6. Signal propagation and transformation map for non-invasive optical diagnosis of disease

## CHAPTER 2 COMPARATIVE EVALUATION OF DIFFERENTIAL LASER-INDUCED PERTURBATION SPECTROSCOPY AS A TECHNIQUE TO DISCRIMINATE EMERGING SKIN PATHOLOGY

### Motivation

Biophotonics, the study of interactions between light and biological samples had its earliest applications in diagnostic medicine with the use of optical microscopy to study tissue samples and histological specimens.<sup>39</sup> Since that time, advances in optical technologies have spurred the creation of increasingly sophisticated instruments to study tissue for research and in the laboratory, with a particular focus on the early detection of cancer. Fluorescence-based techniques have been developed to probe the endogenous fluorophores of tissue including collagen, nicotinamide adenine dinucleotide (NADH), flavins, and porphyrins.<sup>40</sup> Through the study of these endogenous markers, it has been shown that these molecules are correlated with certain pathological conditions and have unique distributions in tumors, and that these fluorescent molecules can be used to distinguish benign from malignant tumors.<sup>26, 27</sup>

Generally, fluorescence spectroscopy is a nondestructive and sensitive technique that allows *in vivo* detection of organic and biological materials under different environmental conditions in very short times. Because the excitation/emission wavelength pair is a combination of the molecular structure and the overall molecular environment (e.g. biological matrix), fluorescence emission may provide discrimination among emitting materials.

---

Reprinted with permission from: R. T. Kozikowski, S. E. Smith, J. A. Lee, W. L. Castleman, B. S. Sorg, and D. W. Hahn, "Differential laser-induced perturbation spectroscopy: demonstration of a new spectroscopic technique in a murine model of emerging skin pathology," *Journal of Biomedical Optics* **17**, 067002 (2012).

Despite the long-standing utility of biophotonics-based strategies in the laboratory, these advanced technologies are only beginning to be applied in the clinic. Epithelial tissues, often easily accessible or with minimal invasiveness via endoscopy, have been targets for the majority of clinical techniques employing tissue autofluorescence imaging or spectroscopy. This includes the detection of gastrointestinal cancers and diseases, colorectal cancer screening, and oral oncology.<sup>41-43</sup> Additionally, there are ongoing clinical trials evaluating novel fluorescence techniques such as fluorescence lifetime imaging, multiphoton imaging, hyperspectral imaging, enzyme activity imaging, and single molecule detection for *in vivo* diagnostic applications.<sup>39, 44</sup>

Each of these strategies leverages measurement of intrinsic optical properties from superficial tissue layers to assay the presence of disease, or the potential for development. The promise of these optical diagnostic strategies, however, has been marred by high false positive rates when applied to *in vivo* clinical screening and diagnosis.<sup>45</sup> Consequently, following screening, biopsy of suspect lesions followed by histopathological analysis under visible light microscopy remains the gold standard for disease state confirmation in a large proportion of cancers.<sup>46-48</sup> This has resulted in a slow maturation process for point-of-care biophotonics and can be attributed to several limiting factors inherent to the complexities of the clinical setting.

Common to spectra taken from complex samples, high intensity, broadband fluorescence responses from tissue often obscure the rich biomolecular information found in lower intensity fluorescence emission bands. As this broadband response could potentially be from a tissue fluorophore unrelated to disease, targeting specific biomarkers of disease has been challenging using these techniques. However, the

largest hurdle to surmount in translating these spectral strategies to the clinic has been the significant patient-to-patient variation in fluorescent properties.<sup>49, 50</sup> This has been shown to be associated with race, age, sex, air temperature, and even deformation of the tissue when applying the probe.<sup>49, 51-57</sup> The results of this patient and sampling variability includes: fluctuations in absolute emission intensity, emission peak shifts, and changes in the scattering and absorption properties of the tissue, among other effects.<sup>49, 57</sup> Brookner<sup>49</sup>, for example, reported variations in peak fluorescence intensities varying by more than a factor of five between patients while the intra-patient coefficient of variation was less than 25%. While fluorescence signals are directly linked to the local molecular structure of the targeted system, there clearly remains a need for further improvement in optical-based sensing schemes to specifically address the variations realized with absolute fluorescence intensity.

In this paper we present the first application of a new spectral technique, differential laser-induced perturbation spectroscopy (DLIPS), to the *in vivo* detection of epithelial pathology in an animal model.<sup>36, 37</sup> The DLIPS sensing scheme incorporates three complementary techniques to improve upon previous fluorescence-based biosensing strategies: laser-induced fluorescence emission, ultraviolet (UV) laser perturbation of tissue, and difference spectroscopy.<sup>36</sup> In this instance, fluorescence is used to measure the response of tissue fluorophores before and after the tissue is laser-perturbed. The perturbation pulses from the deep-UV excimer laser (193 nm, 6.4 eV) are strongly absorbed by biological tissue and used to cleave molecular bonds within the extracellular matrix (ECM) as shown schematically in Figure 2-1. Irradiation of biological matrices at 193 nm can cause photoionization, including strand breakage,

locally denatured sites, interstrand cross-linking, reactions via photo-hydrates,  $\pi$ -dimers, and other products.<sup>33</sup> In the current work, despite being well below the intensity threshold for tissue ablation, permanent alteration of the underlying tissue structure is induced, with resulting changes within the fluorescence spectrum, specifically with respect to photoreactive biomolecules, as made apparent with the DLIPS scheme. We note here that while no direct ablation is realized, a single photon of 193 nm radiation exceed nearly all bond energies in the biological matrix; hence permanent photochemistry is induced despite being below the critical photon flux to affect material removal. Additionally, because the pre- and post-perturbation spectra are combined (see Equation 2-1) into a *difference spectrum*, the DLIPS technique mitigates unwanted contributions from unperturbed tissue fluorophores, broadband fluorescence, and importantly, variations in fluorescence emission bands which are unique to the patient, but not necessarily to the targeted pathology. Equation 2-1 shows the DLIPS spectral response, namely:

$$DLIPS(\lambda) = \frac{Em_{post}(\lambda) - Em_{pre}(\lambda)}{Em_{pre}(\lambda)} \quad (2-1)$$

where  $Em_{pre}(\lambda)$  and  $Em_{post}(\lambda)$  represent the fluorescence emission intensity recorded at each wavelength before (pre) and following (post) perturbation by the UV excimer laser, respectively. As defined, a negative DLIPS signal corresponds to a reduction in fluorescence intensity following the photo-perturbation step, which is generally attributed to the destruction of a corresponding fluorophore. In contrast, a positive DLIPS signal corresponds to an increase in fluorescence intensity following perturbation, which may indicate destruction of a fluorescence-quenching species and/or the destruction of a concomitant absorbing compound, thereby allowing more

light to reach the actual fluorophore. Overall, the complexity of the local fluorescence environment provides the opportunity for the perturbing UV radiation to affect a unique change to the resulting fluorescence response. Therefore, this combination of fluorescence, photochemical perturbation, and differential spectroscopy creates a completely unique spectral signature from targeted tissue. The result is a technique that specifically couples to important photosensitive tissue biomarkers of early pathological changes and that has promise to mitigate the apparent noise sources due to inter-patient variations.

The primary goal of this study is to characterize and evaluate the DLIPS biosensing technique using an animal model of epithelial pathology. Using principal component analysis and a simple Hotelling's  $T^2$ -test, we demonstrate that this technique can detect changes in epithelial tissue *in vivo*. Further, we show via component loading analysis that this technique couples specifically to morphological changes in the ECM, which is unique compared to laser-induced fluorescence. Using detection theory analysis of unprocessed principal component data we show that DLIPS is an inherently more robust technique for assaying the presence of pathology in this animal model compared to conventional laser-induced fluorescence alone. Finally, to demonstrate the utility of the DLIPS technique in complementing existing diagnostic techniques, we employ decision fusion with laser-induced fluorescence to further boost performance when detecting the pathological state.

## **Materials & Methods**

### **DLIPS System**

The DLIPS system is shown schematically in Figure 2-2. For all measurements, fluorescence excitation was accomplished using a Q-switched, frequency-tripled

Nd:YAG laser, while the UV perturbation was accomplished using a 193 nm ArF excimer laser. The 355 nm fluorescence excitation beam was aligned coaxially with the 193 nm perturbation laser using a dichroic mirror (193 nm) as a beam combiner. Prior to the beam combiner, a variable attenuator was used to reduce the excimer laser to the desired perturbation intensity. The 355 nm beam diameter was about 30% less in diameter than the 193 nm beam (top-hat beam profile) at the target plane, to ensure complete perturbation of the entire fluorescence probe volume. The co-linear laser beams were passed through a pierced mirror positioned at  $45^\circ$  to the target plane. With the 355 nm beam incident on the target, fluorescence emission was redirected by the pierced mirror and then focused onto a fiber optic bundle using a combination of two 50 mm diameter UV-grade lenses, where it was passed to a 0.3 m Czerny-Turner spectrometer and recorded with an intensified CCD (ICCD) array detector. Prior to entering the fiber optic, two sharp-edge filters were used in series: a high-pass filter designed to block the residual 355 nm light, and a low-pass filter designed to block any residual 532 nm light remaining from the frequency-tripling process. With this system, fluorescence emission was successfully collected in the spectral window between about 390-500 nm. A digital delay generator was also used to synchronize and control both the ICCD and the 355 nm laser, and a 3  $\mu$ s detector gate was used to collect the fluorescence, set to correspond to the leading edge of the 355 nm laser pulse (20 ns full width); hence all prompt and delayed fluorescence was recorded. Additional experimentation revealed that the majority of fluorescence emission corresponded to the first 100 ns of the detector gate.

## **Chemical Initiation and Promotion of Mouse Skin Tumors**

Protocols were approved by the University of Florida Institutional Animal Care and Use Committee. Tumor formation on female athymic nude mice (Hsd:Athymic Nude-*Foxn1<sup>nu</sup>*, Harlan Laboratories, Indianapolis IN), six to eight weeks old, was induced and promoted by 7,12-dimethylbenz(a)anthracene (DMBA) (Sigma-Aldrich, St. Louis MO) in mineral oil (Fisher Scientific, Pittsburgh PA) at a concentration of 0.5% w/w applied topically to the dorsal skin according to previously described methods.<sup>58-64</sup> Application was repeated two to three times per week throughout the 11 week course of the experiment. DMBA application was discontinued if mice began exhibiting signs of systemic toxicity, particularly weight loss. In all cases, cessation of topical application resulted in alleviation of toxicity symptoms. Further, all of these mice showed visible lesions during week eight, consistent with those mice who continued receiving topical DMBA. Topical application of mineral oil alone was used on the control mice. The protocol was terminated at 11 weeks, prior to the emergence of squamous cell carcinomas (SCCs) as the goal of the study was not to investigate the biological difference between cancerous and normal tissue but rather to investigate DLIPS potential as a precancerous diagnostic technique. Thus tissue comparisons were made between healthy tissue and tissue during the course of SCC formation due to DMBA initiation and promotion.<sup>59, 60</sup>

## **Histopathology**

At weeks four and eight, one mouse was selected from the control group as well as the DMBA-treated group and euthanized using an intraperitoneal injection of Euthasol (Virbac AH, Ft. Worth TX). Likewise, the remaining mice were euthanized at the end of the study. Immediately following euthanasia, the dorsal skin was excised all

the way down to the anteroposterior axis and fixed in formalin (Sigma-Aldrich, St. Louis MO). Fixed samples were paraffin-embedded, sectioned at 5  $\mu\text{m}$ , and stained with hematoxylin and eosin (H&E). Tissue preparation was performed at the Cell and Tissue Analysis Core, McKnight Brain Institute, University of Florida (Gainesville FL). The sections were analyzed by a board-certified veterinary pathologist.

### **Collection of DLIPS and Fluorescence Spectra**

Starting in week two of the study, two control mice and two DMBA mice were selected at the beginning of each week for DLIPS and laser-induced fluorescence spectral analysis of the skin. Prior to all DLIPS spectral measurements, each mouse was wiped clean with an alcohol wipe and anesthetized using a ketamine/xylazine solution (Phoenix Pharmaceutical, St. Joseph MO; Lloyd Laboratories, Shenandoah IA) at 10 ml/kg of body weight. Each mouse was then positioned in an alignment holder and spectra were collected from the back of each mouse, two spots from each side of the mouse. For each spot, a fluorescence spectrum was recorded using a 200 shot ensemble average recorded at 5 Hz laser repetition rate, referred to as the pre-perturbation spectrum. Immediately following the pre-perturbation fluorescence measurement, the 193 nm excimer laser was used to deliver a total of 2500 perturbation pulses to the target spot with laser energy of 100  $\mu\text{J}/\text{pulse}$  (fluence = 3  $\text{mJ}/\text{cm}^2$ ) and a laser repetition rate of 50 Hz. Following perturbation, a delay of 30 seconds was introduced, after which a second fluorescence spectrum was recorded using an identical 200 shot ensemble average, referred to as the post-perturbation spectrum. These two spectra were then subtracted to generate the difference spectrum at each location, with the difference divided by the pre-perturbation spectrum to generate the DLIPS response for the given surface site. In this manner, a total of eight DLIPS

spectra (4 spots x 2 mice) were recorded each week from each group (control and DMBA). Despite the emergence of some lesions on the treated mice by week eight, all spectra were collected from skin regions that appeared to be pathology-free under visual inspection (i.e. visible lesions were avoided). Finally, the pre-perturbation spectra alone were retained and averaged separately for each group (control and DMBA) and week, providing traditional fluorescence spectral data to be analyzed independently of the DLIPS approach.

### **Multivariate Statistical Analysis**

At the conclusion of the study, all spectra were visually inspected and 22 individual spectra (~14% of the total collected) were rejected due to (1) excessive spectral noise and/or no observable difference in the pre- and post-perturbation spectra; indicative of low Nd:YAG laser and/or low perturbation laser intensity during the collection process, or (2) due to atypical spectral appearance (e.g. unusually large negative or positive perturbation) which is indicative of mouse movement (e.g. twitching) between the pre- and post-perturbation measurements. Following this process, the remaining spectra (pre-perturbation fluorescence and DLIPS) for both the control and DMBA groups were imported into MATLAB<sup>®</sup> (The Mathworks, Natick MA) for processing. Difference spectra and fluorescence spectra were preprocessed using a five-point moving average filter to remove acquisition noise. Fluorescence and DLIPS spectra were then analyzed separately, but using parallel methods, to facilitate side-by-side comparison at each analytical level. Spectra from the treated and control groups were grouped together in several different ways and analyzed using principal component analysis (PCA). Clustering within the data sets was visualized using score plots and the validity of using only the first two principal components for analysis was verified using a scree plot of the

principal components (cumulative variance explained greater than 95%). Sub-groups from the entire data set were selected for individual PCA to highlight the emergence of differences between the DMBA-treated skin and the untreated skin. For each PCA analysis, Hotelling's  $T^2$  test was used to verify that the clusters from the treated and control samples were statistically different.<sup>65</sup>

The component loadings from the first principal component were used to assess which spectral regions best explain variations within and between data sets.<sup>66</sup> Component loadings were squared to facilitate direct comparison of loading across wavelength regions between sub-populations of the data set (this casts each wavelength's loading value in terms of percent variance explained in the particular component). The regions of the spectrum at higher component loading levels were considered to have the highest impact on the observed differences between DMBA treated and control mice.

### **Detection Theory Analysis of Classification Performance**

To investigate the ability of the DLIPS technique to discriminate between healthy and pathological tissue, a likelihood ratio classifier was implemented as this has been shown to be the optimal detector to discover a signal in noise, irrespective of the type of data passed into it.<sup>67, 68</sup> Further, this classifier implementation facilitates direct performance comparison between laser-induced fluorescence and DLIPS without the need for the subjective evaluation of classifier appropriateness for one spectral technique versus another.

The spectral data set was first processed using PCA to reduce the dimensionality of the data and consolidate the majority of the variation in the first few resolved components. PCA was used because this change of basis maximizes the variance

across all of the data and does not require *a priori* knowledge of class associations. Due to the large percentage of variance explained by the first principal component for both the DLIPS and fluorescence spectra, as well as the limited size of the data set, detection theory modeling was restricted to decisions made using this first component. In this study, the null hypothesis ( $H_0$ ) was considered to be the absence of DMBA-induced pathology plus some noise (e.g. biological background, shot noise in the ICCD), while the alternate hypothesis ( $H_1$ ) was that a signal due to pathology is present in a noisy background, as shown in Equation 2-2.<sup>67</sup>

$$H_0 : X = N; \text{ no pathology markers} \quad (2-2)$$

$$H_1 : X = S + N; \text{ pathology markers present}$$

However, the overall inter-sample variance is assumed to be dominated by the presence or absence of the pathological state, not the noise. No prior knowledge of the data distribution under  $H_0$  or  $H_1$  was assumed and the distributions were approximated using kernel density estimation (bandwidth set using a Gaussian approximation) as  $P(X|H_0)$  and  $P(X|H_1)$  respectively.<sup>69</sup> The probability density functions were combined into a likelihood ratio and compared against a range of operating points ( $\tau$ ) to compute the receiver operating character (ROC) curves, as shown in Equation 2-3. For each operating point, the null hypothesis was rejected if the likelihood ratio was less than or equal to  $\tau$ . The classification rule was applied across the entire data subset under consideration to compute the false positive rate (FPR) and true positive rate (TPR) for the corresponding operating point, given by:

$$\Lambda(X) = \frac{P(X | H_0)}{P(X | H_1)} \leq \tau \quad (2-3)$$

To compare the inherent performance of the two spectral techniques, the area under the ROC curve (AUC) was used.<sup>70</sup> The maximum Matthews correlation coefficient (MCC) was evaluated as a basis for comparing “optimal” operating points between the two techniques as it provided equal weight to minimizing both false positive and false negative results.

Finally, a multi-modal pathology detector was designed using decision fusion in order to show the ability of DLIPS to complement traditional spectral techniques and boost the overall detection performance. Liao<sup>71</sup> and Jesneck<sup>67</sup> provide excellent reviews of the details for applying this technique to fuse multiple detectors as well as the benefits and limitations. The implementation employed here follows directly from Liao<sup>71</sup> without significant modification. Operating points for the local detectors were optimized by choosing the threshold that maximized the MCC. In this case, only the decisions from the DLIPS detector and the laser-induced fluorescence detector were used to create a fused detector. Performance was evaluated by calculating the AUC of the ROC for the fusion processor and comparing that to the performance of a single detector.

## **Results**

### **Histopathology**

Figures 2-3 (A-D) are representative photomicrographs of the H&E sections of the skin at four, eight, and eleven weeks of the study. The top left panel (Figure 2-3 (A)) is from a control mouse after week four of the study. There is normal epidermal thickness with several layers in the stratum corneum. Hair follicles and sebaceous glands are in normal density within dermal collagen and subcutis. Skin samples from control mice in subsequent weeks were comparable to the sample at week four. Figure 2-3 (B) shows

the skin after four weeks of DMBA treatment which displayed moderate epidermal changes including acanthosis and orthokeratotic hyperkeratosis, characterized by thickening of the stratum spinosum, stratum granulosum, and stratum corneum. Hair follicles were reduced in density and the dermis in treated areas was almost devoid of sebaceous glands compared to skin from control mice. At the same time dermal collagen density was increased. After eight weeks of topical DMBA application, skin was characterized by more severe acanthosis, orthokeratotic hyperkeratosis and dermal fibrosis than in skin after four weeks, as shown in Figure 2-3 (C). Hair follicles were infrequently found in treated areas, and sebaceous glands were almost completely absent. Squamous cell papillomas were occasionally present in the epidermis (although not shown in this section). At the conclusion of the study, week 11, the DMBA treated skin (Figure 3 (D)) showed more severe epidermal acanthosis and hyperkeratosis. There was also an increased, but still low density, scattering of squamous cell papillomas throughout the epidermis. Dermal fibrosis was slightly more severe than in samples from mice at eight weeks of DMBA treatment.

### **DLIPS and Laser-Induced Fluorescence Spectra**

Figure 2-4 (A-C) shows the average DLIPS spectra of the DMBA treated skin as compared to the control samples at weeks two, six, and eight. Figure 2-4 (D-F) shows the average of the laser-induced fluorescence spectra at the same time points, again comparing DMBA and control groups. Over the weeks of DMBA application, noticeable changes in shape of DLIPS spectra emerge (DMBA versus control), while these changes are not directly observable in the fluorescence spectra alone. Figure 2-5 shows individual (i.e. single mouse) spectral samples at the same time points of the study, illustrating the ability of the DLIPS technique to exploit internal normalization of

the spectra relative to the tissue, and thus revealing information about the underlying pathology. Both figures show the emergence of a noticeable band in the lower wavelengths of the DLIPS spectra throughout the pathological progression of the DMBA model. This information is either obscured or not detected using fluorescence alone, as the spectra from the skin (both control and DMBA-treated) are dominated by the broad, correlated fluorescence peak centered on 460 nm.

### **Multivariate Statistical Analysis**

Figure 2-6 (A, B) shows the score plots from the entire data set for the DLIPS data as well as the laser-induced fluorescence spectra. In both cases, 68 individual spectra were used from the DMBA-treated mice and 80 from the control mice throughout the eleven weeks of the study. For the entire DLIPS spectral data set the cumulative variance explained by PC1 and PC2 was 95% while these components explained 99% of the variance for the fluorescence spectra. For both data sets Hotelling's  $T^2$  test returned a p-value less than 0.001, confirming that the spectra collected from untreated mice are statistically unique from those collected from the DMBA-treated mice.

As an extension of this dimension reduction and remapping of the spectral data set into principal component space, the component loading were used to identify the important spectral regions in explaining the variance across the entire data set as well as several sub-populations of the data set. Figure 2-7 shows the proportion of variance in a given data set as a function of wavelength. PC1 was the only component considered since greater than 90% of the total variance in principal component space was accounted for in this component for all cases. Figure 2-7 (A-C) shows the proportion of variance using the DLIPS technique for the entire data set, the DMBA data subset, and the control data subset, respectively. Across all acquired spectra, the most

important regions in explaining the differences are: below 400 nm, a peak at 420 nm, and a region of increasing importance at wavelengths above 460 nm. Additionally, when the control spectra and DMBA-treatment spectra are analyzed separately, unique band regions emerge to potentially explain the observed pathological progression to lesion formation in the DMBA model as opposed to the skin from the control mice. Primarily, the DMBA-treated skin has an important band between 400 and 420 nm, while the control skin's band is below 400 nm. Although neither of these sub-populations shows much loading above 460 nm, the entire data set shows significant variability above this wavelength. This implies that this region may specifically account for variability between control and DMBA-treated skin using the DLIPS technique.

Remarkably, the region around the peak fluorescence emission is of minimal importance using the DLIPS technique, a dramatic contrast to the component loadings for the traditional laser-induced fluorescence spectra across the same data sets (Figure 2-7 (D-F)). The fact that the shape of the component loading map closely resembles that of the fluorescence spectra is indicative of a strong dependence on intensity fluctuations at the peak emission wavelength in describing variations across the data set. Further, there are no unique spectral regions within either the DMBA-treated or control groups when compared to the loadings from the entire data set. This sensitivity to signal intensity highlights an important limitation of traditional *in vivo* fluorescence techniques, namely, that subject-to-subject variability can often obscure the relatively much smaller variability due to changes in tissue autofluorescence.<sup>49</sup> Finally, Figure 2-7 (G-I) shows the same technique applied to the spectra collected after the perturbation laser pulse. This analysis was applied to this data to assess whether any new

information gained from applying the differential technique is unique to DLIPS, or merely inherent to the post-perturbation fluorescence spectra. Not unlike the component loadings for laser-induced spectra, these resemble the shape of the acquired fluorescence spectra, indicating that the most significant feature is the variability of the intensity of the broad fluorescence peak fluorescence centered at 460 nm. Again, the component loadings are the same across all three figures, indicating limited coupling of these spectra to underlying tissue biomolecular structure.

### **Pathology Detection Performance**

Using the same compressive transformation as above, sub-populations of the data set were compared to describe the ability of each technique to discriminate the pathological (or pre-pathological) state from normal skin. In this case, only the first principal component was considered due to the small size of the sub-populations used in classifier construction. Specifically, the spectral data was partitioned into “early” (week 2-4), “middle” (week 5-8), and “late” (week 9-11) segments, based upon the visual observation of similar pathological states within those time periods for the DMBA-treated mice. The “early” DMBA-treatment group was considered pre-pathological as both observational and histological evidence showed only the earliest stages (inflammation and hyperplasia) of development. The “middle” and “late” periods were considered definite-pathological because dysplastic lesions and papillomas were visible during those periods of the study. PCA was performed independently on all of the data (DMBA treated and control) for the given time periods. Figure 2-8 shows the ROC curves derived from the likelihood ratios computed using the DLIPS technique, and Figure 2-9 shows the curves for laser-induced fluorescence. With the exception the “early” time period, detection performance using the DLIPS technique was considerably

better than using laser-induced fluorescence, as measured by calculating the AUC for each ROC curve. Even during the “early” stage of pathology development, which we note is considered pre-pathological, the DLIPS technique only lagged fluorescence by 2.5%. However, during the “middle” and “late” stages, DLIPS showed a 29.79% and 5.01% improvement in detection performance, respectively. In addition, Table 2-1 shows the sensitivity and specificity at the “optimal” operating points for these pathology detectors, assuming an equal weighting for false negatives and false positives. This table shows that for DLIPS, as the pathology matures, the specificity of detection stays at a high level while the sensitivity improves. On the other hand, when laser-induced fluorescence is used the sensitivity still improves, but at the expense of specificity. Thus, even when the detection performance of these techniques is optimized using an off-the-shelf classification scheme (i.e.: artificial neural network, linear discriminant analysis, etc.), the information encoded using DLIPS is more robust than traditional fluorescence spectroscopy and offers improved discrimination when detecting pathology.

As evidenced above using component loadings, the DLIPS spectra and fluorescence spectra emphasize unique spectral regions and features. Assuming this means that these spectra reflect different underlying biological changes, or at the very least some amount of statistical independence between the two techniques, the DLIPS technique was combined with laser-induced fluorescence to improve the overall detection performance.<sup>67, 71</sup> Figure 2-10 shows the ROC curve for this fused classifier as well as the ROC curves for the local detectors with the operating points used to create the fused classifier labeled. When used to evaluate the “late” data set, the AUC

is improved by 11.70% over detection using laser-induced fluorescence alone. Based upon these results, DLIPS may serve as a new dimension in the composite evaluation of pathology for *in vivo* detection and diagnosis applications.

### **Discussion**

In this study, we investigated a new spectral technique, DLIPS, and evaluated its applicability to detecting pathological changes in a murine model. Our findings show preliminary support for applying this technique as a stand-alone medical diagnostic tool or as a complementary technique to traditional fluorescence spectroscopy for the detection of pathology *in vivo*. Of particular note were the findings that the DLIPS spectra emphasize different spectral regions from the laser-induced fluorescence spectra and that the endogenous pathology detection potential for DLIPS shows superior performance when compared to laser-induced fluorescence alone in this study.

As has been shown before, the strong fluorescence peak centered on 460 nm for the fluorescence spectra (Figures 2-4 and 2-5) can most reasonably be assigned to the tissue fluorophore NADH.<sup>26, 72-74</sup> While this is an important tissue fluorophore, and is a primary target of fluorescence tissue assessment, it serves as a marker of increased cellular metabolism, which is a hallmark of dysplasia, but not necessarily unique to it. In conjunction with increased cellular metabolism, one of the earliest markers of pre-cancerous progression is cellular infiltration and the release of growth factors and cytokines. This unchecked cellular signaling results in the proliferation of fibroblasts, increased collagen synthesis, and suppression of collagenase production, with the overall effect of restructuring the local ECM.<sup>75</sup> These effects suggest that techniques which target collagen remapping might provide direct diagnostic coupling of the spectra to the pathology. Figure 2-7 (A) shows that this spectral region, up to 420 nm, was the

most prominent region in explaining the variance when using DLIPS, and is in the range for emission due to collagen.<sup>26, 72-74</sup> This agrees with previous work showing that excimer laser pulses can break collagen amide bonds, resulting in a pronounced difference spectrum band.<sup>36, 37</sup> Further, when PCA was performed independently on the control spectra and the DMBA treated spectra (Figure 2-7(B, C)), a unique collagen region emerges in each case, at lower wavelengths for control skin and at higher wavelengths for DMBA-treated skin. This region of higher variability is likely due to the progression of ECM remodeling associated with pre-cancerous lesion formation throughout the 11 weeks of the study for the DMBA-treated skin. As for the control skin, this region of higher variability could be due to the aging-related remodeling of skin or the natural turnover of skin ECM proteins.<sup>49, 53</sup> In this regard, DLIPS serves as a convenient probe for ECM structure that was previously inaccessible when exciting natural fluorescence at 355 nm, as it has been noted that at this excitation wavelength it is not possible to resolve collagen fluorescence from that of NADH.<sup>76</sup> Our component loading plots for the laser-induced fluorescence spectra and the post-perturbation spectra (Figure 2-7(D-I)) illustrate this effect as the variation is most strongly tied to the intensity of the broad NADH peak at 460 nm. The other important spectral region in distinguishing DLIPS spectra is above 460 nm. This band of increasing importance up to 500 nm is not clearly assignable to metabolic or structural fluorophores, but is definitely a point of contrast between DMBA-treated and control skin as it only shows up in the combined spectral pool (Figure 2-7(A)). The proximity to the 460 nm NADH peak could indicate it is simply a residual region from that emission but further work will be

required to isolate the molecular source of this DLIPS region and assess its diagnostic strength.

The DMBA model of pathogenesis has been well characterized, particularly with regard to *in vivo* models for the evaluation of fluorescence-based techniques to detect and diagnosis cancerous and pre-cancerous lesion formation.<sup>59, 60, 74</sup> While our study found improved performance using the DLIPS technique, other studies have reported accuracy rates up to 90% for detecting precancerous morphological changes and sensitivities and specificities ranges of 76-95% and 83-95% respectively when using fluorescence spectroscopy.<sup>59, 74, 77, 78</sup> However, a major difference of these studies was the focus on an algorithmic approach to boosting detection performance using techniques like partial least squares discriminant analysis or a support vector machine to develop a maximized basis on which to separate the data and subsequently only resolve a single detection operating point.<sup>60, 74, 79</sup>

In diagnostic medicine, there is often a much greater cost associated with a false negative result as opposed to a false positive, as evidenced by the high sensitivities and low specificities reported for physician-driven diagnostic techniques.<sup>47</sup> Thus, an understanding of the entire performance curve is critical, as different applications may require operating far from the optimal decision threshold in order to boost either sensitivity or specificity. In our work, a technique-driven investigational study, PCA was employed allowing the inherent variance of the data to be the factor across which the dimensionality was reduced and the data were separated. This permitted a probing of the primary source of variation; the emerging pathology or noise. Since the tissue under investigation in this study was not actual spontaneous human lesions (*in vivo* or

otherwise), development of a discriminant model to improve detection was not considered, as it must be derived from the intended target, but will be implemented when appropriate in future work. Despite this significant difference in change of basis methodology, the performance metrics reported in Table 2-1 indicate that this technique has at least comparable detection performance to previously reported fluorescence studies in DMBA-induced model pathology. However, when translating results to actual clinical use, performance of fluorescence spectroscopy is reported to drop to 70-82% sensitivity and 68-92% specificity.<sup>79, 80</sup> This is most often attributed to patient-to-patient variability and is a known confounding factor for clinical *in vivo* fluorescence measurements. Although multiple standardization and normalization techniques have been proposed to combat this issue, it necessarily comes at the cost of lost information from the collected spectra.<sup>60</sup> Our results in Figure 2-9 support this notion that without a normalization strategy, emission spectra can vary widely due to factors other than changes in the underlying pathological condition. The severe drop in performance for identifying pathology during weeks five through eight is likely due to emission fluctuations associated with the data collection process or the particular spots being interrogated on the back of particular mice. In the case of DLIPS, the spectra represents a *differential response* measurement from the same location and is in that sense self-referencing in order to specifically remove variation associated with inter-sample differences. Figure 2-8 supports this stabilization of measurement as it shows the detection performance improving uniformly with the maturation of the DMBA-induced pathology.

Irrespective of the diagnostic performance of this technique using a model of pathology, or how that compares to other techniques, DLIPS still provides a new spectral dimension with which to investigate epidermal pathology. As more diagnostic tests and techniques become available, there is an increasing trend in medicine toward boosting the performance of pathology detection by combining disparate data sets from multiple unique sources. Although this can be a challenging problem, techniques from the bioinformatics and machine learning communities can be applied to optimally fuse this information.<sup>67, 81-83</sup> In the case of DLIPS, its largest impact may be in offering a new source of unique information about the ECM to be processed along with multiple other markers of disease. Our preliminary findings (Figure 2-10) fusing this technique with fluorescence spectroscopy shows that improvements in diagnosis can be realized by combining this technique with other independent biomarkers for the target pathology. We note an additional point in regard to the DLIPS technique in the context of orthogonal sensing, namely, that the scheme is readily implemented with Raman spectroscopy as the primary optical scheme.<sup>36</sup> In other words, Raman spectra are recorded pre- and post-perturbation, and the difference Raman DLIPS spectrum is then calculated in the same manner as done with a fluorescence probe.

In summary, our work here presents a promising preliminary evaluation of DLIPS for the *in vivo* detection of disease. We succeeded in revealing the underlying sources of physiological contrast to which DLIPS is sensitive and also established the baseline performance of DLIPS in detecting pathological changes. Applying identical data collection and evaluation techniques, DLIPS showed superior detection performance when compared to laser-induced fluorescence spectroscopy. Future work will include

the refinement of this technique in subsequent animal studies, application of the DLIPS technique to other spectral domains, further investigation of the endogenous chromophores responsible for the spectral changes under DLIPS detection, with the long-term goal of translating this technique to the clinic.

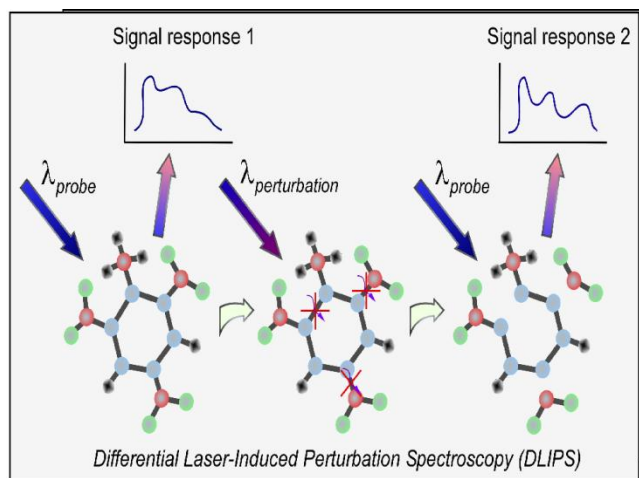


Figure 2-1. DLIPS acquisition scheme

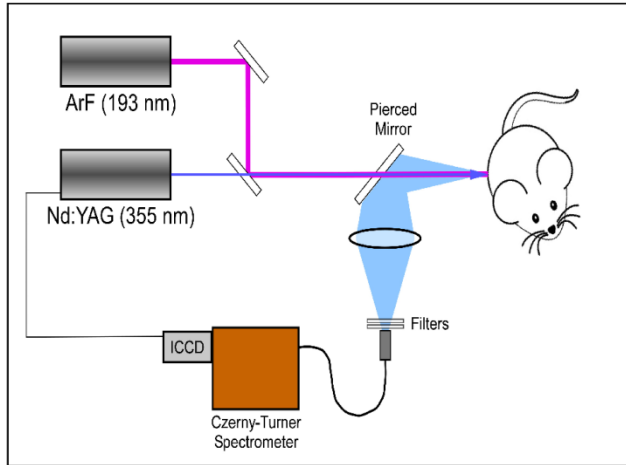


Figure 2-2. Schematic of the DLIPS system

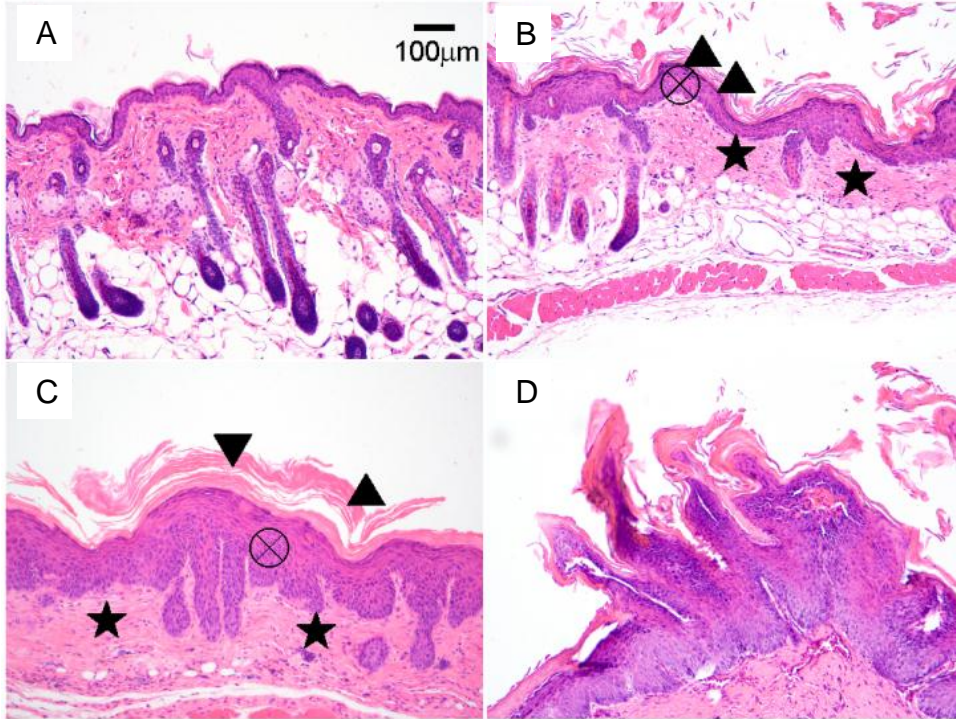


Figure 2-3. H&E stained histology sections of skin. A) Control mouse, week 4. B) DMBA mouse, week 4. C) DMBA mouse, week 8. D) DMBA mouse, week 11. (▲) denotes thickened regions of the stratum corneum, symptomatic of orthokeratotic hyperkeratosis. (X) highlights the thickening of the stratum spinosum, characteristic of acanthosis. (\*) denotes areas of increased dermal collagen density. D) a section through a developed papilloma.

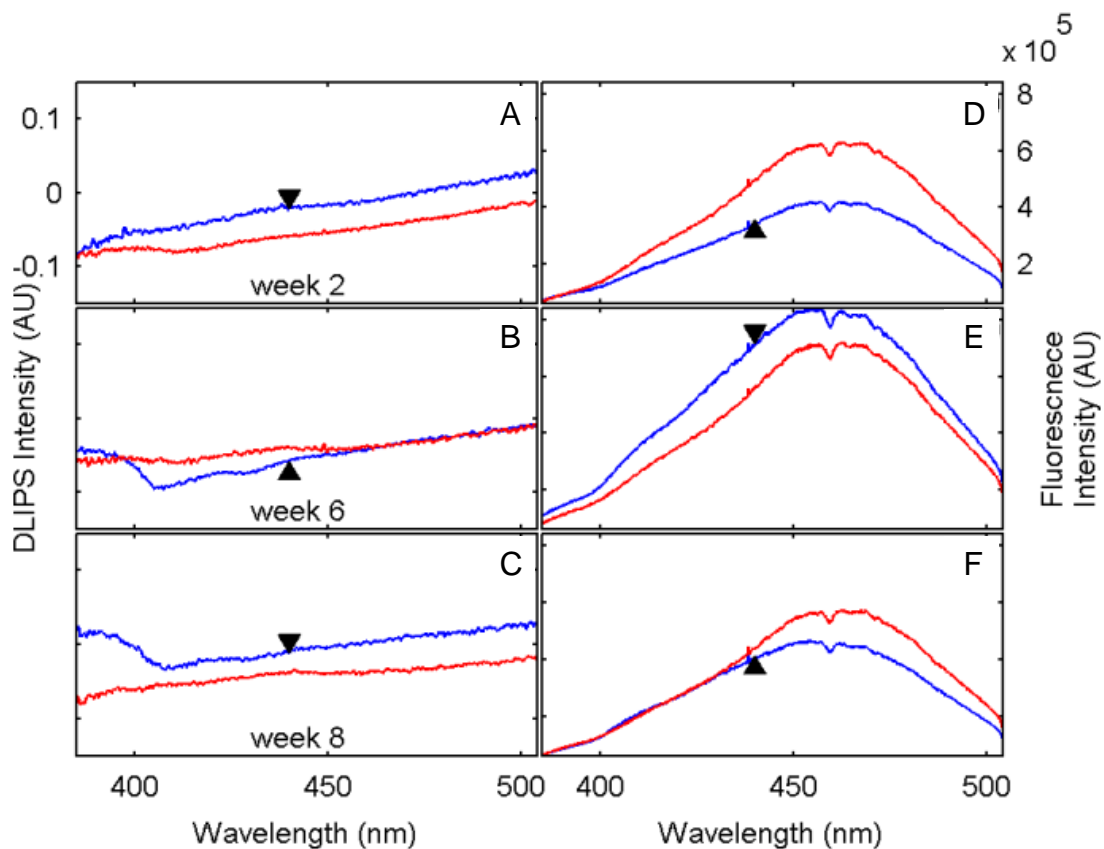


Figure 2-4. Average spectra at weeks two (n=6, 7), six (n=5, 4), and eight (n=7, 8). A-C) DLIPS. D-F) normalized fluorescence. (▲) denotes DMBA-treated skin and untreated skin spectra are unlabeled.

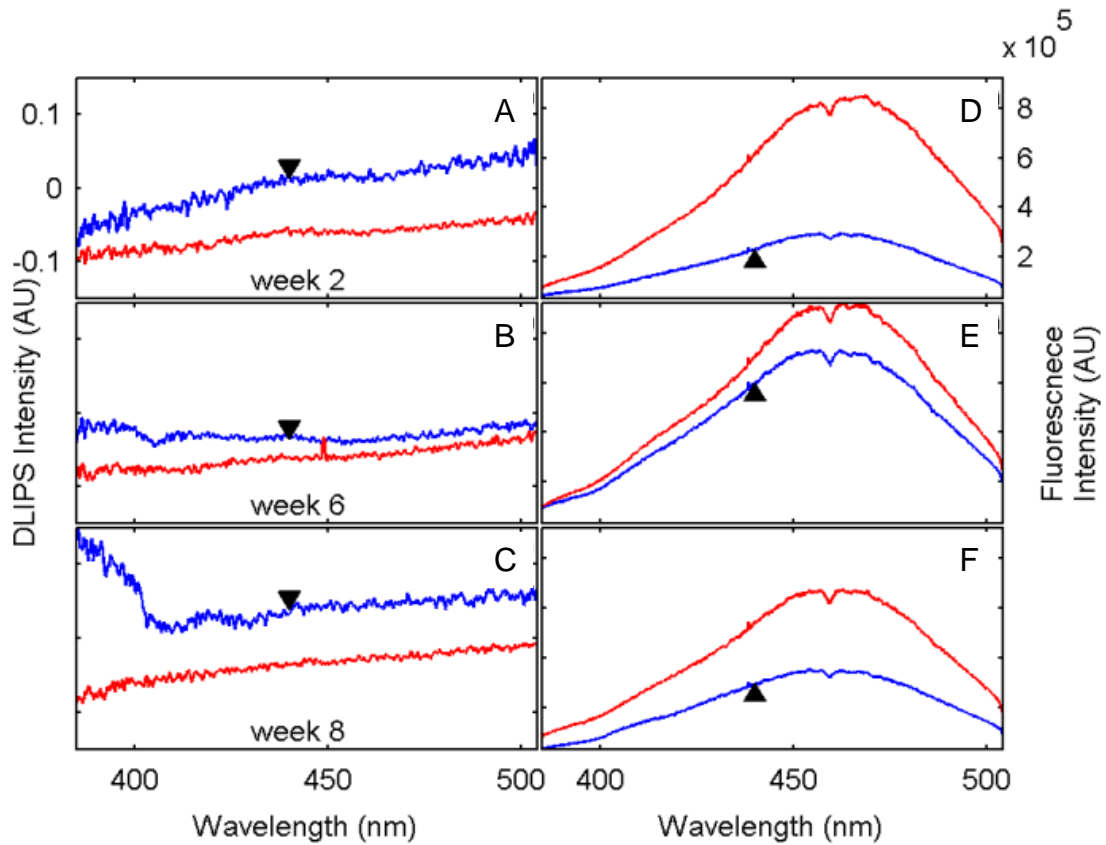


Figure 2-5. Spectra at weeks two, six, and eight. A-C) DLIPS. D-F) fluorescence. All measurements from the same spot on the backs of DMBA-treated (▲) and untreated mice

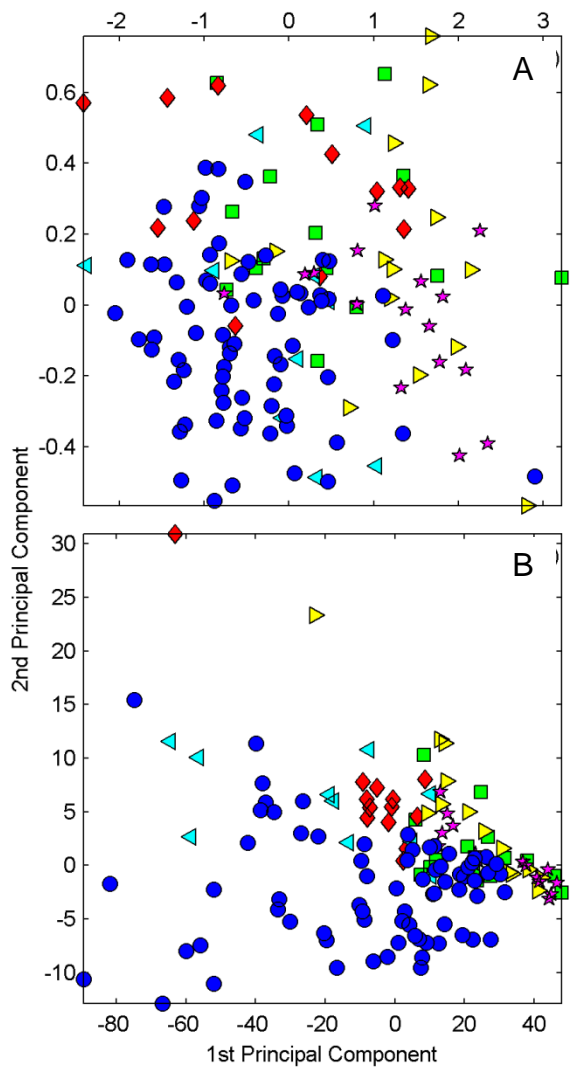


Figure 2-6. Score plots for the principal component analysis. A) DLIPS. B) Laser-induced fluorescence. All spectra from week two to eleven of the study. Control (●), DMBA-treated weeks 2 & 3 (■), weeks 4 & 5 (◆), weeks 6 & 7 (◄), weeks 8 & 9 (►), weeks 10 & 11 (\*)

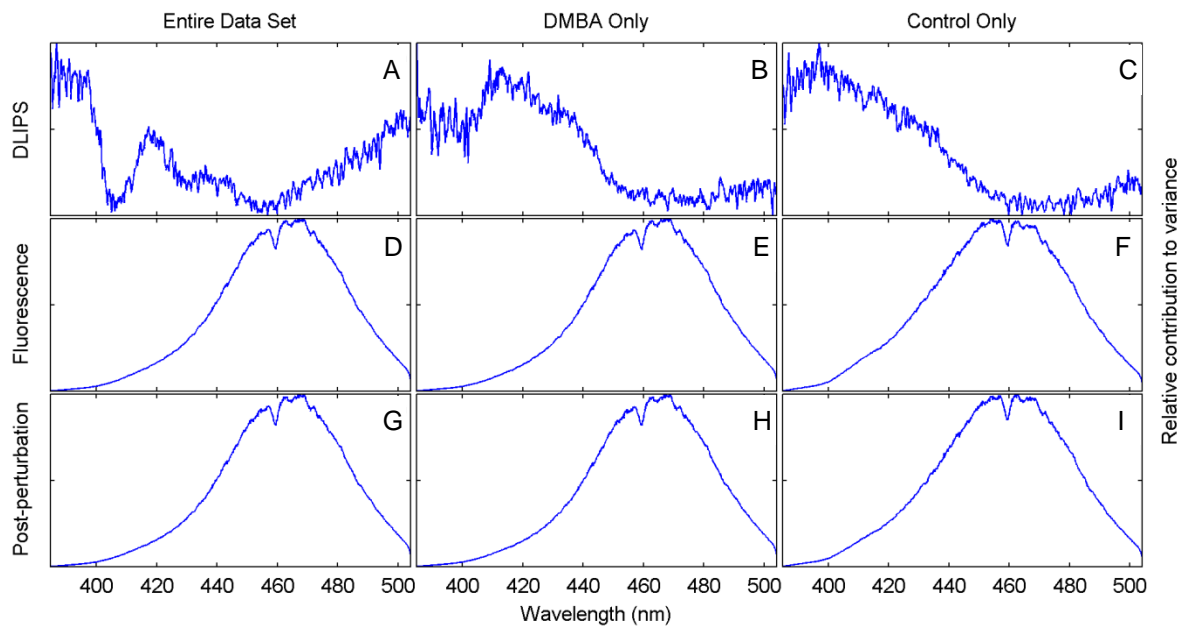


Figure 2-7. Proportion of variance in Principal Component 1 accounted for by each wavelength. A-C) DLIPS spectra. D-F) Laser-induced fluorescence spectra. G-I) Post-perturbation spectra. In each row, the leftmost plot considers the variation across the entire data set, the middle plot represents the variation from only from DMBA-treated mice and the right plot represents variation within the control data.

Table 2-1. Detection performance metrics using DLIPS, laser-induced fluorescence, or a decision fusion approach.

	Early (wk 2-4)		Middle (wk 5-8)		Late (wk 9-11)		Fused
	DLIPS	Fluorescence	DLIPS	Fluorescence	DLIPS	Fluorescence	
AUC	0.734	0.755	0.835	0.643	0.913	0.869	0.971
Sensitivity	0.429	0.524	0.783	0.870	0.833	1.000	
Specificity	0.957	0.913	0.815	0.593	0.955	0.727	

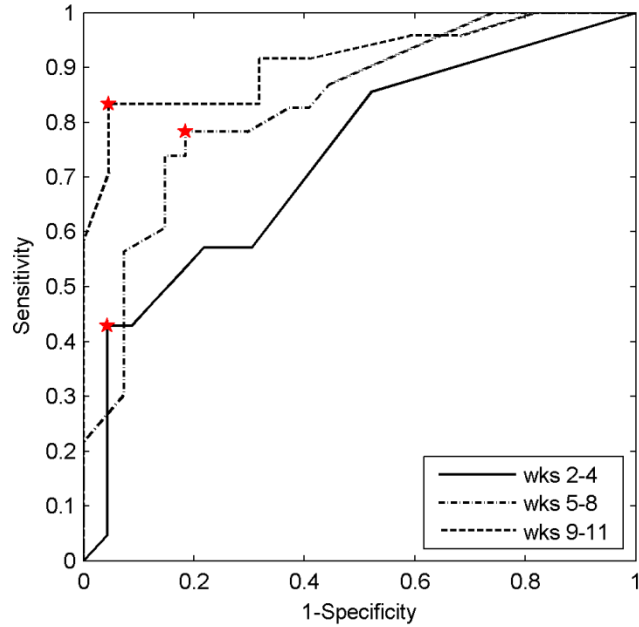


Figure 2-8. ROC curves for the detection of DMBA-induced skin pathology using the DLIPS technique. The data set was partitioned into early (weeks 2-4), middle (weeks 5-8), and late (weeks 9-11) time periods of papilloma development resulting from topical DMBA application.

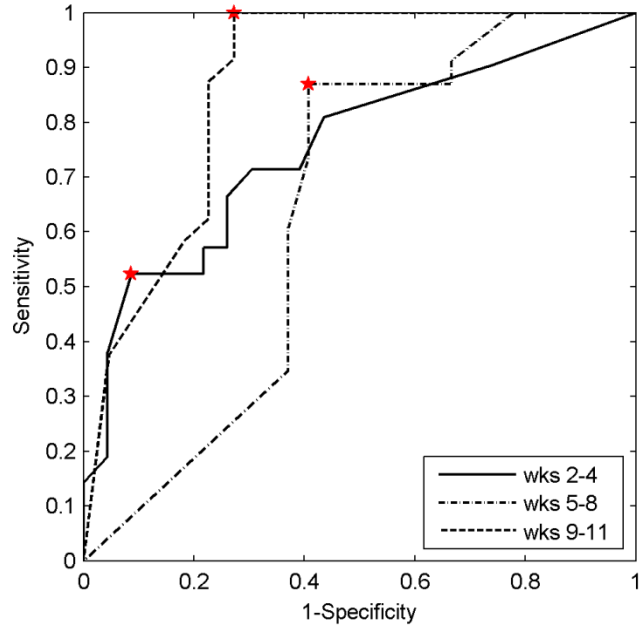


Figure 2-9. ROC curves for the detection of DMBA-induced skin pathology using laser-induced fluorescence. The data set was partitioned into early (weeks 2-4), middle (weeks 5-8), and late (weeks 9-11) time periods of papilloma development resulting from topical DMBA application.

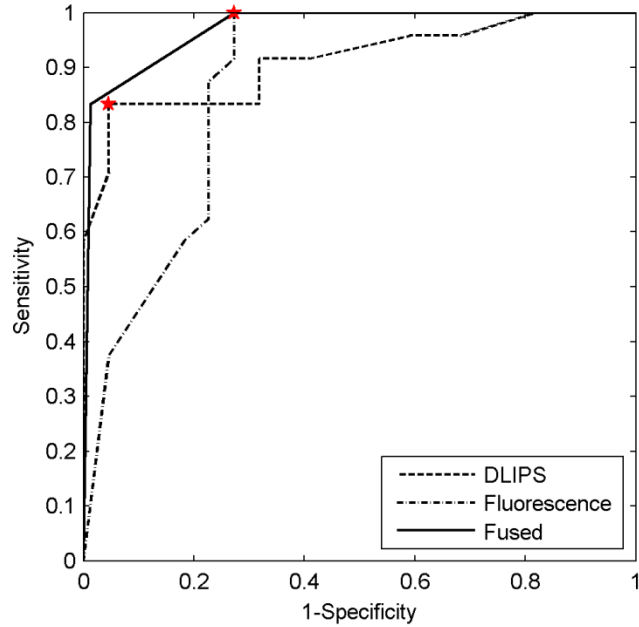


Figure 2-10. ROC curves for the fused decision incorporating both fluorescence and DLIPS spectra to boost the optimal performance in detecting DMBA-induced skin pathology in the “late” timeframe, weeks nine to eleven. The other ROC curves are from the DLIPS and fluorescence based techniques alone, with the selected operating points noted (\*).

## CHAPTER 3

### DLIPS SPECTRA OF ORAL MUCOSA PATHOLOGY: MONTE CARLO MODELING OF SITE-SPECIFIC OPTICAL AND FLUORESCENT PROPERTIES AND THE CHANGES INDUCED BY 193 NM PHOTOCHEMICAL PERTURBATION

#### Motivation

Superficial carcinomas like oral cancer provide an opportunity for technological approaches to earlier screening and diagnosis due to the nature of their development. These carcinomas are invariably preceded by dysplastic precancerous cellular changes, in which histological changes associated with malignancy are often confined to the epithelial layer.<sup>84</sup> Dysplasia, defined as unequivocal neoplastic epithelium, is at present the most reliable biomarker of malignancy. Many of these earliest changes (excellent targets for diagnosis and screening) are not detectable visually, but these molecular changes are often detectable using fluorescence or optical spectroscopy both *in vitro* and *in vivo*.

As a result, there has been an explosion of proposed optical approaches to addressing the problem of oral cancer diagnosis. These technologies have primarily attempted to translate successful *in vitro* techniques directly into tools for evaluating cancer *in vivo*. The oral mucosa specifically, because of the ease of access, has been targeted for a large number of clinical techniques employing tissue autofluorescence imaging or spectroscopy.<sup>41-43</sup> The promise of these strategies however, has been marred by high false positive rates when applied to clinical screening and diagnosis.<sup>45</sup> This is because the preclinical phase of the dysplastic transformation into oral squamous cell carcinoma is varied, often asymptomatic, and easily lumped into two generic oral pathology categories: leukoplakia or erythroplakia.<sup>17, 18</sup> Leukoplakia is describes a white patch of oral mucosa that cannot be removed through gentle contact.

The lack of color is often due to the hyperkeratosis of the superficial epithelium and is responsible for the non-specific “loss of fluorescence” associated with these lesions.<sup>85, 86</sup> Erythroplakia presents with a red, inflamed, velvety surface.<sup>85, 86</sup> These terms are generally terms of exclusion, reserved for when the underlying cause is undetermined. Most often, these lesions are the result of benign inflammation, hyperkeratosis, or ulceration and may persist or self-resolve. And these benign diseases are in fact more prevalent than oral cancer, as up to 15% of the population presents with oral mucosal disease (non-malignant or pre-malignant) at any given time, despite the much lower incidence of oral cancer in the population.<sup>17, 18</sup> These generic characteristics of oral pathology often mask the slow pre-malignant transformations from both the dental professional and currently available diagnostic aids. It has been reported that variations of up to a factor of five have been observed in the endogenous fluorescence signals between patients.<sup>49</sup>

Recently, a new tissue fluorescence probing technique, Differential Laser-Induced Perturbation Spectroscopy (DLIPS), has been proposed to address some of these limiting factors for traditional tissue optical diagnostics as well as open another optical sensing dimension to augment tissue spectroscopy techniques.<sup>38</sup> The DLIPS sensing scheme is based on recent research showing that the biological matrix may be altered by low intensity, sub-ablative deep ultraviolet radiation (193 nm) such that the intrinsic fluorescence response is perturbed.<sup>36, 37</sup> It has been demonstrated that this novel sequential combination of fluorescence probing, UV photochemical perturbation, and repeat fluorescence probing, realizes a powerful new spectral dimension based on difference spectroscopy that is strongly coupled to the local biomolecular matrix.<sup>36, 37</sup>

Because of the intimate coupling of the perturbing laser to the biological matrix, molecular structures of abnormal tissue (e.g. dysplastic precancerous cells) have been shown to respond differently than normal tissue.<sup>38</sup> This technique examines differences in fluorescence response; hence many of the significant variations in the absolute optical response, generally observed in patient-to-patient populations, can be overcome. Preliminary pre-clinical investigation of DLIPS as a diagnostic modality for the detection of pre-malignant lesions has shown promising results, however the physical and biochemical underpinnings of this technique have received no consideration aside from drawing speculative connections between common tissue fluorophores and the diagnostic regions of the DLIPS spectrum.<sup>38</sup>

Understanding the relevance of DLIPS to in vivo diagnostics requires a fundamental understanding of how this spectral dimension responds to the biochemical and morphological changes associated with disease. Further, as the 193nm laser perturbation interacts photochemically with the tissue, a thorough understanding of this phenomenon is essential as well. Monte Carlo methods have previously been applied to the study of light-tissue interactions and in the present study are extended to consider the propagation and photochemical activity of coherent 193nm light as well as the impact of these interactions on the tissue optical and fluorescent properties.

Previous work with Monte Carlo models of multi-layered tissues has shown success in transforming experimental measurements into accurate representations of the underlying optical and fluorescence properties, and these models have been used to understand the hierarchical structure of epithelial tissue in the context of the remitted light signal.<sup>9, 28-30, 87</sup> Further, sensitivity analyses of these models have demonstrated

that the remitted light is extremely sensitive to changes in the optical properties and morphology of the target tissue.<sup>29</sup> In the case of DLIPS-based tissue measurements, these changes in optical properties are not just due to pathological changes but molecular changes induced by the perturbation laser.<sup>34, 36-38</sup> Here we demonstrate that by using model-based approaches, the diagnostic potential of DLIPS can be ascribed to specific biochemical changes of both disease and photochemical perturbation.

The purpose of this study was to develop a model of the DLIPS-tissue interactions, within the context of the ultimate sensing modality, fluorescence spectroscopy. Because of the high degree of variability in the fluorescent properties of the individual layers of buccal epithelium, as well as the limited penetration depth and photochemical potential of 193 nm light, this was built around multi-layered epithelial tissue model as described previously.<sup>9, 29</sup> The optical properties and gross morphologies of these tissue simulations were varied to describe healthy, benign, and dysplastic oral mucosa. The model was populated with tissue optical properties from measurements of these properties reported in the literature.<sup>9, 28-31, 33, 34, 87</sup> Using this model, we were able to draw connections between the remitted fluorescence from tissue and the contributions of individual tissue layers and fluorophores to that signal, in addition to showing how excimer perturbation affects this signal.

As supporting evidence, we present outputs of Monte Carlo simulations before and after photochemical perturbation as well as for models of healthy oral tissue, dysplastic (pre-malignant) oral tissue, and benign oral pathology. Specifically, we examine changes total remitted fluorescence as well as from individual tissue layer of the oral mucosa. Further we examine the computationally modeled DLIPS spectra and consider

the origins of this spectral signature in the tissue using the remitted fluorescence spectra. Finally, we compare these spectra to measurements made in vivo.<sup>38</sup> In presenting these outputs from the Monte Carlo model, this study confirms previous empirical observations that using laser perturbation with difference spectroscopy does change the direct coupling of the returned spectral signature to the target tissue. While further validation will need to be performed for this technique using excised tissue layers, this work presents a mechanistic framework for understanding the complex spectral signatures generated by this technique; a crucial component of understanding the future impact of this technique as a clinical detection modality.

## **Materials & Methods**

### **Simulation Workflow**

As the goals for this simulation exceed that obtainable through a traditional Monte Carlo modeling approaching to light propagation in tissue, Monte Carlo methods were embedded within the overall simulation scheme (Figure 3-1). In a simple approach to modeling a DLIPS measurement, one envision the linear experimental workflow (fluorescence measurement, perturbation, second fluorescence measurement) as being modeled as sequential Monte Carlo simulations of the fluorescence measurement, excimer laser perturbation, and a final fluorescence measurement. In addition however, this workflow takes into consideration the photochemical interplay between excimer laser perturbation and tissue optical properties, tradeoffs between modeling 193 nm light using Monte Carlo simulations and the Beer-Lambert Law, the layer-dependence of tissue optical and fluorescence properties, and the changes in optical properties due to disease. The global analysis centers around the information embedded in the remitted

light; how both disease and photochemical perturbation (separately and jointly) influence that collected spectrum.

### **Monte Carlo Model Construction**

A basic Monte Carlo framework for simulating light propagation in tissue was constructed in MATLAB<sup>®</sup> (The Mathworks, Natick MA) for the purpose of this study, based upon previously developed models.<sup>21</sup> The rationale for developing the modeling software in-house was to have the flexibility to model photochemical and fluorescent interactions, as well as the impact of the former effect on the tissue optical properties within the model. The source was modeled either as a tophat beam profile from free laser beams or from direct contact of a fiber-optic bundle with the tissue, again with a tophat beam profile. Each beam profile was modeled with a diameter of 1 mm. The free beam was assumed to have no divergence at the point of tissue irradiation while the photons emitted from the fiber were emitted at an angle of up to 12°, the maximum emission angle calculated from the numerical aperture of the fiber. Additionally, the refractive index of the window for the fiber probe was considered at the boundary between the probe and tissue.

The basic functionality of the model was validated by comparing the diffuse reflectance from this model versus a free, peer-reviewed Monte Carlo model.<sup>88</sup> The two models were compared under identical conditions for two sets of tissue optical properties. Each simulation was run five times using 50,000 photon packets. The results for these simulations were tested for equivalence using a modified t-test in the two one-sided tests (TOST) framework and using Bland-Altman analysis, with a difference of up to 5% in the total remitted light accepted as equivalent.

## Multi-Layer Tissue Model

The buccal oral mucosa was modeled as a five distinct tissue layers, based off of histological and anatomical data as well as previous epithelial tissue optics models.<sup>9, 29</sup> The layers were defined as shown in Figure 3-2, with the thickness of each layer used as reported in the literature.<sup>9</sup> There were three defined layers of epithelium above the basement membrane, as well two distinct layers of lamina propria below the membrane. The fluorescent properties of each layer were modeled by using the dominant fluorophore in that tissue layer as discovered using confocal microscopy and in vitro immunohistochemical techniques, and as used in other tissue Monte Carlo models to study fluorescence alone.<sup>9, 29</sup> The major fluorophores used here were keratin, FAD, NADH, and collagen. The shape of the emitted light spectrum for each of these fluorophores was found in the literature.<sup>29, 89, 90</sup> Quantum yields for each of the five layers of tissue were adapted from a model of the optical properties of skin.<sup>91</sup> While skin is analogous to oral mucosa in its general structure, it varies greatly in the absorption and scattering properties in the superficial layers due to different cellular structures and the presence of melanin at much higher concentrations.<sup>23</sup> Despite this, the dominant fluorophores are generally considered to be consistent on a layer-by-layer basis between epithelial tissues.<sup>90, 92</sup> Variability in the fluorescence in different types of tissue is accounted for by the relative fluorescence; the product of the quantum yield (a fixed property), the fluorophore extinction coefficient (a fixed property), and the fluorophore concentration (variable for different tissue models). The anisotropy and refractive index for each layer were considered to be wavelength-independent and used as described previously.<sup>9, 23, 91</sup> A summary of these properties is given in Figure 3-2.

Models of the spectral properties of absorption coefficients and scattering coefficients of the tissue were built from aggregated, experimentally-collected values from various sources.<sup>9, 28, 30, 93</sup> The spectral response for scattering was developed as a linear combination of Mie scattering and Rayleigh scattering for the UV-Vis range (Equation 3-1) and extrapolated into the deep UV range using a Rayleigh scattering with constant offset model (Equation 3-2). The exponent used for the Mie theory term was adopted from Jacques.<sup>94</sup> In both the Mie and Rayleigh cases, the parameters were lumped together into coefficients in order to facilitate fitting to experimental data (Equations 3-1 and 3-2). The spectral variation in the absorption coefficient was likewise considered and modeled after data collected directly from tissue samples and constituent chromophores.<sup>9, 23, 29, 30, 93</sup> In this case both the exponent and coefficient were fit to the available data using Equation 3-3. The fits to this data are shown in Figure 3-3 and the values for  $\mu_s$  and  $\mu_a$  at 355 nm are given in Figure 3-2. The notable exception is for layer of tissue containing hemoglobin, where the extinction coefficient was used as reported in the literature and the hemoglobin saturation was fixed at 80% with the concentration of hemoglobin in blood assumed to be 150 g/L and Saidi's function for the wavelength dependence of the background tissue absorbance was used.<sup>94</sup>

$$\mu_s(\lambda) = A\lambda^{-0.22} + B\lambda^{-4} \quad (3-1)$$

$$\mu_s(\text{deepUV}) = A\lambda^{-4} + B \quad (3-2)$$

$$\mu_a(\lambda, \text{Epithelium}) = A + Be^{-(\lambda-C)/D} \quad (3-3)$$

## Fluorescent Interactions

In addition to the consideration of absorption and scattering of photons at each step of the Monte Carlo simulation, generation (and consequently propagation of fluorescence light) was treated as follows, developed loosely from.<sup>9, 29, 91</sup> In this model, the excitation wavelength was fixed at 355 nm, and the range of possible emission wavelengths was from 356 nm to 585 nm. At each interaction site in the tissue, the probability of an excitation photon's weight being converted into fluorescence emission was considered by converting the steps of fluorescence generation into probabilities of each event in the cascade happening and then taking the product to find the relative fluorescence efficiency over the emission range (Equation 3-5). In this equation, the ratio of absorption coefficient to transport coefficient represents the probability that a photon will be absorbed, the critical first step for fluorescence generation. The  $\Phi_{ex}$ , or quantum yield represents the ratio of absorbed photons that generate fluorescence from a single fluorophore. The relative layer fluorescence, RF (Equation 3-4), is an experimentally-derived combination of absorbance and quantum yield for each tissue model and layer described in Figure 3-2.<sup>29</sup>

$$RF = \mu_a \phi_{ex} \quad (3-4)$$

This combined parameter was estimated previously using confocal fluorescence microscopy.<sup>9</sup> The shape of the emission spectrum,  $P(em|\lambda)$ , was modeled after experimental data collected from excised tissue layers as well as from solutions of the relevant constituent fluorophores.<sup>9, 23, 87, 90, 92, 93</sup> This data was fit to a Weibull function (Equation 3-6) using a non-linear solver in MATLAB<sup>®</sup>. When fluorescent photons were generated, no additional photon weight was deposited in the tissue and all of the weight

of the excitation photon was transferred to the emitted photon. Figure 3-3 shows the fluorescence efficiency, calculated from the quantum yield measured in the given layer of tissue where the fluorophore dominates and the emission spectral shape modeled after measurements made on exogenous fluorophores.<sup>89</sup>

$$F(\lambda_{ex}, \lambda_{em}) = \frac{\mu_a}{\mu_a + \mu_s} \mu_a \phi_{ex} P(em | \lambda) \quad (3-5)$$

$$P(em | \lambda) = A \left( \frac{\lambda}{B} \right)^{C-1} e^{-\left( \frac{\lambda}{B} \right)^C} \quad (3-6)$$

### Photochemical Interactions

Biochemically, peptide bonds, aromatic amino acids, and nucleic acids all strongly absorb 193 nm. However, it has been shown that in cultured cells, 193 nm light induces far less photochemical DNA damage when compared to middle UV light.<sup>31</sup> This is due to the high absorption coefficients of peptide bonds and aromatic amino acids, both present in high concentrations in the extracellular matrix and the cytosol effectively blocking the light from interaction with the genetic material contained in the nucleus. For the purposes of this model, absorption by protein was the only interaction considered. In the case of 193 nm light, the energy of a single photon 6.4 eV, exceeds that of peptide bonds as well as the aromatic ring structures of characteristically fluorescence amino acids. As the energy exceeds the bond energy in all cases considered, this model assumes that if a photon is absorbed, then the bond breaking reaction will proceed in accordance with the quantum yield for that reaction. The probability of a photon being absorbed in the Monte Carlo model was given as in the fluorescence model, the absorbance fraction versus scattering. Multiplying that by the effective cross-section, the net concentration and the net quantum yield for all peptide dissociation reaction, the

net photodissociation is calculated (Equation 3-7). This is the generic propensity for absorbed light to break some bond in a protein, not specifically a peptide bond. The net photodissociation reaction is related to all of the possible specific bond-breaking mechanisms by the relationship in Equation 3-10, where  $\epsilon$  is the molar extinction coefficient for each type of bond in the protein, and  $\phi$  is the quantum yield for each specific mechanism. In this case since both the quantum yield and extinction coefficients are considerably higher for aromatic amino acids as opposed to aliphatic ones, the contribution from aliphatic amino acids is assumed to be negligible. Using this relationship, the photodissociation reactions can then be grouped into two main types, those that break peptide bonds (Equation 3-8) and those that break aromatic side chains (Equation 3-9).<sup>34</sup>

$$PD_{net} = \frac{\mu_a}{\mu_a + \mu_s} \mu_a \phi_d \quad (3-7)$$

$$PD_{sc} = \frac{\mu_a}{\mu_a + \mu_s} \mu_{a,bond} \phi_{sc} \quad (3-8)$$

$$PD_{aromatic} = \frac{\mu_a}{\mu_a + \mu_s} \mu_{a,aromatic} \phi_{d,aromatic} \quad (3-9)$$

$$\phi_d \epsilon_{net} \approx \phi_{sc} \epsilon_{bond} + \phi_{d,peptide} \epsilon_{peptide,net} \approx \phi_{sc} \epsilon_{bond} + \frac{N_{aromatic}}{N_{peptides}} \phi_{d,aromatic} \epsilon_{aromatic} \quad (3-10)$$

In the most superficial layer of buccal epithelium, keratin is both the dominant fluorophore as well as the dominant protein, and has an estimated peptide bond density of 1 M and an estimated aromatic ring density of approximately 0.065 M.<sup>32</sup> Unlike collagen in which the source of fluorescence is the cross-linking molecules, keratin fluorescence arises primarily from the aromatic amino acids nested into the protein

coiled supra-molecular structure. Therefore it is reasonable to assume that photolysis of the aromatic residue will result in both a loss of fluorescence as well as a decrease in the absorbance cross section at 355 nm. However, if the bond cleaved is a peptide bond, there is no change to the absorbance cross section at 355 nm but there is the potential to disrupt the supra-molecular structure responsible for the unique fluorescence character of keratin. It was assumed in this case that the closer the peptide bond was to an aromatic residue, the higher the likelihood it would disrupt the local structure critical to fluorescence generation. Thus the likelihood of peptide bond cleavage inducing loss of fluorescence was given as the fraction of aromatic amino acids in a typical keratin fiber to the total number of peptide bonds.

Similar treatment was given to deeper tissue layers but due to the limited penetration depth of 193 nm light, these layers were not modeled as no photons propagated into any layer beyond the superficial epithelium and using the Beer-Lambert law, the incident photon energy drops by an order of magnitude approximately every 5  $\mu\text{m}$ .

### **Pathology Models**

Models for benign pathology and dysplastic pathology were modeled by combining histopathology data, confocal microscopy data, optical coherence tomography data, and tissue spectroscopy studies, as well as clinical observations available in the literature.<sup>9, 23, 29, 87, 89, 90, 92, 93, 95</sup> To model our benign pathology, a persistent inflammatory lesion with hyperkeratosis was used as a model of a generic benign leukoplakia. Dysplasia, was modeled by taking into account increased cellular metabolism, loss of cellular differentiation, and a thickening of the superficial epithelial layer among other characteristics as previously described and as shown in Figure 3-2.<sup>9, 96, 97</sup> Further, both

are often characterized by a loss of fluorescence upon UV excitation, which was only addressed by using previously reported experimental measurements of layer fluorescence.<sup>9</sup> Figure 3-2 summarizes the differences from the baseline model for each of the model pathologies as well as the biological justification for the previously-observed changes in the particular optical properties in the “notes” column.

### **Simulation Details**

Masks of the photochemical damage and the resulting modifications to the local absorption and fluorescence properties of the tissue were created by running simulations of the ArF laser perturbation five times using  $10^6$  photons for each trial and then averaging the results. Simulations of pre- and post-perturbation tissue fluorescence for each of the tissue models described were performed with  $10^6$  photon packets each.

## **Results**

### **Model Validation**

For both sets of tissue parameters tested in the Monte Carlo system presented here versus a previously-validated model, the null hypothesis (ie: that the data sets are from different distributions) was rejected with a  $p < 0.01$  using the TOST methodology and accepting a up to 5% difference between the model outputs as equivalent. Figure 3-4 shows the Bland-Altman plots for the two Monte Carlo frameworks, with the bias and limits of agreement noted for each set of model parameters.

### **Pre-Perturbation Fluorescence**

Figure 3-5 (A-C) shows the fluence, in logarithmic units, of photons through each of the three tissue models: healthy cheek, dysplastic oral mucosa, and a benign buccal lesion respectively. Comparison between these three plots demonstrates that even

subtle changes to the tissue can greatly influence how and where the light interacts with tissue. What is not apparent here is how these properties influence the generation and propagation of fluorescence light specifically. Despite the tissue depth in the figure cutting off at 1,600  $\mu\text{m}$ , the simulation actually ran using a depth of over 10,000  $\mu\text{m}$ , long enough to consider the deep stroma an infinite medium for this model.

Figure 3-6 however, considers this full depth of tissue for each of the models. This figure shows the fraction of the light absorbed by each layer as compared to the fluorescence generated in that tissue layer, and also shows the fractional efficiency of fluorescence generation for each layer. More important however is the light that is actually remitted from the tissue, shown in (d-f) for the healthy cheek, benign leukoplakia, and a dysplastic lesion respectively. Again there are obvious differences between the models, particularly in the loss of total fluorescence observed for the pathological states. It is interesting to note however that despite losing fluorescence intensity in these two cases, the layer-by-layer breakdown indicates different reasons for this observation. Also of note is the small signals from the superficial epithelium and the intermediate epithelium for healthy tissue and the marked increase in fluorescence signal from these layers for either benign or dysplastic pathology models. Additionally, there is considerable fluorescence information lost from the collagen network of the stroma, likely due to the high absorbance of the stromal layer as well as the tissue depth through which that emitted light must travel in order to reach the surface of the oral mucosa.

### **Excimer Laser Perturbation Patterns**

Figure 3-7 shows the fluence of 193 nm light through the superficial epithelium. In the deep UV range the absorbance properties of tissue dominate the scattering

properties, explaining the high degree of preservation of the collimated beam profile and the extremely low penetration depth. Figure 3-8 shows the fractions of photons converted into different bond breaking reactions in the tissue. The slightly elevated levels of loss of fluorescence reactions over aromatic amino acid interactions is explained by the fact that the model takes into account some local-area influence of peptide bond cleavage on the fluorescent properties of keratin. The slight drop in the middle of the fluence pattern is an artifact of the Monte Carlo method; it is often hard to pass photons through the small volume of voxels on the axis of radial symmetry. This effect is particularly prominent when absorbance dominates scattering, as is the case for 193 nm light (the opposite effect is in fact observed when scattering dominates absorbance).<sup>21</sup>

### **Post-Perturbation Fluorescence**

Post-perturbation patterns of fluorescence, as assessed using fluence patterns and remitted light signatures, looked similar to pre-perturbation patterns, as expected from previous experimental studies of DLIPS.<sup>38</sup>

### **Computed Spectral Remittance and Layer-Specific Signals**

Figure 3-9 shows sources of contrast in the DLIPS spectrum on a per-layer basis for healthy tissue, pre-malignant lesions, and benign lesions. Interestingly, despite modeling hyperkeratosis in the superficial epithelium for both benign and pre-malignant disease, the DLIPS signal from this layer is much weaker when compared to healthy oral mucosa. Additionally, despite the small fluorescence footprint of FAD when excited at 355 nm, the DLIPS spectral characteristics integrate significantly different levels of signal from the intermediate epithelium for the different oral mucosa states considered here. Although there is some change observed in the DLIPS signals from basal

epithelium and the stroma, it is relatively small which is not surprising given the depth of these layers in the tissue when compared to the penetration depth of 193 nm light.

In contrast to the changes observed in for the DLIPS spectrum as a function of tissue layer and pathology, Figure 3-10 shows the signal contributions from each tissue layer for fluorescence alone. Based upon the large degree of experimental work in fluorescence tissue spectroscopy assigning epithelial fluorescence at 355 nm primarily to collagen, it is not surprising to find that the most prominent feature (in terms of signal strength) is from the stroma.<sup>87, 92, 95</sup> Surprising however, is the convergence in terms of stromal signal strength, approximately equal for both pathologies, despite the fact that the models vary in the particulars of changing the optical properties of the stromal layer and the more superficial layers. Also of note are the extremely low fluorescence signals from the superficial and epithelial layers, essentially biasing the returned information towards the basal epithelium and stromal layers exclusively. Figure 3-11 shows computed fluorescence spectra from each of the three oral tissue types. Similar to previously-reported experimental data, all of the spectra are dominated by a combination of collagen and NADH fluorescence, obscuring the weaker signals from keratin and FAD.<sup>87, 90, 92, 95</sup> Further validating this model are the observations of a loss-of-fluorescence for both the leukoplakia model and the dysplasia model, again characteristic of experimental observations.<sup>3, 9, 17, 20</sup> Finally, a shift of the signal peak is observed as the dominant fluorophore shifts from collagen in healthy oral mucosa to NADH in the dysplastic tissue.

Figure 3-12 shows a computed DLIPS spectrum from healthy oral mucosa, pre-malignant, and benign pathologies. Due to the low amount of DLIPS signal recovered in

this model, the spectral resolution is limited to bins of 20 nm in size. In a similar way to what is observed experimentally, because of the high degree of sensitivity to changes between measurements across the DLIPS spectrum, it is challenging to visually inspect the spectra and assign features to changes in the tissue optical and fluorescent properties. Previously, decomposition using principal component analysis has been shown to provide some insight into the origins of contrast implicit in the DLIPS signatures of contrast in epithelial pathologies, but these relationships did not consider a model of the fluorescent properties of tissue, only the most likely explanations for the remitted spectral signatures. While in the fluorescence spectra it is not possible to ascribe spectral regions to each tissue layer or particular fluorophore, Figure 3-12 demonstrates this is possible for DLIPS and further that there are unique changes for the pathology models, not just the arbitrary loss-of-fluorescence observed in traditional tissue fluorescence spectra (Figure 3-11). In shorter wavelength range of the DLIPS spectrum, the dominant tissue feature should be keratin, and there are dramatic changes in the DLIPS signal for this range between the healthy tissue model and either of the pathology models. This is both because of the specificity of interaction of the perturbing excimer laser with this layer as well as the dramatic changes in fluorescent and morphological properties associated with either the dysplastic transformation or persistent inflammatory lesions. At the long end of the DLIPS spectrum there are also pronounced changes that can be ascribed to changes in accessibility to FAD fluorescence information in the intermediate epithelial layer due to the optical clearing effect on the superficial epithelium of the perturbing excimer laser.

## Discussion

In this paper we presented a Monte Carlo modeling approach to studying a new tissue fluorescence spectroscopy technique, DLIPS. The model was based upon previous clinical, histopathological and optical spectroscopy studies of both healthy and diseased tissue. By using disease-modeling approaches previously used to study tissue fluorescence, instead of developing the modeling uniquely for studying DLIPS, this approach minimizes the risk of confirmation bias in support of previously proposed mechanisms and advantages hypothesized for the diagnostic potential of DLIPS. The Monte Carlo model presented here was motivated by a need to explore three fundamental phenomena related to DLIPS tissue spectroscopy. First we explored the supposed biochemical changes induced by 193 nm laser perturbations and the impact on the remitted fluorescence signal. Second we connected in vivo observations of previous DLIPS studies with biological changes associated with both diseased and healthy tissue, noting the biochemical differences and the changes in the associated DLIPS spectra. And finally, we assessed what features of pathology DLIPS preferentially enhances as opposed to fluorescence spectroscopy alone.

As with any model, this represents an imperfect approximation of the reality of DLIPS and fluorescence tissue spectroscopy. However, as much of the model was developed around actual measured tissue optical properties, with pieces validated in other peer-reviewed studies, it is presumed to at least show relationships within the model. This includes exploring how signals change in different pathological states as well the tissue sources of signal for DLIPS and fluorescence spectroscopy. The notable deviations from actual tissue are catalogued and explained further here. The first is the simplification of each tissue layer to only be represented by a single major fluorophore.

In reality, there is likely some cross over between layers, but in other cases experimental evidence has shown that these fluorescent molecules are not present in a particular tissue layer. In the former case, for any layer that contains actively dividing cells, NADH and FAD are likely to both be present as fluorophores<sup>92</sup>. But in the latter case, IHC stains have shown that there is no extracellular collagen present in the epithelial layer of the oral mucosa above the basement membrane.<sup>29, 98</sup> In other studies addressing this topic, it was found that the fluorescence from individual tissue layers was dominated by a particular fluorophore, although the dominant fluorophore could change as a result of pathology.<sup>92</sup> This effect is modeled in this system and is based upon previously reported findings for oral dysplasia and chronic inflammation.

Another limitation is the approximation of layer boundaries as flat interfaces. In reality these interface can range from small undulation to regions of repeated large invagination between the layers to outright breakdown at the boundary where the interface is not well defined.<sup>92</sup> These effects have previously been modeled for skin Monte Carlo simulation and it was shown that the effect is essentially to increase the scattering of light at the boundaries, reducing the amount of incoming light that penetrates these layers and reducing the amount of remitted light.<sup>99</sup> Since these boundary conditions are likely to change for a given pathological state, this could impact differential signals when using optical parameter estimation as the source of pathological contrast but is unlikely to have a significant effect when fluorescence is used.

The final two important approximations deal with the treatment of 193 nm light for Monte Carlo simulations. Due to the limited number of studies available estimating the

tissue optical properties in this wavelength range, some had to be inferred from a higher wavelength range, like the refractive index. It was assumed to be constant over all wavelengths in this model but that is likely not the case at 193 nm. This could dramatically impact the amount of specular reflection at the surface of the oral mucosa and have a significant impact on the penetration depth and photochemical activity. The final generalization was regarding dynamic updating of the absorption coefficient during the modeling of the excimer perturbation process. Photolysis not only affects fluorescence and absorbance properties of tissue at 355 nm, but also at 193 nm as the cleaved bonds are the source of the high absorbance cross-section for this wavelength. Figure 3-7 shows this effect is not trivial and in fact saturation of the bond-breaking process is observed in this model for the most superficial tissue when the model is extended to the full photon flux used experimentally, about  $2.4 \times 10^{17}$  photons. This type of process is tough to implement in a Monte Carlo simulation as it propagates only a single photon at a time. It could potentially have a sizable impact on the penetration depth for the observed photochemical changes, although it is unclear what the implications would be for the DLIPS signal.

Despite these limitations, this work represents a step forward for tissue optics modeling using Monte Carlo methods due to the incorporation of photolytic effects and further this framework can serve as a virtual testbed for optimizing the DLIPS measurement configuration to recover more DLIPS signal or explore how to access more information in the tissue using DLIPS. The latter is considered through the remaining discussion of results.

In Figure 3-6, the remitted fluorescence is considered with respect to the fluorescence generated in that layer and the amount of photons absorbed. Not surprisingly, stromal absorbance is the dominant effect in terms of photons deposited because this is the first tissue layer where hemoglobin is present. This effect is magnified in the pathological case because of the increase vessel density due to local angiogenesis as the emerging neoplasm establishes a hospitable environment for growth. In terms of fluorescence however, emission from NADH tends to provide a nearly equal amount of fluorescence, with the relative levels varying widely between the disease states. From this it is also clear that any changes associated with superficial and intermediate epithelial layers are overshadowed by the signals from collagen and NADH. There is however potentially valuable information about the pathological state contained in these layers that needs to be assayed using a different technique, like DLIPS. Based upon this fact that the relative levels of NADH and collagen fluorescence remittance change so dramatically between the three states of oral tissue modeled here, this would seem to be an appropriate biomarker for detecting pathology. This is problematic at an excitation wavelength of 355 nm, as the spectral overlap makes decomposition of the two signatures hard.<sup>87</sup>

Although the DLIPS technique is supposed to remove inter-subject sources of variability, it is extremely sensitive to measurement noise, due to the differential nature of the signal while keep the same noise level associated with the individual fluorescence measurements. As a consequence, both the experimentally-collected spectra and those derived from this model show a large noise level relative to the size of the signal level. It is likely this can be corrected experimentally by making repeat pre- and post-

perturbation measurements and averaging those to reduce the noise level somewhat. By looking at the relative stability of the per-layer DLIPS signals over repeated measurements, this confirms that by collecting more DLIPS measurements, a more stable measurement can be made. The other possible approach is to increase the amount of perturbation realized between fluorescence measurements, presumably increasing the differential signal.

In Figures 3-9, 3-10, 3-11, and 3-12 the sources of contrast between the healthy cheek and the two model pathologies are explored. This is the most important information recovered from the model because it allows for the formulation of a biological theory supporting any detection contrast observed between these states experimentally and also can suggest if the information contained in the fluorescence spectrum is redundant with the DLIPS information or if they are unique and complimentary. In Figure 3-9, the largest signals are derived from the top two epithelial layers for DLIPS, which is in opposition to the fluorescence levels in Figure 3-10 which heavily emphasize basal layer and stromal fluorescence. This may be an important source of contrast inherent to the DLIPS technique because research has shown that quantitative measurements of keratin fluorescence and density from histopathology can provide early diagnostic biomarkers; despite often presenting clinically in both benign and dysplastic disease as hyperkeratosis, confounding a clinician's ability to diagnose in vivo. When considering the difference in signals between the healthy and pathological states, this fluorescence contrast for detection clearly favor the basal layer (NADH) as the changes to collagen are approximately the same (Figure 3-11). This figure further confirms that the FAD and keratin signals are essentially washed out as noise for

fluorescence spectroscopy, but when considering the DLIPS spectra in Figure 3-12, all of the epithelial layers provide contrast, while the stromal layer does not show much difference from healthy tissue, or a clear differentiator between benign and dysplastic pathology. This is somewhat surprising for fluorescence spectroscopy as one of the earliest pre-neoplastic changes is collagen remodeling near the basement membrane.<sup>75</sup> This could however also occur in benign chronic inflammation as immune cells invade the upper stroma and basal layer of the epithelium. Biomolecular changes of collagen were not considered here but there is evidence to support the presence of at least three unique types of collagen found in the epithelial stroma based upon fluorescence emission.<sup>10, 25, 28</sup> The relative levels of these three collagen structures could provide the contrast between different pathologies for fluorescence as well as provide a unique signature in the DLIPS spectrum. What was unexpected in the DLIPS signature was the contribution due to FAD fluorescence, particularly since the emission is so weak at 355 nm excitation.<sup>29, 89</sup> Since the DLIPS is a differential technique, small signals are accessible assuming they are not completely buried in noise. In this case FAD can be an important marker of cellular metabolism, particularly as cells undergo the dysplastic transformation and leveraging this as a source of contrast directly couples the DLIPS spectrum to a cellular process underlying pathological changes.

Accurate modeling of tissue spectroscopy is a complicated undertaking, but can be simplified by using iterative methods and only considering the most important tissue factors impacting it. Adding to that the layers of complexity inherent in addressing disease and population variability makes it even tougher to extract a working understanding of the biochemical basis of tissue spectroscopy. Using experimental

studies to derive site-specific and disease-specific optical properties mitigates these uncertainties and improves the confidence in associating model details and experimental DLIPS and fluorescence spectroscopy observation with biochemical and morphological changes. Still this work motivates and directs future experimental work to optimize the DLIPS technique for clinical detection as well as how to further explore the fundamental mechanisms which support using this technique to differentiate dysplastic pathology.

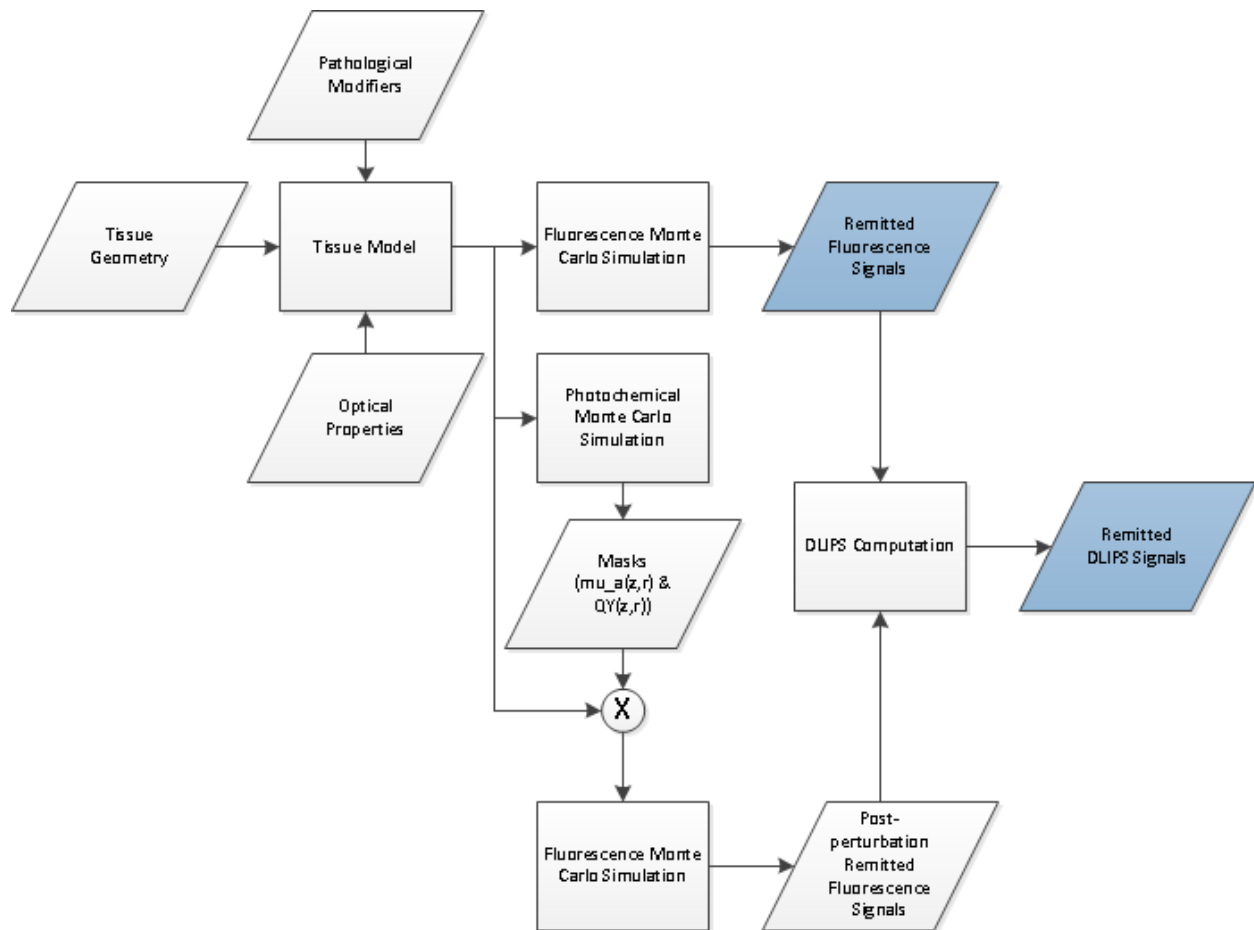


Figure 3-1. Simulation workflow for modeling DLIPS fluorescence tissue spectroscopy. Blue indicates model outputs used to relate remitted light signal characteristics with aspects of pathology or the DLIPS collection scheme

Healthy Oral Mucosa										
Oral Mucosa Layer	Thickness (um)	Dominant Fluorophore	Layer QY	Relative layer fluorescence	$\mu_s(355 \text{ nm}), (\text{cm}^{-1})$	anisotropy, g	refractive index, n	$\mu_a(355 \text{ nm}), (\text{cm}^{-1})$	Blood Vol (%)	
Superficial Epithelium	80	Keratin	0.01	0.12	206	0.97	1.5	3.9		
Intermediate Epithelium	80	FAD	0.01	0.088	62	0.97	1.34	3.9		
Basal Epithelium	120	NADH	0.7	0.74	57	0.97	1.38	3.9		
Upper Lamina Propria	125	Collagen	0.15	0.88	321	0.88	1.4	7.9		
Deep Lamina Propria	1.00E+04	Collagen	0.15	0.9	321	0.88	1.42	9	0.2	
Benign Oral Pathology										
Oral Mucosa Layer	Thickness (um)	Dominant Fluorophore	Layer QY	Relative layer fluorescence	$\mu_s(355 \text{ nm}), (\text{cm}^{-1})$	anisotropy, g	refractive index, n	$\mu_a(355 \text{ nm}), (\text{cm}^{-1})$	Blood Vol (%)	Corresponding features
Superficial Epithelium	160	Keratin	0.01	0.12	206	0.97	1.5	3.9		Hyperkeratosis, invasion by immune cells, shifting of cellular metabolism, hyperplasia
Intermediate Epithelium	96	FAD	0.01	0.068	62	0.97	1.34	3.9		
Basal Epithelium	92	NADH	0.7	0.15	57	0.97	1.38	3.9		
Upper Lamina Propria	125	NADH	0.7	0.15	321	0.88	1.4	7.9		
Deep Lamina Propria	1.00E+04	Collagen	0.15	0.15	321	0.88	1.42	9	0.2	
Oral Dysplasia										
Oral Mucosa Layer	Thickness (um)	Dominant Fluorophore	Layer QY	Relative layer fluorescence	$\mu_s(355 \text{ nm}), (\text{cm}^{-1})$	anisotropy, g	refractive index, n	$\mu_a(355 \text{ nm}), (\text{cm}^{-1})$	Blood Vol (%)	Corresponding features
Superficial Epithelium	222	Keratin	0.01	0.3	206	0.97	1.5	3.9		Hyperkeratosis, shifting of cellular metabolism, invasion of basal cells into upper epithelial layers, hyperplasia, hypervascularization, others...
Intermediate Epithelium	80	FAD	0.01	0.17	62	0.97	1.34	3.9		
Basal Epithelium	256	NADH	0.7	0.8	82	0.97	1.38	3.9		
Upper Lamina Propria	125	Collagen	0.15	0.3	257	0.88	1.4	11.3		
Deep Lamina Propria	1.00E+04	Collagen	0.15	0.7	321	0.88	1.42	11.3	0.6	

Figure 3-2. Tissue optical properties for layer-specific modeling

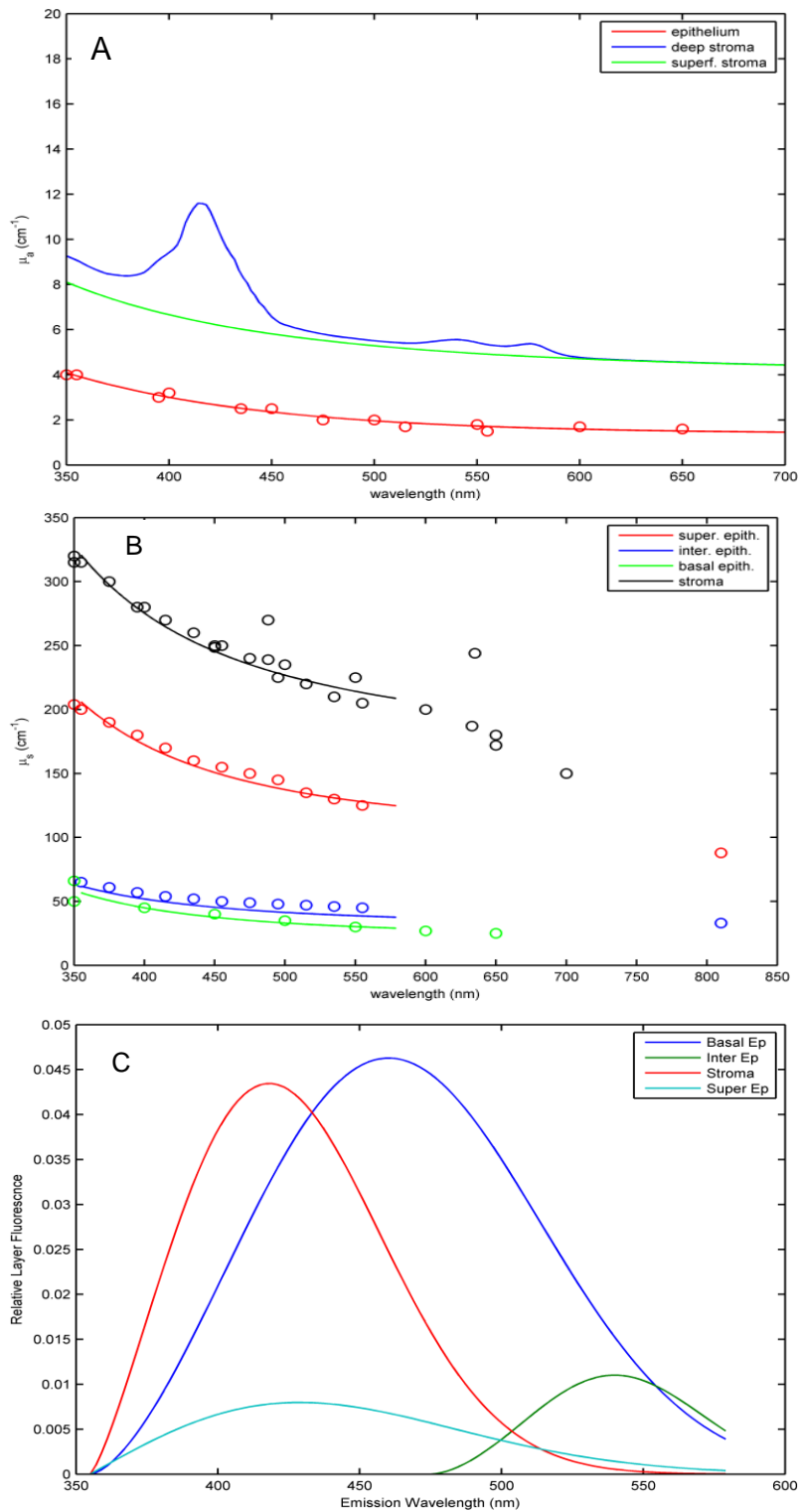


Figure 3-3. Modeled layer-specific optical properties. A) Absorption. B) Scattering. C) Fluorescence. Measurements for fitting the model were found in multiple literature sources as noted in the text

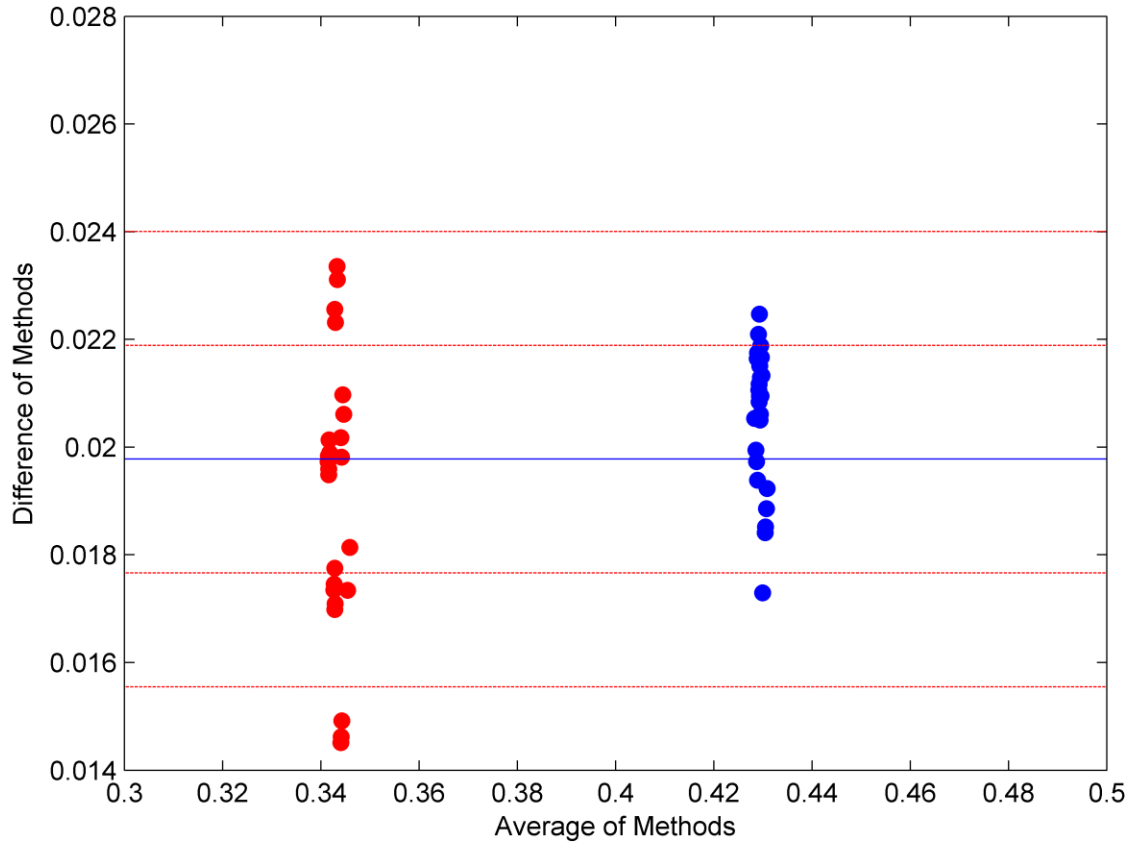


Figure 3-4. Bland Altman plots comparing the total remitted light from the experimental Monte Carlo model versus a previously validated Monte Carlo system. Each system was validated using two sets of model parameters. The blue line represents the bias between the two models and the red lines are one and two standard deviations from the bias value, a measure of the limits of agreement

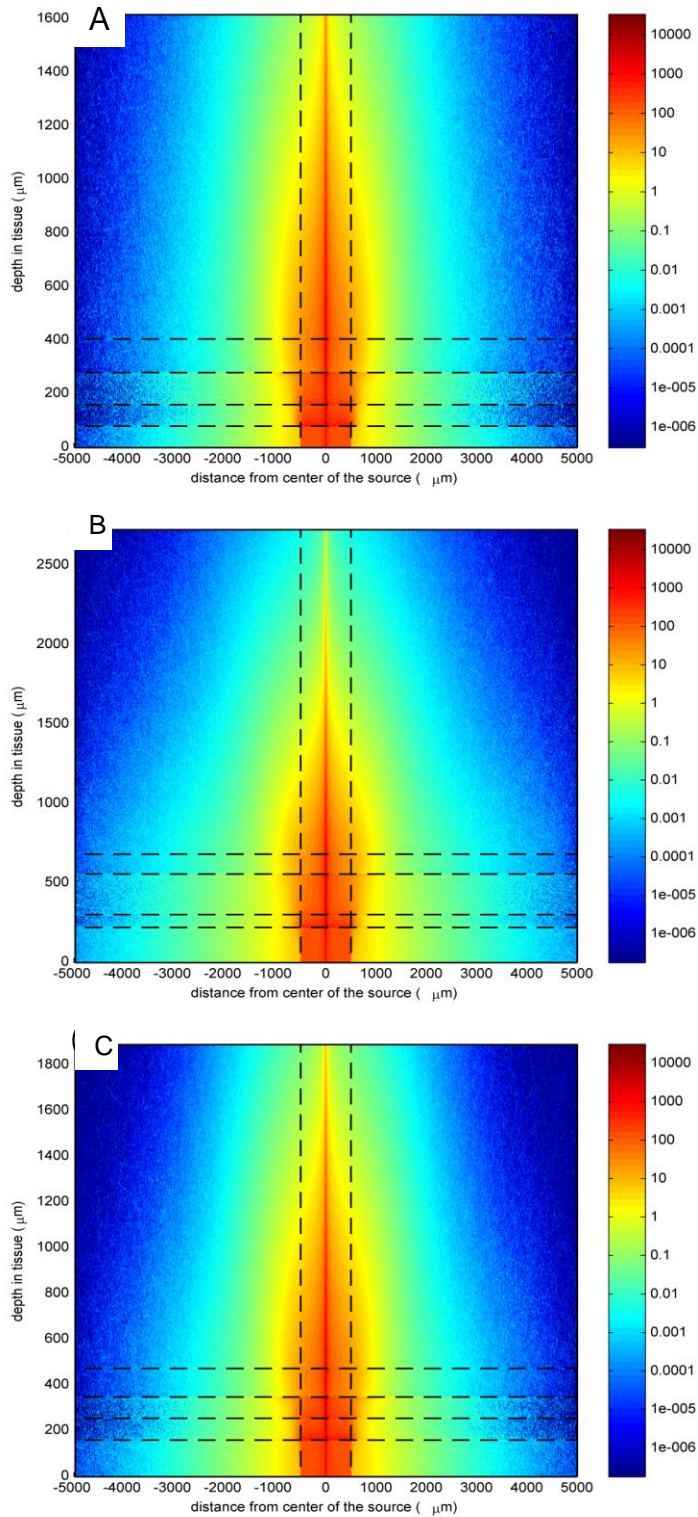


Figure 3-5. Fluence ( $\text{cm}^{-2}$ ), in logarithmic units of photons through the tissue models. A) Healthy buccal tissue. B) Dysplastic oral mucosa. C) Benign oral pathology. Horizontal lines denote boundaries and vertical lines indicate width of the coherent excitation source.

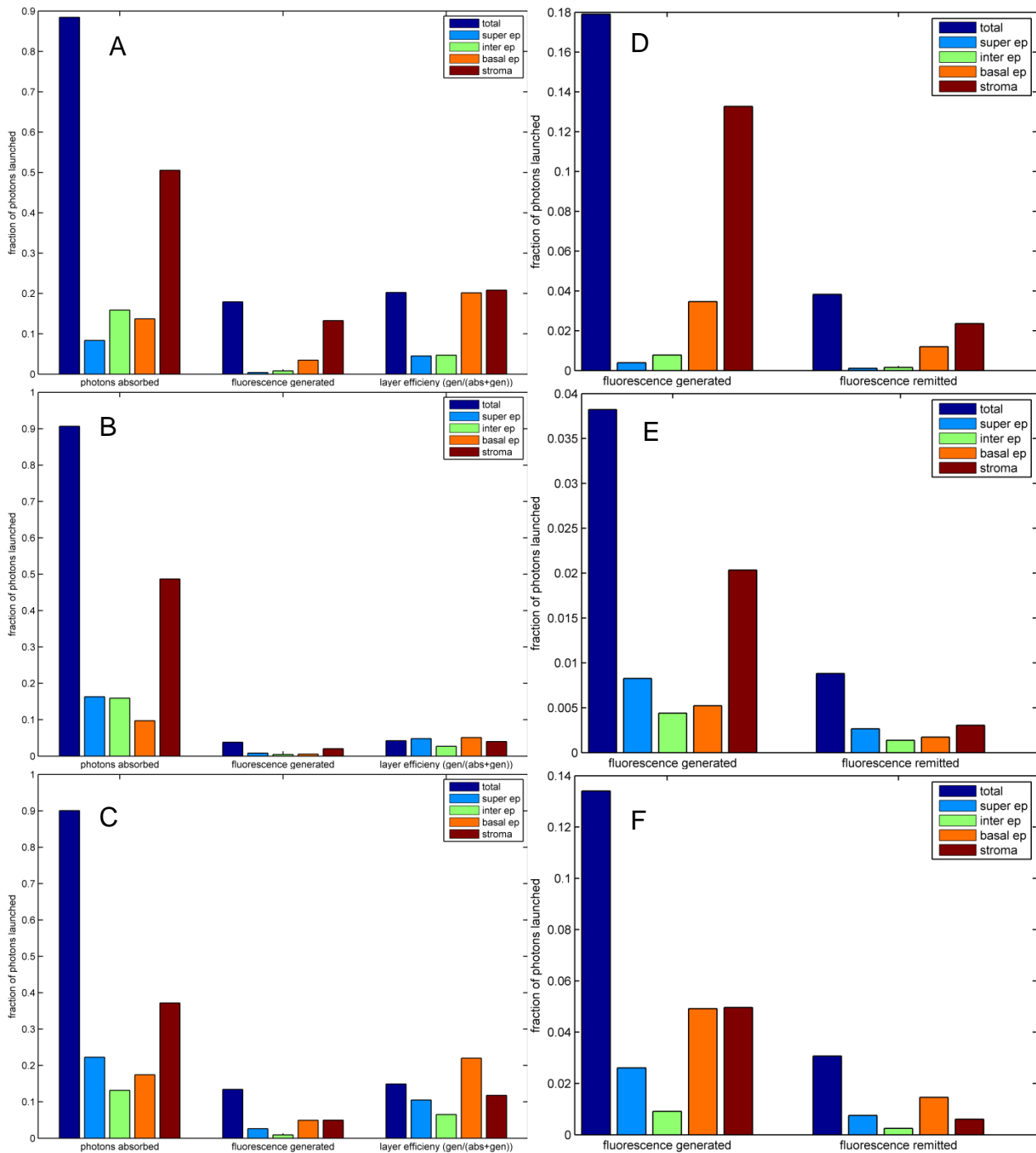


Figure 3-6. Relative per-layer absorption and fluorescence emission. A-C) Absorption of photons, generation of fluorescence, and the layer efficiency for the healthy, benign, and dysplastic oral epithelium models respectively. D-F) Fluorescence generated from each layer as compared to the amount of that light that is remitted from the surface of the tissue to be collected.

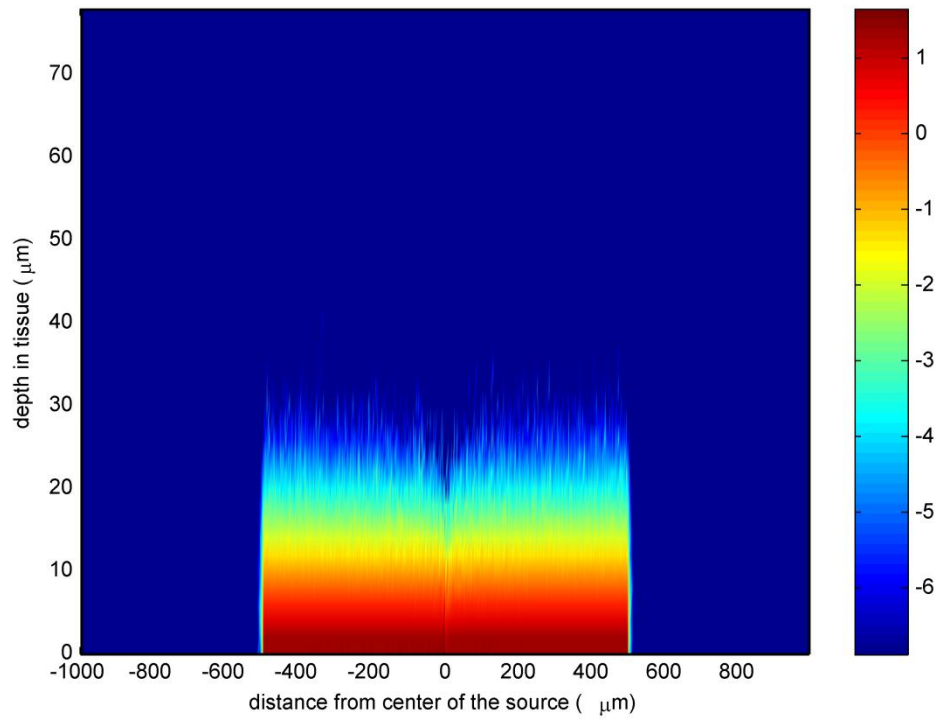


Figure 3-7. Fluence ( $\text{cm}^{-2}$ ) of 193 nm light (logarithmic scale) through the superficial epithelium

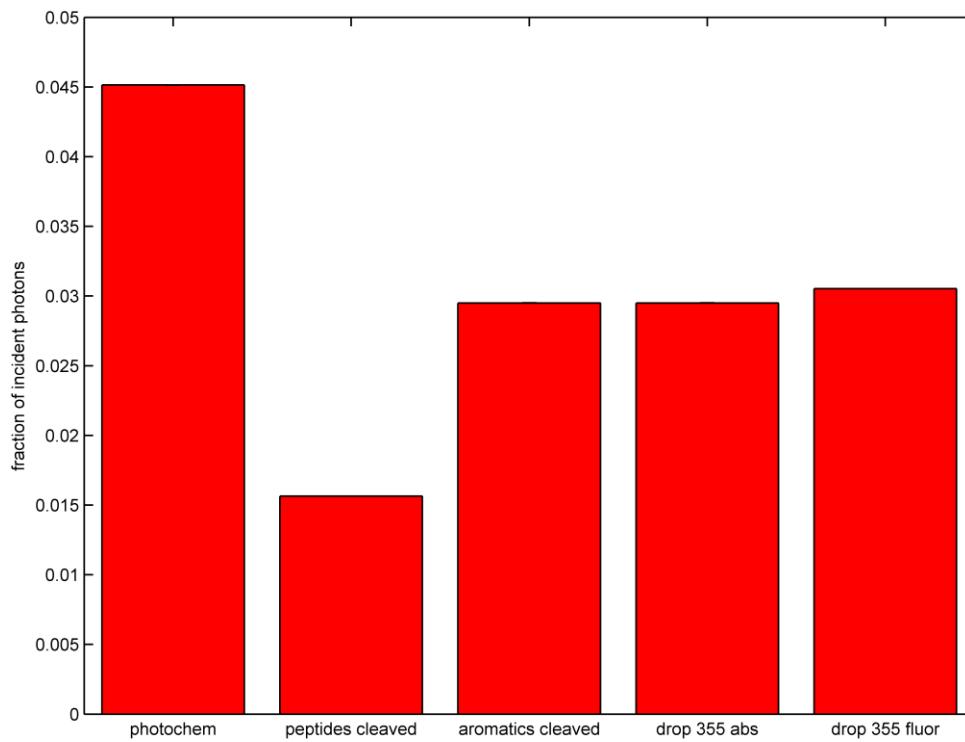


Figure 3-8. Photochemical events stimulated by 193 nm irradiation as a fraction of the total number of incident photons

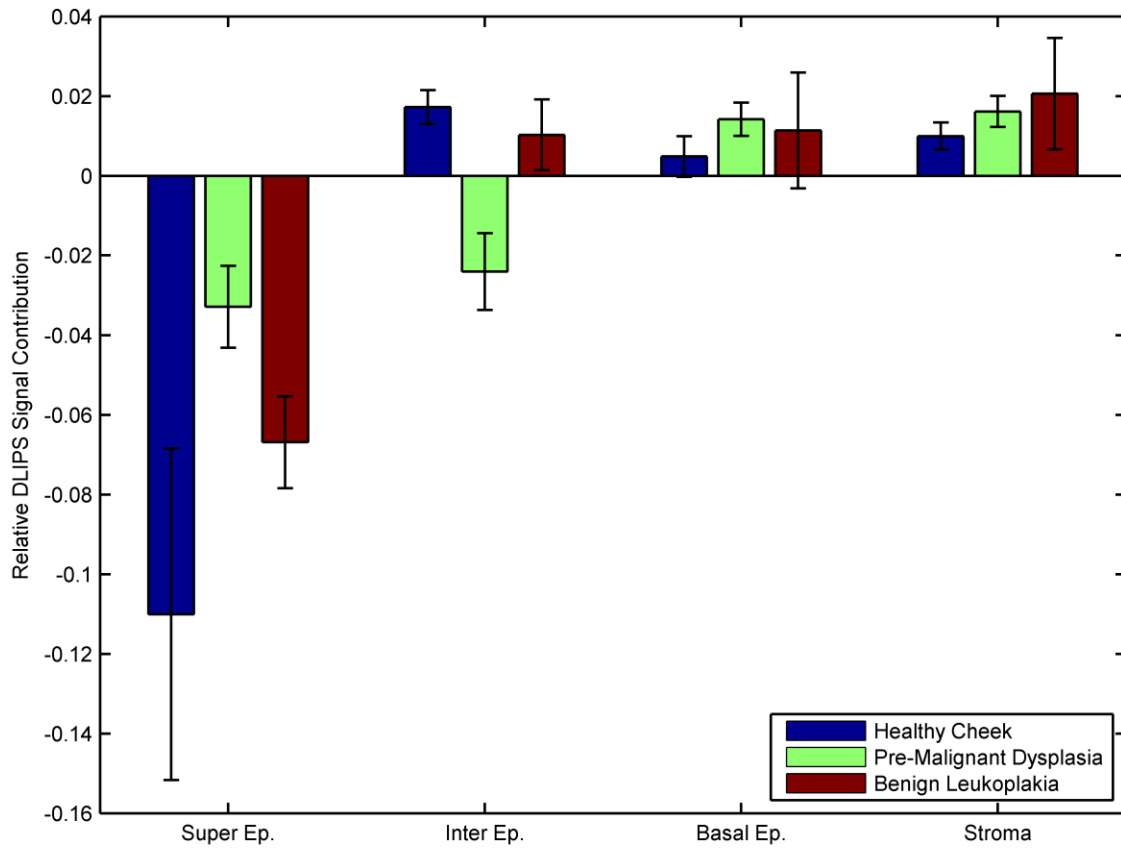


Figure 3-9. Relative contributions to the remitted DLIPS signal from each layer of epithelial tissue

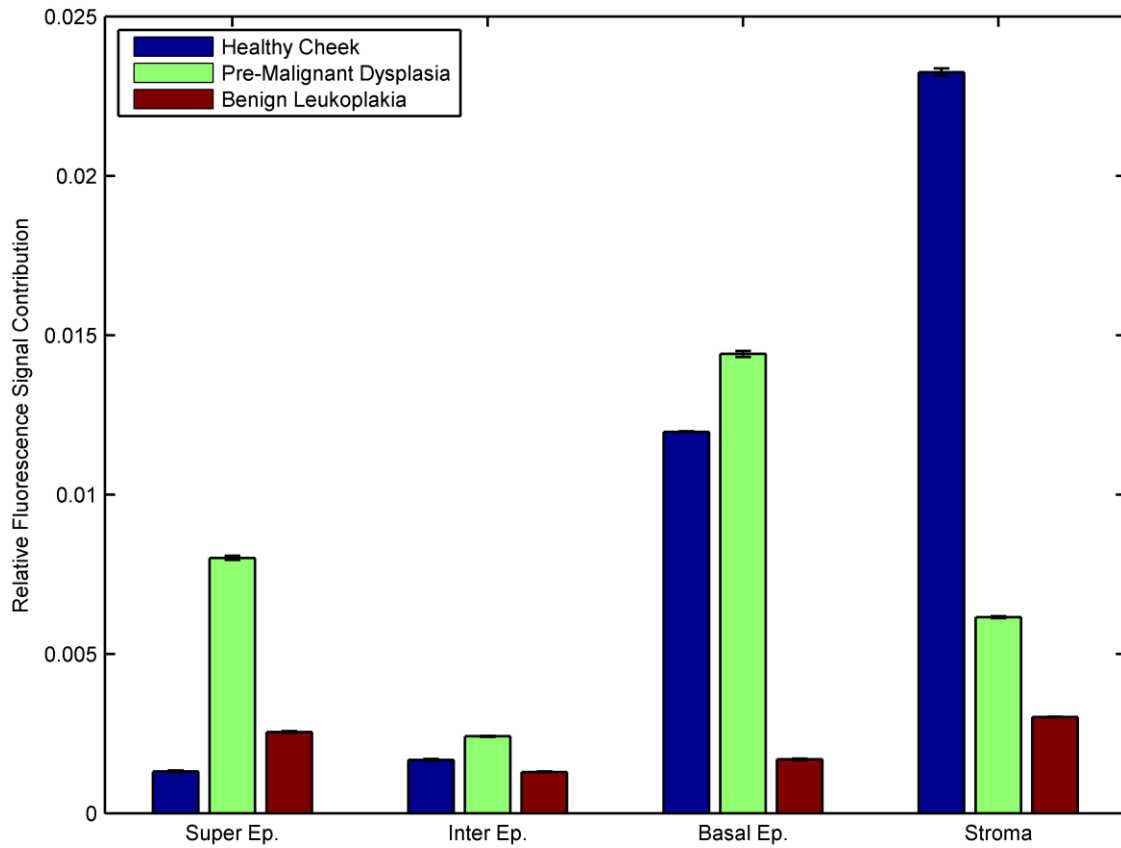


Figure 3-10. Relative contributions to the remitted fluorescence signal from each layer of epithelial tissue

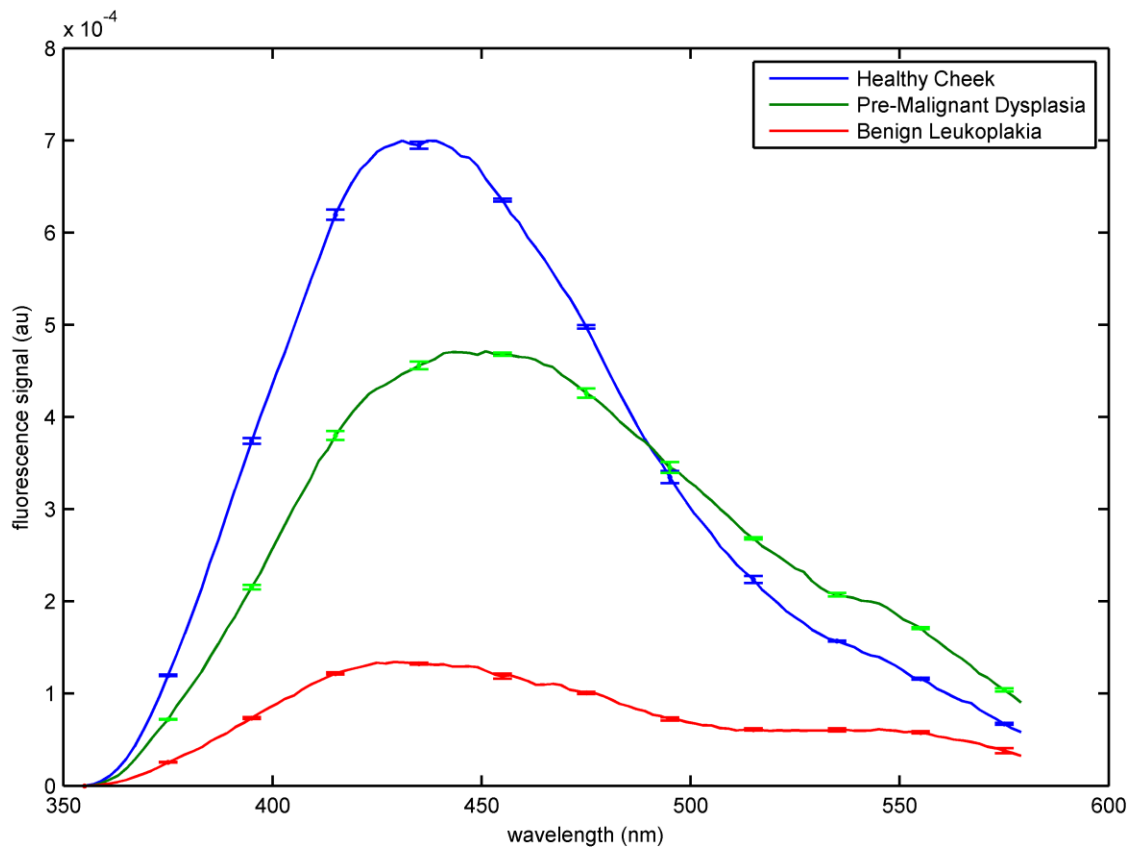


Figure 3-11. Simulated fluorescence spectra for the three tissue models

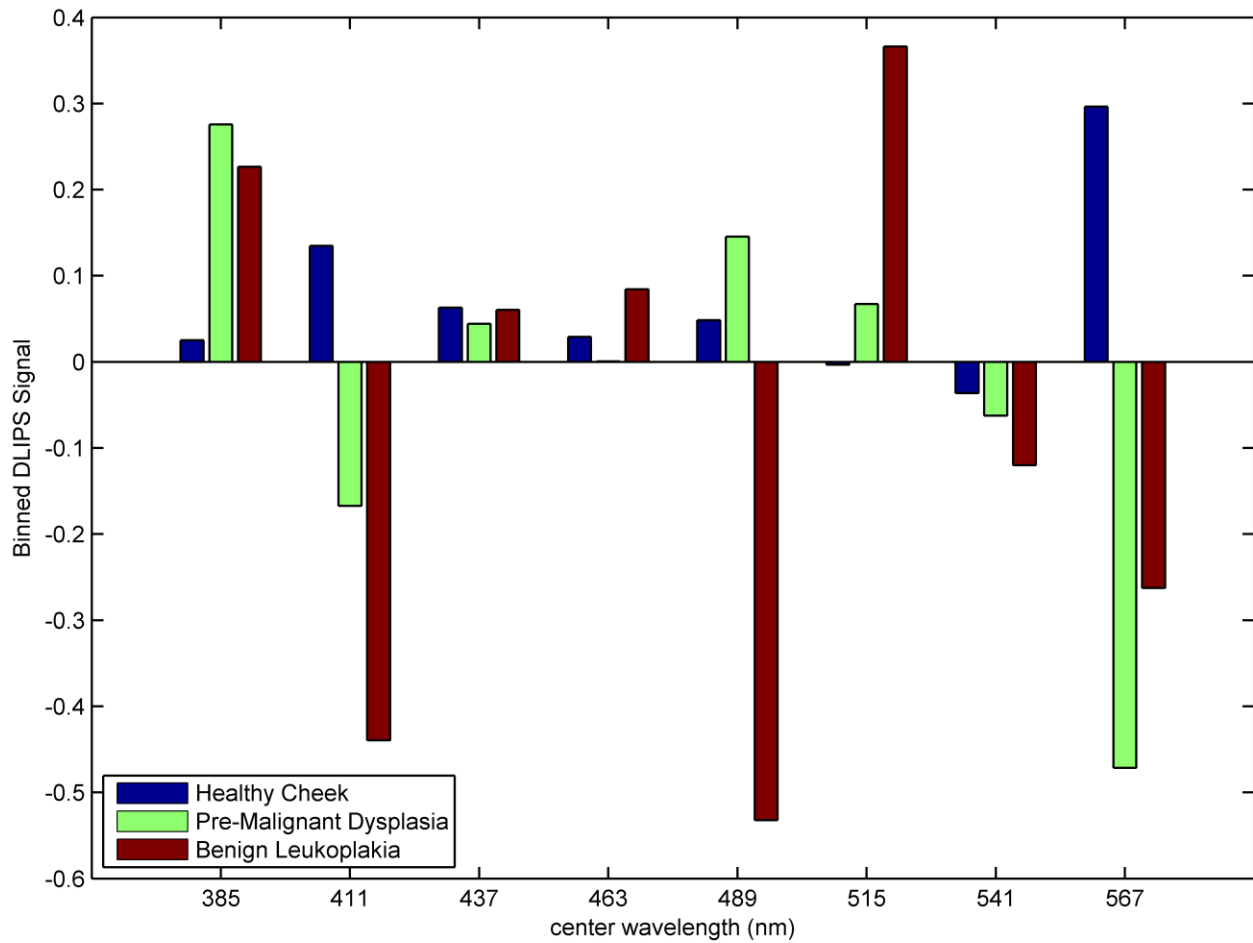


Figure 3-12. Binned spectral DLIPS data from Monte Carlo simulations. Each bin is 26 nm in width and the values represent the summed DLIPS signal over that range (Averaged across three simulations)

## CHAPTER 4 DETECTION THEORY ANALYSIS OF DLIPS-BASED SENSING OF ORAL DYSPLASIA: IMPLICATIONS FOR CLINICAL INSTRUMENT DESIGN AND TESTING

### **Motivation**

Enhanced, early detection of oral pre-malignancies is well-established as a critical component of strategies to improve the 5-year survival rate.<sup>17</sup> Historically, screening patients for oral dysplastic lesions has relied upon a conventional tactile and visual exam, with diagnosis confirmed via biopsy.<sup>3</sup> Over the past 20 years, several adjuvant technologies have emerged to address the problem of better screening for oral dysplasia or benign pathologies.<sup>13</sup> Despite these advances in technology, it has yet to be demonstrated that use of any of these adjuvant techniques results in a meaningful reduction in morbidity and mortality.<sup>13</sup>

The fundamental flaw with these devices is a lack of specificity of the technique for changes associated with cancer progression. Instead these devices are developed and trained to provide contrast for obvious pathological conditions, but are then applied in the clinic to screen for pre-disease state changes.<sup>16</sup> This presupposes that the earlier pre-malignant stages of disease resemble advanced disease. Unfortunately, early pre-cancerous lesions are generally subtle and do not resemble advanced dysplasia or oral malignancies.<sup>3</sup> In addition, pre-malignant lesions are highly heterogeneous in presentation, often mimicking common benign pathologies.<sup>3</sup> There is also a growing body of evidence that indicates many oral pre-malignancies are not detectable to the unaided eye at the earliest stages.<sup>3</sup> New technologies to detection oral dysplasia must consider these issues from the first generation of diagnostic adjuvants, with strategies to specifically assay biomarker of early disease.

Here we present a new biosensing technique Differential Laser-Induced Perturbation Spectroscopy (DLIPS). The technique combines sequential fluorescence probing (pre- and post-perturbation) with sub-ablative, UV photochemical perturbation and difference spectroscopy to provide a new spectral dimension, facilitating two improvements over fluorescence spectroscopy.<sup>36, 37</sup> First, the differential technique eliminates significant variations in absolute fluorescence response within subject populations. Second, UV perturbation directly couples the DLIPS response to the superficial biomolecular structure.<sup>38</sup> Further we develop a pre-clinical animal model framework for testing this device, as well as conventional fluorescence biosensing, which better approximates the observation of both benign, dysplastic, and healthy tissue in the clinic.

The goal of this study was to apply the DLIPS fluorescence technique to specifically detecting an earlier and often ambiguous state of pre-malignant oral lesion development in the presence of benign pathology, a well-known confounding factor in clinical detection. Unfortunately, due to low signal-to-noise levels for the collected DLIPS spectra, it was not possible to conclusively evaluate the performance of this technique in this study. However, despite these negative findings with DLIPS, the structure of the study facilitated critical evaluation of an underlying issue in oral cancer detection: there may be a principled way to design detections systems as well as training and clinical testing to improve diagnostic capabilities.

Because of the disappointing performance of commercially-available devices for detecting oral neoplasia and pre-malignant lesions, and that critical analysis of these devices indicates a lack of testing and optimization prior to reaching the marketplace,

here we present an experimental framework for an optimal detection theory approach to analyzing the detection performance of these devices. Specifically, using the hamster cheek pouch model for dysplastic lesion development as well as benign lesion development and healthy oral mucosa, the ambiguity of the clinical scenario was roughly approximated. Using laser-induced fluorescence (with no pre-defined detection algorithm) as a general surrogate for all fluorescence and light-based technologies in the marketplace, the framework is constructed to evaluate one specific question endemic to all of these devices: If the goal is to find oral cancer and reduce the false positive rate, how can the detection problem be framed to optimize these outcomes? By applying optimal detection theory to several different embedded detection problems and comparing those detectors with currently-available analogs, insight into how detector engineering, algorithm training, and clinical testing may all contribute to improved diagnostic performance at the point of care is provided. This model shows that by re-framing the detection problem in terms of detecting pre-malignant lesion over benign lesions (as opposed to the more commonly used healthy tissue), substantial gains can be realized in terms of enhanced accuracy and anticipated improved clinical performance as this strategy directly addresses the most common confounding source of false positives.

## **Materials & Methods**

### **Chemically-Induced Cheek Pouch Pathology**

Male Golden Syrian hamsters, ten in total were used in this study. Pre-cancerous dysplasia was induced by application of 7,12-dimethylbenz(a)anthracene (DMBA) (Sigma-Aldrich, St. Louis MO) in acetone (Fisher Scientific, Pittsburgh PA) at a concentration of 0.5% w/w to the right cheek pouch of five hamsters. Application was

repeated three times weekly for up to nine weeks. The DMBA-hamster cheek pouch model and the application timeline were selected because of previous work showing that it closely resembles the dysplastic transformation sequence to malignancy observed in the human oral cavity.<sup>96, 97</sup> Particularly, by eight to nine weeks, the pouches show definite signs of the dysplastic transformation leading to cancer, without any malignancies which often take up to 20 weeks to form in this model.<sup>58-64</sup> The left cheek pouch was coated three times weekly for the same time period with acetone alone to serve as an internal control. Five additional hamsters had measurements made in both cheek pouches prior to and immediately following four days of applying 0.5% SLS in DMSO in order to induce benign pathological changes.<sup>100, 101</sup> None of the hamsters in this study displayed signs of systemic toxicity during the study and all animal protocols were approved by the University of Florida Institutional Animal Care and Use Committee.

### **Collection of DLIPS and Fluorescence Spectra**

Spectra were collected using a fiber optic probe coupled to a DLIPS system as previously described (Chapter Two).<sup>38</sup> The fiber probe (Ocean Optics, Dunedin FL) used in these experiments consists of a ring of seven angled solarization-resistant fibers to direct both the 193 nm perturbation beam and the 355 nm excitation beam toward the sample. Between fiber tips and the tissue is a 2.0 mm thick window of UV grade fused silica, to permit relatively undiminished transmission of the excimer laser light. Fluorescence emission from the tissue is collected with a single center fiber. Using this configuration, the excimer perturbation pattern the same size or larger than the surface area sampled for emitted light. The emission is then focused from the fiber probe onto a fiber optic bundle using a combination of two 50 mm diameter UV-grade lenses, where

it is passed to a 0.3 m Czerny-Turner spectrometer and recorded with an intensified CCD (ICCD) array detector. Prior to entering the fiber optic, two sharp-edge filters are used in series: a high-pass filter designed to block the residual 355 nm light, and a low-pass filter designed to block any residual 532 nm light remaining from the frequency-tripling process. This allows spectra from the tissue to be collected from about 390 nm to 500 nm.

At weeks eight and nine of the study, all five of the hamsters had laser-induced fluorescence measurements made in each of their cheek pouches for a total of ten measurements in control tissue and ten measurements of dysplastic tissue. Prior to application of the SLS solution, measurements were made in each cheek pouch of the five animals in this group to give ten additional control measurements. After the four-day course of SLS treatment, these hamsters again had measurements made in each cheek pouch, serving as measurements of benign pathological changes. Before each measurement, the probe was wiped clean with methanol and rinsed with water, and the pouch was inspected for debris. Hamsters were anesthetized using a ketamine/xylazine solution (Phoenix Pharmaceutical, St. Joseph MO; Lloyd Laboratories, Shenandoah IA) at 10 ml/kg of body weight. The fiber optic probe was inserted into the pouch of the anesthetized animal and a fluorescence spectrum was recorded across a 1 mm diameter tissue area using a 200 shot ensemble average recorded at 5 Hz laser repetition rate (Figure 4-1). Immediately following this pre-perturbation fluorescence measurement, the 193 nm excimer laser was used to deliver a total of 2500 perturbation pulses to the target spot with laser energy of 100  $\mu\text{J}/\text{pulse}$  (fluence = 2  $\text{mJ}/\text{cm}^2$ ) and a laser repetition rate of 50 Hz. Approximately 30 seconds

after perturbation, a second fluorescence spectrum was recorded using an identical 200 shot ensemble average to collect a post-perturbation spectrum. These two spectra were then subtracted to generate the difference spectrum at each location, with the difference divided by the pre-perturbation spectrum to generate the DLIPS response for the given surface site.

### **Histopathology**

After week nine, the DMBA-treated hamsters were euthanized and the cheek pouches were excised and fixed in formalin (Sigma-Aldrich, St. Louis MO). Likewise, immediately after measurements were made in the SLS cheek pouch, that tissue was harvested and fixed. Fixed samples were sectioned at 5  $\mu\text{m}$  and stained with hematoxylin and eosin (H&E). Tissue preparation was performed at the Cell and Tissue Analysis Core, McKnight Brain Institute, University of Florida (Gainesville FL). The sections were read by a board-certified oral pathologist, and diagnosed based upon established criteria for dysplasia.<sup>12</sup>

### **Dimensional Reduction and Subspace Analysis**

During the collection of spectra, the shape and signal strength were actively monitored, and measurements were rejected and repeated if the fluorescence measurement was well out of the expected range (approaching an order of magnitude increase or decrease). In these cases, the probe was re-cleaned, the cheek of the hamster was wiped and the probe was repositioned to take another measurement. In another case, the root cause behind a set of low signal-to-noise measurements turned out to be low excimer laser fluence, so the entire set of measurements was repeated.

Following this process, the spectra (pre-perturbation fluorescence and DLIPS) for all four groups were imported into MATLAB<sup>®</sup> (The Mathworks, Natick MA) for

processing. Difference spectra and fluorescence spectra were preprocessed using a twenty five-point moving average (a range of less than 5 nm in wavelength) filter to remove acquisition noise. Fluorescence and DLIPS spectra were then analyzed separately, but using parallel methods, to facilitate side-by-side comparison at each analytical level. Spectra from the treated and control groups were grouped together and decomposed using principal component analysis (PCA) for up to ten components for each technique. Clustering within the data sets was visualized using score plots of the first two components and the validity of using the PCA basis for further analysis was determined by considering both the percent of variance explained by each component and a one-way Analysis of Variance (ANOVA) in each component to test for statistically-significant differences between the three experimental groups. Individual group differences were assessed using Tukey-HSD post-hoc analysis, and two groups were considered different at a 95% confidence level.

To consider the different clinical testing, algorithm training, and contrast mechanisms possible for DLIPS-based diagnostic devices or fluorescence-based devices, data from the three experimental groups (dysplastic pathology, benign pathology, and no pathology) was clustered into six binary detection groupings. For each of these six binary groupings, a transformation of the spectral data was performed to reduce the dimensionality of the spectrum down into the optimal one-dimensional subspace for that binary detection problem. This was done by applying the change of basis described in Equations 4-2 and 4-3, using Fisher's Linear Discriminant,  $B$ , where  $H_0$  and  $H_1$  represent the two data classes being used to construct the linear transform,  $\mu$  is the mean vector for each data set and  $\sigma$  is the covariance matrix.<sup>102</sup> This

maximizes the separation between the two classes while at the same time reducing the dimensionality of each observation from  $y_x$  to  $b_x$ . A limitation of this approach is that the dimensionality of the original data set must be less than or equal to the smallest number of observations with a group.<sup>102</sup> In this study, the dimensionality of the original spectral data was reduced to 10 dimensions (the number of observations in each experimental group) using PCA prior to computation of, and transformation using Fisher's Linear Discriminant.

Using this framework, the signal-to-noise ratio (SNR) for detection in that basis was computed using Equation 4-4 below and as a reference the SNR prior to the transform was also calculated by substituting out Fisher's vector  $B$  for a one's vector,  $J$  (Equation 4-1).<sup>102</sup>

$$SNR(H_0, H_1) = \frac{\sigma_{bnw}^2}{\sigma_{w/n}^2} = \frac{(\bar{J}_{n \times 1} \cdot (\bar{\mu}_{H_1} - \bar{\mu}_{H_0}))^2}{\bar{J}_{n \times 1}^T (\Sigma_{H_0} + \Sigma_{H_1}) \bar{J}_{n \times 1}} \quad (4-1)$$

$$\bar{B} = (\Sigma_{H_0} + \Sigma_{H_1})^{-1} (\bar{\mu}_{H_1} - \bar{\mu}_{H_0}) \quad (4-2)$$

$$b_x = \bar{B} \cdot \bar{y}_x \quad (4-3)$$

$$SNR(H_0, H_1) = \frac{\sigma_{bnw}^2}{\sigma_{w/n}^2} = \frac{(\bar{B}_{n \times 1} \cdot (\bar{\mu}_{H_1} - \bar{\mu}_{H_0}))^2}{\bar{B}_{n \times 1}^T (\Sigma_{H_0} + \Sigma_{H_1}) \bar{B}_{n \times 1}} \quad (4-4)$$

While the change of basis transformation and the SNR are only dependent upon the two data groups selected to compute the transformation, the transform can be applied to the entire data set, independent of class association or use of the data when computed the transformation, which occurred for this study.

## Classification Framework and Detection Performance

To assess the appropriateness for detecting oral pre-malignancies, benign pathology or healthy oral mucosa in each of the six detection bases, a maximum a posteriori (MAP) test was used to predict the class associations.<sup>103</sup> In this case, for each measurement taken, class association was predicted by selecting the most probable class, as estimated from the a posteriori probability of that measurement coming from each class (ie: a test of the likelihood of each class given the observation).<sup>103</sup> The conditional probabilities of each of the 30 observations were estimated by a multi-parametric fit of mean, standard deviation, skewness, and kurtosis to find the most appropriate parametric distribution for the observations from that class. The Johnson System of distributions was used to for fitting the conditional probability distribution and estimates to the parameters (mean, standard deviation, etc.) were made directly from the observations using a maximum likelihood estimation-least squares approach.<sup>104, 105</sup> In total, three conditional probabilities,  $P(y|H_x)$ , were estimated in each basis, supported in all cases by ten observations of that class. Equations 4-5 and 4-6 below summarize the MAP classification criteria for the three groups.

$$P(H_x | y) = \frac{P(y | H_x)P(H_x)}{\sum_{i=0}^n P(y | H_i)P(H_i)} \quad (4-5)$$

$$\max[ P(H_0 | y) \dots P(H_n | y) ] \quad (4-6)$$

Where  $P(H_x|y)$  represents the a posteriori probability of class  $H_x$  given the observation  $y$ , and  $P(H_x)$  is the prior probability of that class occurring in the population.<sup>103</sup> This test was used to assign predicted class to the data points in all cases.

To explore the improved discrimination in each of the six bases, a simple one-way ANOVA with Tukey-HSD post-hoc analysis (as above for the PC-transformed data) was performed on the transformed data to determine if the groups were statistically significantly different following application of the Fisher transformation.

For each of the six detection bases, a confusion matrix of the three-class problem was constructed. Both row and column statistics within the confusion matrix were computed, as analogs of sensitivity and specificity, for the multi-class problem. The metrics used were Precision, the fraction of observations that were correctly assigned to that class, and Recall, the fraction of the members of a particular class correctly assigned to it.<sup>102</sup> To collapse these values into a concise representation of the performance of DLIPS and fluorescence to accurately detect each disease state, the overall Accuracy of correct classification was computed. Unfortunately, for multi-class problems there is no well-established framework for describing the detection performance across all decision thresholds (ie: ROC curve and AUC), and as a consequence does not permit tuning of the detection threshold to explore the optimal operating points and compare this to estimated operating points for clinical devices.<sup>106</sup>

## **Results**

### **Histopathology**

Figures 4-3 (A-C) are representative photomicrographs of the H&E sections of hamster cheek pouches from the control group, SLS-treated group, and DMBA-treated group respectively. The completely untreated cheeks and those treated with carrier (acetone only) for eight weeks appeared histologically indistinguishable, and a representative section of control cheek is shown in Figure 4-3 (A). The epidermis was of normal thickness and consistent throughout the sections. The layers were well defined,

with a thin, consistent layer of keratinization on the surface and a clearly defined, smooth basement membrane layer separating the basal cells and the lamina propia.

Figure 4-3 (B) shows the cheek pouch after four days of SLS application. These pouches displayed moderate epithelial changes including hyperkeratosis, acanthosis, and hypergranulosis. These findings were consistent with other studies using this a model of inflammatory benign pathology.<sup>100, 101</sup> Visual and tactile examination of pouches prior to excision showed evidence of increased toughening of the oral mucosa, as assessed by some loss in elasticity and a cloudiness beginning to obscure visualization of the sub-epithelial vessels (Figure 4-2).

Figure 4-3 (C) shows a section from a cheek pouch after 8 to 9 weeks of DMBA application. This particular section is through a verrucoid papillary mass, consistent with a pre-neoplastic lesion found in human with a high incidence of transforming into an invasive carcinoma.<sup>107</sup> Obvious morphological dysplastic characteristics of this section include: extreme hyperkeratosis, drop-shaped rete ridges, abnormal epithelial maturation, and a loss of cellular cohesiveness, in addition to cellular and nuclear changes. Visual and tactile exam showed a low incidence of papillomas (less than one per pouch) and no obvious ulcerations in the pouch despite clear visual evidence of oral pathology including large patches of leukoplakia and small lesions resembling erythroplakia (Figure 4-2) as well as a clearly abnormal stiffness associated with this generally elastic tissue.

### **Spectral Analysis**

Figure 4-4 shows the average fluorescence spectra and Figure 4-5 shows the average DLIPS spectra of the DMBA treated cheek pouches versus SLS treated and the control pouches. The fluorescence spectra collected from the cheek all resemble

each other in shape but are scaled differently for the three groups. The most prominent spectral features are a peak around 460 nm as expected from NADH, but also a surprising peak at 395 nm. Despite the averaging, the spectra are quite noisy, likely due to the low levels of light collected through the collection fiber of the probe as well as the added noise as the light propagates through the fibers to the detector. The DLIPS spectra on the other hand, show both a change in signal intensity as well as a change in shape between groups; despite the apparently low signal-to-noise ratio. The control and dysplasia spectra resemble one another in shape but vary greatly in signal intensity. The SLS spectrum, while overlapping the control spectrum, shows pronounced shape difference above 430 nm unique from the other groups.

### **Subspace Analysis**

Figure 4-6 shows the percent of variance explained by each principal component. Correspondingly, Figure 4-7 shows identical analysis of the DLIPS data. In both cases 30 total spectra were used, 10 from the DMBA-treated hamsters, 10 from the SLS-treated hamsters, and 10 from the acetone-treated hamsters.

In addition to assessing each component in terms of the amount of total data variance encoded in that dimension, an equally important metric is to determine whether the variance is specifically representative of the between-group variance (ie: the particular principal component dimension preserves or enhances difference between observations of dysplastic tissue versus benignly-inflamed tissue versus health tissue). Using one-way ANOVA, it was discovered that the group means are significantly different in components one, two, and three for the fluorescence measurements, but only in components two and eight for the DLIPS measurements. To further explore the difference between the groups, Tukey-HSD post-hoc analysis was performed. For

fluorescence measurements, differences between dysplastic and benign pathology data groups were significant under PC's one and two, while differences between control and dysplastic groups were significant under PC three. For DLIPS measurements, differences between control and benign pathology data groups were significant under PC's two in addition to differences between the benign and dysplastic pathology data groups. Differences between benign pathology and control groups were significant under PC eight. The lack of a convergence in the principal component space in terms of finding a PC dimension that both describes a large proportion of the variance as well as having significant differences between the three measurement groups indicates that the PC basis is not an appropriate basis for describing the inherent differences between groups that are captured when making either fluorescence or DLIPS measurements. The studies in this work however are not designed to evaluate whether this is inherent to the particular of the detection problem, technique, or the noisiness of the data.

To find a more appropriate basis for describing the differences between the three groups, six transformations for both fluorescence and DLIPS were constructed from the collected cheek pouch measurements. Figure 4-8 shows the six binary classification strategies possible for the three-class problem. In particular the data contained in these six partitions formed the basis for the transformation into the optimal detection dimension using Fisher's Linear Discriminant (FLD). It should be noted however, that this change of basis is only optimal for the two groups being compared in columns  $H_0$  and  $H_1$ , there is no conditioning for a third data class. Further, in each of the six scenarios, the SNR reported both pre- and post-transformation only represents the distance between groups  $H_0$  and  $H_1$ . In comparing the DLIPS data and the fluorescence

data, the fluorescence data has a higher SNR for all cases, except when comparing in the basis of benign lesions versus healthy oral mucosa; a rather trivial basis for comparison or construction of a detection device. For fluorescence, the largest values of SNR always come from a detection basis that has the dysplastic tissue as a specific point of contrast with respect to the rest of the data, not unlikely previous finding where fluorescence spectroscopy has been shown to have a high sensitivity and specificity for detecting oral pre-malignancies against healthy oral mucosa in the hamster cheek pouch.<sup>97</sup> Further, based on analysis of the histopathological section of the dysplastic cheek pouches, a large change in the optical and fluorescent properties should be expected. For the transformations of the DLIPS data however, all of the SNRs after applying the transformations are fairly consistent. This may indicate that the DLIPS measurements are more balanced in detecting points of contrast among all three of the tissue groups, or this may indicate that high noise levels in the experimental measurements are obscuring any dramatic contrast between the three target tissue types.

Unlike the SNR, an ANOVA test accounts the differences between all three of the group means but unfortunately only considers if at least one mean is statistically different from the others. Figures 4-8 and 4-9 show the p-values for an ANOVA test of the three groups under each transformation for fluorescence and DLIPS measurements respectively. As expected, in all cases at least one group measure was found to be significantly different from the other because the nature of the FLD transformation is to maximize the distance between two groups while minimizing the variance within each of the two groups. Ideally however there exists an FLD transformation that also preserves

or enhances the differences between the three groups. This was not discovered in any of the cases for either fluorescence or DLIPS and this again could be due to the high noise levels in the original measurements or that a one-dimensional projection of this data is insufficient to optimally describe the differences between the three groups as well as similarities within groups.

If the goal of the technique is to discriminate pre-malignant pathology from anything else then only the transformations that demonstrate this ability should be considered as options to explore further for the details of classification performance. These are highlighted in yellow in Figures 4-9 and 4-10 as post-hoc analysis showed that under these particular transformations both the benign pathology and the healthy oral mucosa appeared different from the dysplastic tissue.

### **Measurement Classification**

Figures 4-11 through 4-13 correspond to the confusion matrices from transformations T1, T2, and T4 in Figure 4-8 for the fluorescence measurements. Figure 4-14 is the confusion matrix for transformation T4 in Figure 4-8 for the DLIPS measurements. These are the highlighted transformations in Figures 4-9 and 4-10 respectively. Despite not meeting the post-hoc analysis criteria for utility as a detection basis when making DLIPS measurements, the confusion matrix for transformation T2 is shown as well because of the high classification accuracy (Figure 4-15).

The best detection performances across all three classes (dysplasia, benign pathology, healthy oral mucosa) were in bases where the dysplastic tissue was isolated as one of the two grouping for constructing the change of basis (highlighted in Figure 4-9). While each of these bases for detection showed excellent performance in finding dysplasia (100% Precision and Recall), the basis optimized around comparing benign

pathology and dysplastic tissue had the highest overall accuracy at 83%. This implies that for this model, dysplastic tissue has a very distinct signature because these numbers do not reflect the performance predicted from commercially-available systems.<sup>3, 13</sup> Another possibility is that these algorithms that consider the benign pathology as well as healthy oral tissue in contrast to dysplastic tissue are uniquely suited to diagnostic tissue fluorescence.

For classifications using the DLIPS measurements, the performance in terms of finding dysplasia was overall worse than using fluorescence alone, but not by a lot. Under transformation T4, the Precision was 80% and the Recall was 89%. Overall the Accuracy was only 60% as the DLIPS technique tended to confuse benign pathology and healthy oral mucosa. Under transformation T2, the Precision was 100% and the Recall was 91% for finding dysplasia and the overall accuracy was 87%. While this overall accuracy is higher than the number reported for using fluorescence alone, the metrics for finding dysplasia are marginally worse. It remains to be seen if these numbers accurately represent the performance of using the DLIPS technique to detect oral dysplasia or merely point out the increased sensitivity of this technique to measurement noise.

## **Discussion**

Despite the shortcoming of this study in providing support for the DLIPS technique in the detection of oral cancer, a more fundamental question with regard to optical detection of oral cancer was addressed: What is the correct detection problem to target devices towards in order to improve diagnostic accuracy and reduce the false positive rate.

The extremely low values for the fluorescence spectra and the DLIPS spectra (Figures 4-4 and 4-5) are likely related to a lack of fluorescence light returning through the fiber probe to the detector. As shown previously in Chapter 1, the DLIPS signal must overcome an order of magnitude more measurement noise than the individual fluorescence measurements so in this case since the fluorescence levels were so low, the DLIPS signals were almost completely buried in noise. The large error bars and 25 point moving average associated with Figures 4-5 support this notion. As a result of this noise, pathology classification using the DLIPS data (Figures 4-14 and 4-15) was uniformly worse than when using fluorescence alone. Despite this, the results presented here indicate that by solving this signal-to-noise problem for the DLIPS system, improved detection performance should be possible.

Figures 4-11 to 4-13 show that dysplasia can be detected with 100% accuracy and no false positives when using fluorescence detection. While this is a great result in terms of the overall goal for oral cancer detection devices, these results are not consistent with what is typically reported for clinical measurements.<sup>3, 13</sup> Future work applying optimal detection theory to the improvement of oral cancer diagnostic devices should address this, by either relaxing the criteria for consider tissue pre-malignant, thereby modeling even earlier stages of disease, considering multiple benign pathology, or by simply increasing the number of measurements/ test subjects.

The overall best performance for finding dysplasia was reported in Figure 4-11, for the classifier constructed by emphasizing the differences between benign pathology and dysplasia. It is possible that detecting benign pathology over dysplastic pathology is an inherently harder detection problem than discovering healthy tissue over dysplasia and

by optimizing on that basis, the need to consider contrast with healthy tissue is obviated. Typically, systems are trained or inherently designed to differentiate between healthy tissue and dysplasia. Take for example the Velscope system which uses loss of fluorescence as its biomarker of oral cancer and pre-malignancies.<sup>17, 20</sup> Since the system relies upon comparative visual inspection with the remainder of the (presumably healthy) oral mucosa to detect this LOF, this device inadvertently operates in the detection regime of dysplasia versus benign tissue; although there is no optimization of the detection scheme in this case, it is simply the detection criteria being employed for this device. So there is little consideration given to ability to uniquely differentiate benign pathology from dysplastic tissue and as such these devices commonly detect the LOF from leukoplakias and other lesions as cancerous when they are not.<sup>13, 16, 17</sup>

But is it feasible to train and test devices for the basis comparing benign pathology and dysplastic pathology? Pre-clinically, this is not problematic (as demonstrated here) but clinically, it could present a hurdle, as a gold-standard for the evaluation of benign pathology (ie: biopsy) is not always available. That is because clinical testing protocols calling for biopsy of oral tissue that would not otherwise require biopsy is considered unethical.<sup>3</sup> Therefore other experimental means must be sought to realize the potential for enhanced detection capabilities by designing instruments to focus on the harder, but more clinically-relevant problem of sorting benign lesions from dysplastic lesions. This could include continuing to develop more accurate animal model of human oral pathology or attempting to better understand the feature-based sources of contrast within each type of oral tissue and design instruments around those

detection requirements, visualizing the differences between benign pathology and dysplastic lesions.

Even though the ultimate priority for tuning these instruments is detection of cancerous and pre-malignant lesions above all other classes (presumably lumped together), here we demonstrate that by rethinking the methodology for training and testing these systems; instead optimizing for contrast between dysplastic and benign lesions, improvements in detection accuracy can be realized. By using this basis for contrast it is further expected that the rate of false positives due to benign lesions could be reduced and the specificity of these devices for finding oral pre-malignancies could be enhanced, but it is unclear from these results as no false dysplasias were detected for transformations with the best performance (Figures 4-11 to 4-13).



Figure 4-1. Fiber probe used for DLIPS and fluorescence measurements in the hamster cheek pouch



Figure 4-2. Pictures of everted cheek pouches displaying the model pathologies used in this study. A) Healthy oral mucosa. B) DMBA-treated buccal tissue displaying a clear thickening and loss of elasticity, characteristic of the pre-malignant transformation. C) DMBA-treated buccal tissue displaying flat regions of leukoplakia as well as a small velvety erythroplakia lesion. D) SLS treated oral mucosa displaying a smoother, thicker layer of epithelial tissue and a loss of elasticity.

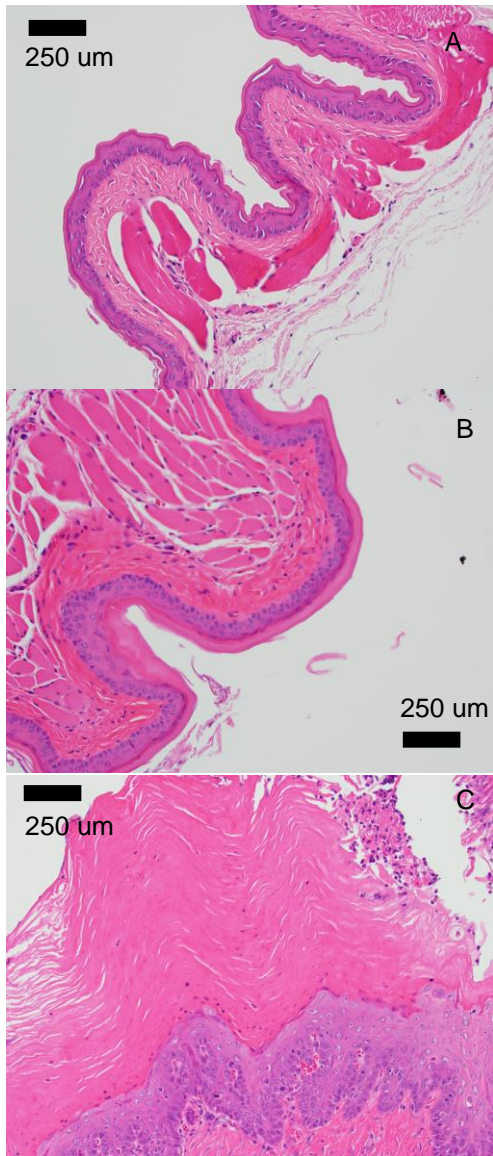


Figure 4-3. H&E stained histology sections of cheek pouches. A) Control hamster (no treatment or carrier alone). B) SLS-treated hamster. C) DMBA-treated hamster at week 8 or 9. A) shows healthy, well-organized section of superficial keratin, epithelium, and lamina propia. B) shows obvious signs of irritation. C) is specifically a section through a verrucopapillary mass, a clear sign of dysplastic transformation

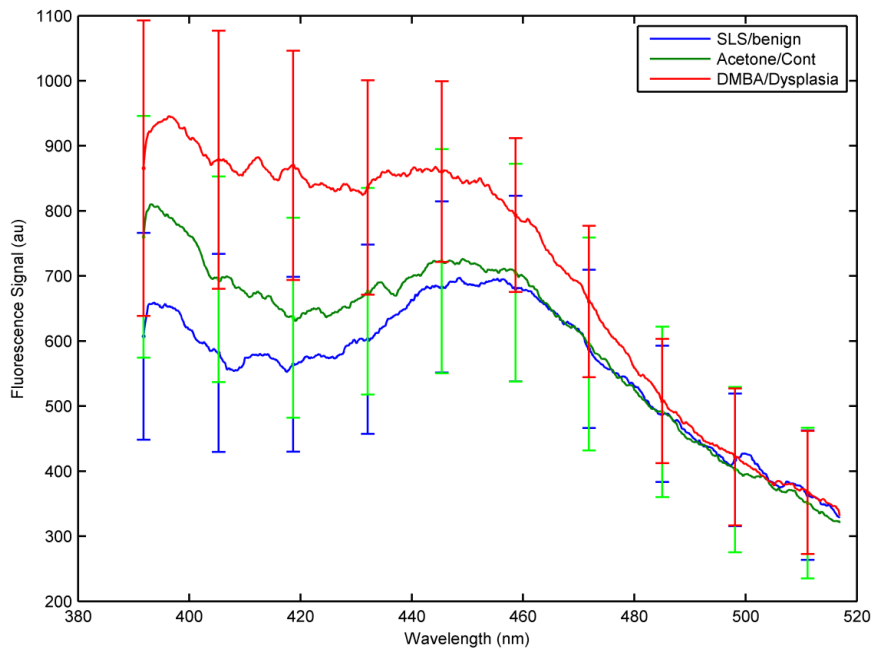


Figure 4-4. Average fluorescence spectra from 10 SLS-treated benign irritation cheek pouches (blue), 10 carrier only-treated control cheek pouches after 8 or 9 weeks of application (green), and 10 DMBA-treated dysplastic cheek pouches after 8 or 9 weeks of application (red)

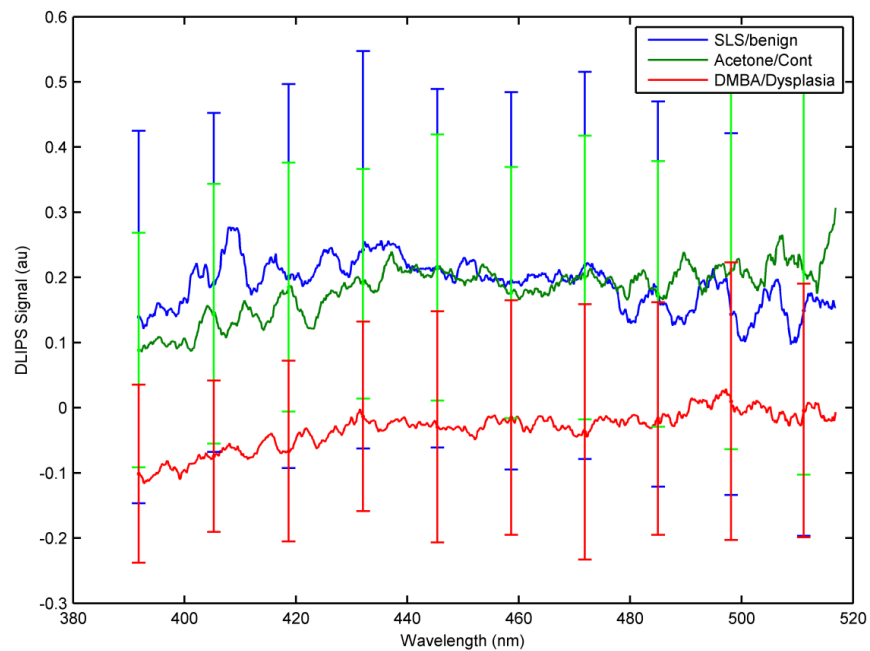


Figure 4-5. Average DLIPS spectra from 10 SLS-treated benign irritation cheek pouches (blue), 10 carrier only-treated control cheek pouches after 8 or 9 weeks of application (green), and 10 DMBA-treated dysplastic cheek pouches after 8 or 9 weeks of application (red)

Principal Component	% Variance Explained	Tukey-HSD post hoc analysis (p<0.05)			
		ANOVA P-value	Benign v. Control	Benign v. Dysplasia	Control v. Dysplasia
1	87.064	<b>0.025</b>	F	<b>T</b>	F
2	9.706	<b>0.010</b>	F	<b>T</b>	F
3	1.379	<b>0.009</b>	F	F	<b>T</b>
4	0.677	0.428	-	-	-
5	0.164	0.187	-	-	-
6	0.127	0.704	-	-	-
7	0.113	0.392	-	-	-
8	0.086	0.144	-	-	-
9	0.081	0.761	-	-	-
10	0.076	0.127	-	-	-
Residual Data Variance	0.527				

Figure 4-6. Percent of variance explained by each of the first ten principal components, p-values for the ANOVA between the three experimental groups (in each principal component), and post-hoc analysis to determine which group means are significantly different for the laser-induced fluorescence data

Principal Component	% Variance Explained	Tukey-HSD post hoc analysis (p<0.05)			
		ANOVA P-value	Benign v. Control	Benign v. Dysplasia	Control v. Dysplasia
1	91.495	0.063	-	-	-
2	3.786	<b>0.015</b>	<b>T</b>	<b>T</b>	<b>F</b>
3	0.898	0.314	-	-	-
4	0.645	0.477	-	-	-
5	0.414	0.376	-	-	-
6	0.388	0.338	-	-	-
7	0.291	0.874	-	-	-
8	0.239	<b>0.025</b>	<b>T</b>	<b>F</b>	<b>F</b>
9	0.222	0.901	-	-	-
10	0.199	0.257	-	-	-
Residual Data Variance	1.424				

Figure 4-7. Percent of variance explained by each of the first ten principal components, p-values for the ANOVA between the three experimental groups (in each principal component), and post-hoc analysis to determine which group means are significantly different for the DLIPS data

Transformation	Group comparison to derive FLD transformation		Fluorescence		DLIPS	
	H0	H1	Pre-transform SNR	Post-transform SNR	Pre-transform SNR	Post-transform SNR
<b>T1</b>	Dysplasia	Benign	1.909	21.013	0.579	5.679
<b>T2</b>	Dysplasia	Control	1.084	18.823	0.788	8.020
<b>T3</b>	Benign	Control	0.211	2.899	0.041	3.780
<b>T4</b>	Dysplasia	Benign or Control	2.076	25.612	0.714	3.437
<b>T5</b>	Benign	Dysplasia or Control	0.918	4.803	0.331	4.008
<b>T6</b>	Control	Dysplasia or Benign	0.079	3.768	0.052	3.157

Figure 4-8. Data groups used to derive the six FLD transformations as well as the corresponding SNR between the  $H_0$  and  $H_1$  data group pre- and post-transformation

Fluorescence Transformation	Tukey-HSD post hoc analysis (p<0.05)			
	ANOVA P-value	Benign v. Control	Benign v. Dysplasia	Control v. Dysplasia
T1	9.1E-13	F	T	T
T2	1.6E-13	F	T	T
T3	0.00091	T	T	F
T4	2.1E-14	F	T	T
T5	3.6E-07	T	T	F
T6	1.7E-06	T	F	T

Figure 4-9. ANOVA and Tukey-HSD post-hoc analysis of the transformed fluorescence measurements

<b>DLIPS</b>		Tukey-HSD post hoc analysis ( $p < 0.05$ )		
	ANOVA	Benign v.	Benign v.	Control v.
Transformation	P-value	Control	Dysplasia	Dysplasia
T1	0.00135	<b>T</b>	<b>T</b>	F
T2	0.00334	F	<b>T</b>	F
T3	7.1E-05	<b>T</b>	<b>T</b>	F
<b>T4</b>	2.3E-05	F	<b>T</b>	<b>T</b>
T5	8.2E-06	<b>T</b>	<b>T</b>	F
T6	7.3E-05	<b>T</b>	F	<b>T</b>

Figure 4-10. ANOVA and Tukey-HSD post-hoc analysis of the transformed DLIPS measurements

		Predicted Class		
		Benign	Control	Dysplasia
Actual Class	Fluor T1			
	Benign	8	2	0
	Control	3	7	0
Dysplasia	0	0	10	
	Precision	0.80	0.70	1.00
	Recall	0.73	0.78	1.00
	Accuracy	0.83		

Figure 4-11. Confusion matrix for the fluorescence data under transformation T1

		Predicted Class		
		Benign	Control	Dysplasia
Actual Class	Fluor T2			
	Benign	2	8	0
	Control	3	7	0
Dysplasia	0	0	10	
	Precision	0.20	0.70	1.00
	Recall	0.40	0.47	1.00
	Accuracy	0.63		

Figure 4-12. Confusion matrix for the fluorescence data under transformation T2

		Predicted Class		
		Benign	Control	Dysplasia
Actual Class	Fluor T4			
	Benign	4	6	0
	Control	4	6	0
Dysplasia	0	0	10	
	Precision	0.40	0.60	1.00
	Recall	0.50	0.50	1.00
	Accuracy	0.67		

Figure 4-13. Confusion matrix for the fluorescence data under transformation T4

		Predicted Class			
		DLIPS T4	Benign	Control	Dysplasia
Actual Class	Benign	2	8	0	
	Control	1	8	1	
	Dysplasia	0	2	8	
		<b>Precision</b>	0.20	0.80	0.80
		<b>Recall</b>	0.67	0.44	0.89
		<b>Accuracy</b>	0.60		

Figure 4-14. Confusion matrix for the DLIPS data under transformation T4

		Predicted Class			
		DLIPS T2	Benign	Control	Dysplasia
Actual Class	Benign	6	3	1	
	Control	0	10	0	
	Dysplasia	0	0	10	
	<b>Precision</b>	0.60	1.00	1.00	
	<b>Recall</b>	1.00	0.77	0.91	
	<b>Accuracy</b>	0.87			

Figure 4-15. Confusion matrix for the DLIPS data under transformation T2

## CHAPTER 5 CONCLUSION

The work in this dissertation focused on the development of DLIPS fluorescence biosensing, a new spectral technique, into a clinical detection technique, with the long-term goal of improving clinicians' ability to detect and diagnose oral pre-malignancies earlier and with enhanced accuracy. Here we presented a proof-of-concept study (Chapter 2) in mice that established a key fundamental fact: DLIPS can be used to discriminate pathological tissue from healthy tissue *in vivo*. Further, when comparing this technique to fluorescence spectroscopy alone, it was found to perform at least as well as this technique; one which is seeing success in clinical trials for diagnosing disease using advanced techniques, but has seen mixed results in the currently available commercial systems.

In an effort to understand the utility and opportunity for maximizing DLIPS clinical benefit, a fluorescence-photochemical Monte Carlo model of the DLIPS technique was constructed (Chapter 3). Here it was discovered that DLIPS in fact highlights unique regional and fluorescent properties of disease that were previously inaccessible using fluorescence spectroscopy alone. This builds support for the case that DLIPS biosensing could stand alone as a diagnostic technique or can complement detection systems for oral pre-malignancies by providing an orthogonal dimension of information.

Finally, in a pre-clinical assessment of this technique as a tool for detecting oral cancer (Chapter 4), while DLIPS failed to demonstrate superior detection capabilities due to extremely low signal levels, the investigation of fluorescence detection in this multi-class framework demonstrated that by using detection theory, the discrimination can potentially be enhanced. This result implies that by designing systems for solving

the detection problem of discriminating benign pathology from oral pre-malignancies, the most common problems associated with currently marketed diagnostic aids can be mitigated. Specifically, this work demonstrates that this particular design and testing strategy can reduce the high false positive rate associated with screening, without trading sensitivity to oral dysplasia.

Overall, this dissertation provides the experimental and theoretical links between DLIPS as an abstract technique, diagnostic tissue spectroscopy, and the unmet need in oral pre-malignancy detection. This work represents an important step forward for DLIPS biosensing techniques, extending the capabilities of this technique from *in vitro* applications to *in vivo* diagnostics. Results from both modeling and experiments confirm that DLIPS accesses fundamentally different biomolecular information than fluorescence spectroscopy alone. These results represent the foundation for the extension of this biosensing technique to other diseases as well as the coupling of laser-induced perturbation with other sensing modalities (Raman, magnetic resonance, other optical spectroscopies). Further, for *in vitro* applications, the results from the Monte Carlo models in Chapter 4 imply a dual mechanism for inherent contrast associated with DLIPS: optical clearing of superficial interference and direct coupling to cleaved biomolecules. This combination mechanism is a critical advantage of the DLIPS technique and in the Monte Carlo models accounted for the interrogation of FAD and keratin respectively (biomolecules inaccessible in the fluorescence spectra alone).

While there is not an immediate, direct impact for DLIPS on oral cancer detection due to the long regulatory path to clinical testing, these results confirm two important general facts about effective optical tools for non-invasive screening and diagnosis. First

is that there are some fundamental flaws with currently technologies in terms of what information is integrated into the returned signal from the tissue. Specifically, the results in Chapter 3 indicate that fluorescence spectra from tissue heavily emphasize information from the stroma and basal epithelium, obscuring information from the superficial epithelial layers. In this same study, it was shown that DLIPS in fact targets these superficial structures, where other studies have shown that some of the earliest morphological and biochemical changes occur leading to oral malignancies.<sup>29, 90, 92</sup> This result is disruptive to the market for oral cancer adjuvants as none of these instruments currently provide depth-selectivity or target biomolecule selectivity, but this selectivity could be a critical feature for a successful diagnostic aid.

Second, in Chapter 4 this work demonstrated that devices trained to discriminate benign pathology from dysplasia provide overall better diagnostic performance in animal models. This is again disruptive as the current design archetype relies upon “training” or design to discriminate known dysplastic lesions against healthy oral mucosa (eg: loss-of-fluorescence). What this design paradigm does not consider is the specificity of the observed contrast for cancer versus other pathologies; this supposed to be a key factor driving down detection performance for current commercial devices. Implementation of this strategy is not easy and will require new and more rigorous approaches to clinical validation and testing, lengthening time-to-market and development costs. At the same time, the opportunity to drive up 5-year survival rates for oral cancer is immeasurably valuable.

There are several important next steps for the development of in vivo DLIPS-based screening and diagnostic technologies. Primarily these studies revolve around

continuing to build the theoretical basis for this technique as well as confirming the results presented in this dissertation. One important next step is to better optimize this technique for in vivo analysis. Based on the results in Chapters 3 and 4, it is clear that while DLIPS should minimize inter-patient variability, it has a very low tolerance for measurement noise. This can likely be mitigated somewhat by averaging multiple measurements before and after perturbation or rethinking how to focus the excitation beam and collection optics to decrease the fluorescence interaction volume. If the volume of fluorescence interactions at 355 nm is around 100 times larger than the footprint of photochemical interactions, then the majority of that remitted fluorescence is cluttering assessment of the photochemical changes induced by the perturbation beam. If the goal is a more localized analysis of the perturbation region then optical strategies for targeting that tissue specifically should be considered. Or potentially coupling this technique with a more superficial spectral analysis technique, such as resonance Raman with a shorter wavelength UV excitation laser to better restrict the penetration depth and focus more on the superficial signals. In short, there is a good deal of optimization work to be done on this technique, but the results provided here give a firm starting point for incremental technical improvements.

Second, is establishing the safety profile for this technique, a key requirement to move forward into clinical testing. From the perspective of the Food and Drug Administration (FDA) as well as any Institutional Review Board, there are three apparent safety hazards associated with the current system that must be addressed. These are safety concerns regarding eye safety (with regards to the coherent light sources used in this device) for patients as well and healthcare professionals, the safety

of applying sub-ablative pulses of deep UV light to tissue in vivo, and protection from Fluorine gas exposure. In all of these cases there are pre-existing, FDA-approved clinical systems that can be used for patterning the design as well as provide supporting evidence for the safety profile of this device. Finally, optimization of the optical and mechanical design for portability and integration with existing minimally-invasive endoscopic systems could significantly broaden the applications of this technique to detecting other diseases such as cervical and colorectal cancer or atherosclerosis.

The long-term outlook for this technique as an in vivo biosensing modality is promising, if nascent, based upon the results presented here. This work enables the next steps forward for DLIPS as a non-invasive detection technique: translation into clinical studies of oral pathology, and extension to other target tissues and pathologies. Along the way, a clearer picture of some technical issues will be necessary to troubleshoot and optimize the diagnostic performance for this challenging biosensing setting. As the knowledge base for DLIPS technology continues to grow, other applications are discovered, and the application of DLIPS to superficial cancer detection matures, the full promise of this new spectral technique presented here will be realized.

## APPENDIX

### MATLAB® CODE FOR MONTE CARLO SIMULATIONS

```

%dlips_mc2.m
%Raymond Kozikowski
%Aug 1, 2012
%monte carlo code to describe dlips phenomena in tissue
%Assume that photons dont split, each photon is a discrete packet until it
%dies in the simulation
%USE ANGLES IN DEGREES!!!!

function out=dlips_mc2(model, no_pho, beam, mask_mu, mask_f)
tic
res=.5;      %pixels per um, assume pixels are square
width=10e3;  %width of the model (in um), to create an ~infinite width wrt
beam width (1mm)
randn('state',sum(100*clock)); %reinitilize randn each time the program runs
rand('state',sum(100*clock));
%define excitation and perturbation parameters
lambx=355;  %excitation in nm
lambp=193;  %perturbation in nm
%describe the probe optical properties
NA=.22;     %taken from the fiber properties
nARF=1.666; %assuming interface with a crystal quartz window
nfluor=1.56; %for fiber applications
nfluor=1;%for free beam laser applications

if strcmp(model, 'test')==0 && strcmp(model, 'test2')==0
%define tissue fluorophores (given as relative emission from tissue layers
%which correspond to dominant fluorophores
NADH=fluoro_fit([355 385 405 425 455 475 495 525 545 565],[0 .1 .29 .49 .69
.51 .41 .28 .2 .13],lambx);
FAD=fluoro_fit([475 495 505 525 535 545 565],[0 .025 .075 .12 .15 .12
.1],lambx);
Collagen=fluoro_fit([355 385 395 410 425 455 475 495 525 545 565],[0 .19 .35
.47 .35 .22 .14 .1 .06 .04 .03],lambx);
Keratin=fluoro_fit([355 385 405 425 455 475 495 525 545 565],[0 .07 .1 .11 .1
.08 .05 .03 .02 .01],lambx);
nNADH=sum(.5*(NADH{2}(2:end)+NADH{2}(1:end-1))./(NADH{1}(2:end)-
NADH{1}(1:end-1)));
nFAD=sum(.5*(FAD{2}(2:end)+FAD{2}(1:end-1))./(FAD{1}(2:end)-FAD{1}(1:end-
1)));
nCollagen=sum(.5*(Collagen{2}(2:end)+Collagen{2}(1:end-
1))./(Collagen{1}(2:end)-Collagen{1}(1:end-1)));
nKeratin=sum(.5*(Keratin{2}(2:end)+Keratin{2}(1:end-1))./(Keratin{1}(2:end)-
Keratin{1}(1:end-1)));
NADH2=(NADH{1}(2)-NADH{1}(1))*NADH{2}/nNADH;
FAD2=(NADH{1}(2)-NADH{1}(1))*FAD{2}/nFAD;
Collagen2=(NADH{1}(2)-NADH{1}(1))*Collagen{2}/nCollagen;
Keratin2=(NADH{1}(2)-NADH{1}(1))*Keratin{2}/nKeratin;

%load and convert your hemoglobin data (mu_a, cm-1)

```

```

hb_mat=load('C:\Users\Owner\Desktop\dissertation\refs for
MC\hb_ext_spectra.txt');
hb_mat(1:end,2:3)=hb_mat(1:end,2:3)*2.303*150/64500;

%change me for healthy versus disease
if strcmp(model, 'cheek')==1
    blood_frac=.002;
else
    blood_frac=3*.002;
end

O2_frac=.8;
%skin_bkgd_mua=0.244+85.3*exp(-(hb_mat(1:end,1)-154)/66.2);           %Jacques
approx for background
skin_bkgd_mua=7.84e8.*hb_mat(1:end,1).^(-3.255);                     %Saidi
approx for bkgd (maybe used in Pavlova?)
wave_bkgd=193:1:1000;
%skin_bkgd_mua2=0.244+85.3*exp(-(wave_bkgd-154)/66.2);
skin_bkgd_mua2=7.84e8.*wave_bkgd.^(-3.255);
net_hb=O2_frac*hb_mat(1:end,2)+(1-O2_frac)*hb_mat(1:end,3);
net_stroma=blood_frac*(net_hb)+(1-blood_frac)*skin_bkgd_mua;
hb_mat(53,1)
st_corr=(1-blood_frac)*skin_bkgd_mua(53)/net_stroma(53);
skin_bkgd_mua(53)/(net_hb(53)+skin_bkgd_mua(53));
if strcmp(model, 'ArF, cheek')==0
    figure(2)
    semilogy(hb_mat(1:end,1),hb_mat(1:end,2),'-
r',hb_mat(1:end,1),hb_mat(1:end,3),'-b',wave_bkgd,skin_bkgd_mua2,'-
g',hb_mat(1:end,1),net_stroma,'-k',hb_mat(1:end,1),net_hb,'--k')
    legend('HbO_2','Hb','tissue bkgd','net \mu_a','net Hb')
    xlabel('wavelength (nm)')
    ylabel('\mu_a (cm^{-1})')
end
if strcmp(model, 'ArF, cheek')==0
    %prepare figures of fluorescence response here
    figure(1)
    plot(NADH{1},.95*.74*NADH2,'-',FAD{1},.4*.22*FAD2,'-
',Collagen{1},.9*Collagen2*st_corr,'-',Keratin{1},.12*Keratin2,'-')
    ylabel('Normalized Fluorescence')
    xlabel('Emission Wavelength (nm)')
    legend('NADH','FAD','Collagen','Keratin','Location','NorthWest')
    %title('Fluorescent efficiency (355nm ex) of the dominant fluorophores of
the buccal epithelium')
end
end

%initialize your tissue model
if strcmp(model,'cheekd')== 1
    mods=[111/40; .3/.12; .4/.22; 95/66; 277/130; 256/320; .3/.88; .7/.9];
%layer1 thick, layer1 fluor, lay2 flour, layer3 ms, layer3 thick, layer4 ms,
layer4 fluor, layer5 fluor
    d=[mods(1)*80 80 mods(5)*120 125 10e3];
    no_layers=length(d);
    n=[1.5 1.34 1.38 1.4 1.42];           %may need a correction for wavelength
(ArF)
    g=[.97 .97 .97 .88 .88];

```

```

    qy=[.3 .4*.4 .8 .3*st_corr .7*st_corr];           %qy's for keratin, FAD,
NADH, and collagen at 355nm excitation
    f_layer={Keratin{2}; FAD{2}; NADH{2}; Collagen{2}; Collagen{2}};

draw={make_draw(Keratin{2},NADH{1}),make_draw(FAD{2},NADH{1}),make_draw(NADH{
2},NADH{1}),make_draw(Collagen{2},NADH{1}),make_draw(Collagen{2},NADH{1})};

    ms=cell(no_layers,1);           %scattering coeff for each layer
    mus_wavel=[350, 355:20:555 810];
    mus_wave2=[350, 350:50:650, 355:20:555 810];
    mus_wave3=[350, 350:50:650, 355:20:555, 488, 700, 450, 650, 633, 635,
488];
    mus_wave4=[350, 350:50:650];
    ms{1}=mus_spec(mus_wavel,[204 200 190 180 170 160 155 150 145 135 130 125
88],lambx);
    ms{2}=mus_spec(mus_wave2,[66 50 45 40 35 30 27 25 65 61 57 54 52 50 49 48
47 46 45 33],lambx);
    ms{3}=mus_spec(mus_wave4,[66 50 45 40 35 30 27 25],lambx);
    ms{4}=mus_spec(mus_wave3,[320 315 280 250 235 225 200 180 315 300 280 270
260 250 240 225 220 210 205 270 150 248.5 172 187 244 239],lambx);
    ms{5}=ms{4};
    ms{3}{2}=mods(4)*ms{3}{2};
    ms{4}{2}=mods(6)*ms{4}{2};
    figure(3)
    plot(ms{1}{1},ms{1}{2}, '-r',ms{2}{1},ms{2}{2}, '-b',ms{3}{1},ms{3}{2}, '-
g',ms{4}{1},ms{4}{2}, '-k')
    legend('super. epith.','inter. epith.','basal epith.','stroma')
    hold on
    plot(mus_wavel,[204 200 190 180 170 160 155 150 145 135 130 125 88], 'or')
    plot(mus_wave2,[66 50 45 40 35 30 27 25 65 61 57 54 52 50 49 48 47 46 45
33], 'ob')
    plot(mus_wave4,[66 50 45 40 35 30 27 25], 'og')
    plot(mus_wave3,[320 315 280 250 235 225 200 180 315 300 280 270 260 250
240 225 220 210 205 270 150 248.5 172 187 244 239], 'ok')
    xlabel('wavelength (nm)')
    ylabel('\mu_s (cm^{-1})')
    hold off

    ma=cell(no_layers,1);
    ma{1}=mua_epi([355:40:555 350:50:650],[4 3 2.5 2 1.7 1.5 4 3.2 2.5 2 1.8
1.7 1.6],lambx);
    ma{2}=ma{1};
    ma{3}=ma{1};
    ma{5}={hb_mat(1:end,1); net_stroma+4};
    %ma{4}={hb_mat(1:end,1); skin_bkgd_mua+4};
    ma{4}=ma{5};
    figure(4)
    plot(ma{1}{1},ma{1}{2}, '-r',ma{5}{1},ma{5}{2}, '-b',ma{4}{1},ma{4}{2}, '-
g')
    legend('epithelium','deep stroma','superf. stroma')
    hold on
    plot([355:40:555 350:50:650],[4 3 2.5 2 1.7 1.5 4 3.2 2.5 2 1.8 1.7
1.6], 'or')
    xlabel('wavelength (nm)')
    ylabel('\mu_a (cm^{-1})')
    axis([350 700 0 20])

```

```

hold off

d_tot=sum(d);
pho_mat_ex=zeros(width*res,round(d_tot*res),2); %use to track absorbed
weight, NEED TO ROUND THIS...
fluor_gen=zeros(width*res,round(d_tot*res));
%pho_mat_ARF=zeros(width*res,d_tot*res,5); %use to track photochemical
events
%could break these up by layers (or even further) to add resolution
%size(pho_mat_ex)
offset=find(hb_mat(1:end,1)==354); %alignment for mu_a wrt fluorescence
and mu_s
lamb_pho_model=1; %assumes everything starts as excitation

elseif strcmp(model,'cheek') == 1
d=[80 80 120 125 10e3];
no_layers=length(d);
n=[1.5 1.34 1.38 1.4 1.42]; %may need a correction for wavelength
(ArF)
g=[.97 .97 .97 .88 .88];
qy=[.12 .22*.4 .74 .88*st_corr .9*st_corr]; %qy's for keratin,
FAD, NADH, and collagen at 355nm excitation
f_layer={Keratin{2}; FAD{2}; NADH{2}; Collagen{2}; Collagen{2}};

draw={make_draw(Keratin{2},NADH{1}),make_draw(FAD{2},NADH{1}),make_draw(NADH{
2},NADH{1}),make_draw(Collagen{2},NADH{1}),make_draw(Collagen{2},NADH{1})};

ms=cell(no_layers,1); %scattering coeff for each layer
mus_wavel=[350, 355:20:555 810];
mus_wave2=[350, 350:50:650, 355:20:555 810];
mus_wave3=[350, 350:50:650, 355:20:555, 488, 700, 450, 650, 633, 635,
488];
mus_wave4=[350, 350:50:650];
ms{1}=mus_spec(mus_wavel,[204 200 190 180 170 160 155 150 145 135 130 125
88],lambx);
ms{2}=mus_spec(mus_wave2,[66 50 45 40 35 30 27 25 65 61 57 54 52 50 49 48
47 46 45 33],lambx);
ms{3}=mus_spec(mus_wave4,[66 50 45 40 35 30 27 25],lambx);
ms{4}=mus_spec(mus_wave3,[320 315 280 250 235 225 200 180 315 300 280 270
260 250 240 225 220 210 205 270 150 248.5 172 187 244 239],lambx);
ms{5}=ms{4};
figure(3)
plot(ms{1}{1},ms{1}{2},'-r',ms{2}{1},ms{2}{2},'-b',ms{3}{1},ms{3}{2},'-
g',ms{4}{1},ms{4}{2},'-k')
legend('super. epith.','inter. epith.','basal epith.','stroma')
hold on
plot(mus_wavel,[204 200 190 180 170 160 155 150 145 135 130 125 88], 'or')
plot(mus_wave2,[66 50 45 40 35 30 27 25 65 61 57 54 52 50 49 48 47 46 45
33], 'ob')
plot(mus_wave4,[66 50 45 40 35 30 27 25], 'og')
plot(mus_wave3,[320 315 280 250 235 225 200 180 315 300 280 270 260 250
240 225 220 210 205 270 150 248.5 172 187 244 239], 'ok')
xlabel('wavelength (nm)')
ylabel('\mu_s (cm^{-1})')
hold off

```

```

ma=cell(no_layers,1);
ma{1}=mua_epi([355:40:555 350:50:650],[4 3 2.5 2 1.7 1.5 4 3.2 2.5 2 1.8
1.7 1.6],lambx);
ma{2}=ma{1};
ma{3}=ma{1};
ma{5}={hb_mat(1:end,1); net_stroma+4};
%ma{4}={hb_mat(1:end,1); skin_bkgd_mua+4};
ma{4}=ma{5};
figure(4)
plot(ma{1}{1},ma{1}{2}, '-r',ma{5}{1},ma{5}{2}, '-b',ma{4}{1},ma{4}{2}, '-
g')
legend('epithelium','deep stroma', 'superf. stroma')
hold on
plot([355:40:555 350:50:650],[4 3 2.5 2 1.7 1.5 4 3.2 2.5 2 1.8 1.7
1.6], 'or')
xlabel('wavelength (nm)')
ylabel('\mu_a (cm^{-1})')
axis([350 700 0 20])
hold off

d_tot=sum(d);
pho_mat_ex=zeros(width*res,round(d_tot*res),2); %use to track absorbed
weight, NEED TO ROUND THIS...
fluor_gen=zeros(width*res,round(d_tot*res));
%pho_mat_ARF=zeros(width*res,d_tot*res,5); %use to track photochemical
events
%could break these up by layers (or even further) to add resolution
%size(pho_mat_ex)
offset=find(hb_mat(1:end,1)==354); %alignment for mu_a wrt fluorescence
and mu_s
lamb_pho_model=1; %assumes everything starts as excitation

elseif strcmp(model,'cheekb')== 1
mods=[2; 120/100; 100/130; .17/.22; .15/.74; .15/.88; .15/.9]; %th1 th2
th3 f2 f3 f4 f5
d=[mods(1)*80 mods(2)*80 mods(3)*120 125 10e3];
no_layers=length(d);
n=[1.5 1.34 1.38 1.4 1.42]; %may need a correction for wavelength
(ArF)
g=[.97 .97 .97 .88 .88];
qy=[.12 .17*.4 .15 .15*st_corr .15*st_corr]; %qy's for keratin,
FAD, NADH, and collagen at 355nm excitation
f_layer={Keratin{2}; FAD{2}; NADH{2}; NADH{2}; Collagen{2}};

draw={make_draw(Keratin{2},NADH{1}),make_draw(FAD{2},NADH{1}),make_draw(NADH{
2},NADH{1}),make_draw(Collagen{2},NADH{1}),make_draw(Collagen{2},NADH{1})};

ms=cell(no_layers,1); %scattering coeff for each layer
mus_wavel=[350, 355:20:555 810];
mus_wave2=[350, 350:50:650, 355:20:555 810];
mus_wave3=[350, 350:50:650, 355:20:555, 488, 700, 450, 650, 633, 635,
488];
mus_wave4=[350, 350:50:650];
ms{1}=mus_spec(mus_wavel,[204 200 190 180 170 160 155 150 145 135 130 125
88],lambx);

```

```

ms{2}=mus_spec(mus_wave2,[66 50 45 40 35 30 27 25 65 61 57 54 52 50 49 48
47 46 45 33],lambx);
ms{3}=mus_spec(mus_wave4,[66 50 45 40 35 30 27 25],lambx);
ms{4}=mus_spec(mus_wave3,[320 315 280 250 235 225 200 180 315 300 280 270
260 250 240 225 220 210 205 270 150 248.5 172 187 244 239],lambx);
ms{5}=ms{4};
figure(3)
plot(ms{1}{1},ms{1}{2}, '-r',ms{2}{1},ms{2}{2}, '-b',ms{3}{1},ms{3}{2}, '-
g',ms{4}{1},ms{4}{2}, '-k')
legend('super. epith.','inter. epith.','basal epith.','stroma')
hold on
plot(mus_wave1,[204 200 190 180 170 160 155 150 145 135 130 125 88], 'or')
plot(mus_wave2,[66 50 45 40 35 30 27 25 65 61 57 54 52 50 49 48 47 46 45
33], 'ob')
plot(mus_wave4,[66 50 45 40 35 30 27 25], 'og')
plot(mus_wave3,[320 315 280 250 235 225 200 180 315 300 280 270 260 250
240 225 220 210 205 270 150 248.5 172 187 244 239], 'ok')
xlabel('wavelength (nm)')
ylabel('\mu_s (cm^{-1})')
hold off

ma=cell(no_layers,1);
ma{1}=mua_epi([355:40:555 350:50:650],[4 3 2.5 2 1.7 1.5 4 3.2 2.5 2 1.8
1.7 1.6],lambx);
ma{2}=ma{1};
ma{3}=ma{1};
ma{5}={hb_mat(1:end,1); net_stroma+4};
%ma{4}={hb_mat(1:end,1); skin_bkgd_mua+4};
ma{4}=ma{5};
figure(4)
plot(ma{1}{1},ma{1}{2}, '-r',ma{5}{1},ma{5}{2}, '-b',ma{4}{1},ma{4}{2}, '-
g')
legend('epithelium',' deep stroma', 'superf. stroma')
hold on
plot([355:40:555 350:50:650],[4 3 2.5 2 1.7 1.5 4 3.2 2.5 2 1.8 1.7
1.6], 'or')
xlabel('wavelength (nm)')
ylabel('\mu_a (cm^{-1})')
axis([350 700 0 20])
hold off

d_tot=sum(d);
pho_mat_ex=zeros(width*res,round(d_tot*res),2); %use to track absorbed
weight, NEED TO ROUND THIS...
fluor_gen=zeros(width*res,round(d_tot*res));
%pho_mat_ARF=zeros(width*res,d_tot*res,5); %use to track photochemical
events
%could break these up by layers (or even further) to add resolution
%size(pho_mat_ex)
offset=find(hb_mat(1:end,1)==354); %alignment for mu_a wrt fluorescence
and mu_s
lamb_pho_model=1; %assumes everything starts as excitation
elseif strcmp(model, 'test') ==1
d=[10e3];
width=100e3;
res=.1;

```

```

d_tot=sum(d);
no_layers=length(d);
n=[1];          %may need a correction for wavelength (ArF)
nfluor=1;
g=[.8];
ma=cell(no_layers,1);
ms=cell(no_layers,1);
ma{1}={ [355 355]; [.1 .1] };
ms{1}={ [355 355]; [10 10] };
offset=0;
lamb_pho_model=2;      %assumes everything starts as excitation
pho_mat_ex=zeros(width*res,round(d_tot*res));
pho_mat_ARF=pho_mat_ex;
elseif strcmp(model, 'test2') ==1
d=[10e3];
width=100e3;
res=.1;
d_tot=sum(d);
no_layers=length(d);
n=[1.37];          %may need a correction for wavelength (ArF)
nfluor=1;
g=[.8];
ma=cell(no_layers,1);
ms=cell(no_layers,1);
ma{1}={ [355 355]; [.1 .1] };
ms{1}={ [355 355]; [10 10] };
offset=0;
lamb_pho_model=2;      %assumes everything starts as excitation
pho_mat_ex=zeros(width*res,round(d_tot*res));
pho_mat_ARF=pho_mat_ex;
elseif strcmp(model, 'ArF, cheek')==1
%setup for cheek
d=[80 80 120 125 10e3];
d_tot=sum(d);
no_layers=length(d);
n=[1.5 1.34 1.38 1.4 1.42];          %may need a correction for wavelength
(ArF)
g=[.97 .97 .97 .88 .88];          %may be able to estimate a correction
or better values
nfluor=nARF;

mus_wave1=[350, 355:20:555 810];
mus_wave2=[350, 350:50:650, 355:20:555 810];
mus_wave3=[350, 350:50:650, 355:20:555, 488, 700, 450, 650, 633, 635,
488];
mus_wave4=[350, 350:50:650];

ma=cell(no_layers,1);
ms=cell(no_layers,1);
ms193_1=ms193(6000,mus_wave1,[204 200 190 180 170 160 155 150 145 135 130
125 88]);
ms193_2=ms193(8000,mus_wave2,[66 50 45 40 35 30 27 25 65 61 57 54 52 50
49 48 47 46 45 33]);
ms193_3=ms193(8000,mus_wave4,[66 50 45 40 35 30 27 25]);
ms193_4=ms193(1000,mus_wave3,[320 315 280 250 235 225 200 180 315 300 280
270 260 250 240 225 220 210 205 270 150 248.5 172 187 244 239]);

```

```

    ma{1}={ [193 193]; [6000 6000] }; %except theres no melanin unlike in the
SC...
    ms{1}={ [193 193]; [ms193_1{1} ms193_1{1}] };
    ma{2}={ [193 193]; [8000 8000] };
    ms{2}={ [193 193]; [ms193_2{1} ms193_2{1}] };
    ma{3}={ [193 193]; [8000 8000] };
    ms{3}={ [193 193]; [ms193_3{1} ms193_3{1}] };
    ma{4}={ [193 193]; [1000 1000] };
    ms{4}={ [193 193]; [ms193_4{1} ms193_4{1}] };
    ma{5}={ [193 193]; [1000 1000] };
    ms{5}={ [193 193]; [ms193_4{1} ms193_4{1}] };
    offset=0;
    lamb_pho_model=2; %assumes everything starts as excitation
    pho_mat_ex=zeros(width*res,round(d_tot*res));
    arf_gen=zeros(width*res,round(d_tot*res),2);
    %pho_mat_ARF=zeros(width*res,d_tot*res,5); %use to track photochemical
events
    photochem_pho=zeros(no_pho,8); %first 5 are flags for pc events, x, y,
layer
else
    'ERROR- invalid model name'
    return
end
ma{1}{1}(1+offset)
ma{1}{2}(1+offset)
ma{2}{2}(1+offset)
ma{3}{2}(1+offset)
ma{4}{2}(1+offset)
ma{5}{2}(1+offset)
%
% ms{1}{1}(1)
% ms{1}{2}(1)
% ms{2}{2}(1)
% ms{3}{2}(1)
% ms{4}{2}(1)
% ms{5}{2}(1)
%initialize your disease model

%initialize collection vectors
reflect=zeros(no_pho,3); %weight, position, and angle respectively
return_check=zeros(no_pho,1); %check vector for photons that didnt violate
any rules or die
new_pho_check=zeros(no_pho,1); %check for fluorescent photons that made it
out
fluor_pho=zeros(no_pho,5); %weight, wavelength, position, angle, (layer
generated to come...)
%fluor_gen=pho_mat_ex; %track where fluorescence is generated
%pho_mat_ex=zeros(width*res,d_tot*res);
layer_vec=ones(sum(d)*res,1); %ALSO NEED TO ROUND THIS
d2=cumsum(d);
d3=[0 d2(1:(end-1))];
for i=1:(no_layers-1)
    layer_vec((res*d2(i)+1):end)=1+layer_vec(((res*d2(i))+1):end); %COULD
ALSO BE PROBLEMATIC BC OF ROUNDING
end

```

```

%initialize sim param
cutoff=1e-4; %cutoff for playing roulette
x=0;
y=0;
angle=0;
W=1;
lamb_pho=lamb_pho_model; %assumes everything starts as excitation
f_layer_hold=-1;

%lauch a photon
for i=1:no_pho
    %i
    %from where and at what angle?
    if isempty(bean)
        %pencil beam, everything starts in the middle
        nfluor=1;
        x=width/2;
        y=0;
        angle=0;
        %angle=launch_angle(NA,n(1));
    elseif strcmp(bean,'diffuse')
        %point source at the surface
        nfluor=1;
        y=0.1;
        x=width/2;
        angle=(2*round(rand)-1)*180*rand;
    else
        %use the model that was loaded and draw from that distribution
        angle=launch_angle(NA,n(1));
        %angle=(2*round(rand)-1)*89*rand;
        %angle=0;
        y=0;
        beamw=1000;
        if strcmp(model,'ArF, cheek')==1
            x=(2*round(rand)-1)*.5*beamw*sqrt(rand)+.5*width;
        else
            x=(2*round(rand)-1)*.5*beamw*sqrt(rand)+.5*width;
        end
    end
    %with what weight and wavelength?
    W=1;
    lamb_pho=lamb_pho_model;
    f_layer_hold=-1;

    %did it make it into the top layer?
    start_check=fresnel(nfluor,n(1),angle);
    if start_check{2,1} == 1 && strcmp(bean,'diffuse')==0 %then your photon
was rejected, dont check for a sub-surface pt source
        reflect(i,1)=W;
        reflect(i,2)=x;
        reflect(i,3)=angle;
        %'rejection'
    else %photon will propagate
        while W > 0
            %is my weight large enough, or do I play roulette?

```

```

if abs(angle)>180
    input('ERROR angle out of range, Enter to continue')
end
if W < cutoff
    %'play roulette'
    m=10; %or should this be indep of cutoff?
    roul=rand;
    if roul < (1/m)
        %photon survives w weight mW
        W=m*W;
    else
        %photon is terminated
        W=0;
        break
    end
end
%find my layer
layer=layer_vec(round(res*y)+1);
%lets make a move to my next scattering event
dep_x2=round(res*x)+1;
depy2=round(res*y)+1;
if dep_y2<=size(mask_mu,2) && isempty(mask_mu)==0 && y>0 &&
(strcmp(model,'cheek')==1 || strcmp(model,'cheekd')==1 ||
strcmp(model,'cheekb')==1)
    s=-
log(rand)./(ms{layer}{2}(lamb_pho)+mask_mu(dep_x2,depy2)*ma{layer}{2}(lamb_pho
+offset));
else
    s=-
log(rand)./(ms{layer}{2}(lamb_pho)+ma{layer}{2}(lamb_pho+offset));
end
x_new=x+s*1e4*sind(angle);%convert from cm to um
y_new=y+s*1e4*cosd(angle);
%did i go out of bounds?
if (x_new*res+1)>=(width*res) || (x_new*res+1)<=1 ||
(y_new*res+1)>=(d_tot*res)
    W=0;
    %'photon out of bounds'
    break
end
%did I try and escape?
if y_new <= 0
    escape_check=fresnel(n(1),nfluor,angle);
    if escape_check{1,1}==1
        %photon escaped, but was bent
        return_check(i)=1;
        fluor_pho(i,1)=W;
        fluor_pho(i,2)=lamb_pho;
        fluor_pho(i,3)=(x+x_new)/2;
        fluor_pho(i,4)=escape_check{2,1};
        fluor_pho(i,5)=f_layer_hold;
        if lamb_pho>1 && (strcmp(model,'cheek')==1 ||
strcmp(model,'cheekd')==1 || strcmp(model,'cheekb')==1)
            fluor_pho(i,6)=ma{f_layer_hold}{2}(lamb_pho+offset);
        end
        W=0;
        if lamb_pho > 1

```

```

        new_pho_check(i,1)=1;
    end
    %'photon heads out'
    break
else
    %photon reflected back in so update the position
    y_new=2*0-s*1e4*cosd(angle)-y;
    %'reflection at top'
    angle=escape_check{2,2};
end
%did i change layers or reflect off the boundary?
elseif ((y_new>d2(layer) && y<d2(layer)) || (y_new<d3(layer) &&
y>d3(layer))) && no_layers>1
    new_layer=layer_vec(round(res*y_new)+1);%into which layer?
    ref_check=fresnel(n(layer),n(new_layer),angle);
    if ref_check{1,1}==1
        %photon migrated, but was bent
        if layer > new_layer% then y_layer < y && y_new < y_layer
            %assume refraction is small deflection and just
            %update angle
            dy=abs(s*1e4*cosd(angle));%suggested dy
            dy_layer=abs(y-d3(layer));%move to the boundary
            frac=dy_layer/dy;
            s2=frac*s*1e4;
            x_layer=s2*sin(angle)+x;
            angle=ref_check{1,2};
            x_new=x_layer+(s*1e4-s2)*sin(angle);
            y_new=d3(layer)-abs((s*1e4-s2)*cos(angle));
        end
        if layer < new_layer% then y_layer > y && y_new > y_layer
            dy=abs(s*1e4*cosd(angle));%suggested dy
            dy_layer=abs(y-d2(layer));%move to the boundary
            frac=dy_layer/dy;
            s2=frac*s*1e4;
            x_layer=s2*sin(angle)+x;
            angle=ref_check{1,2};
            x_new=x_layer+(s*1e4-s2)*sin(angle);
            y_new=d2(layer)+abs((s*1e4-s2)*cos(angle));
        end
        layer=new_layer;
    else
        %photon reflected back in so update the position
        if layer > new_layer
            y_new=2*d3(layer)-s*1e4*cosd(angle)-y;
            angle=ref_check{2,2};
            %'bounced off of a layer coming back, angle should
point in, abs<90'
        end
        if layer < new_layer
            y_new=2*d2(layer)-s*1e4*cosd(angle)-y;
            angle=ref_check{2,2};
            %'bounced off of a layer going in, angle should point
out, abs>90'
        end
    end
end
end
%need one more check for exiting

```

```

if y_new<=0
    %made it out by bouncing off of another boundary
    return_check(i)=1;
    fluor_pho(i,1)=W;
    fluor_pho(i,2)=lamb_pho;
    fluor_pho(i,3)=(x+x_new)/2;
    fluor_pho(i,4)=angle;
    fluor_pho(i,5)=f_layer_hold;
    if lamb_pho>1 && (strcmp(model,'cheek')==1 ||
strcmp(model,'cheekd')==1 || strcmp(model,'cheekb')==1)
        fluor_pho(i,6)=ma{f_layer_hold}{2}(lamb_pho+offset);
    end
    W=0;
    if lamb_pho > 1
        new_pho_check(i,1)=1;
    end
    %'photon heads out'
    break
end
%need one last check to see if it exited the tissue via the
%sides
if (x_new*res+1)>=(width*res) || (x_new*res+1)<=1 ||
(y_new*res+1)>=(d_tot*res)
    W=0;
    %'photon out of bounds'
    break
end
%lets update our weight and deposit some weight in the new
%position
dep_x=round(res*x_new)+1;
dep_y=round(res*y_new)+1;
if dep_y<=size(mask_mu,2) && isempty(mask_mu)==0

dW=W.*ma{layer}{2}(lamb_pho)*mask_mu(dep_x,dep_y)./(ms{layer}{2}(lamb_pho)+mask
_mu(dep_x,dep_y)*ma{layer}{2}(lamb_pho+offset));
else

dW=W.*ma{layer}{2}(lamb_pho)./(ms{layer}{2}(lamb_pho)+ma{layer}{2}(lamb_pho+o
ffset));
end
if (strcmp(model,'cheek')==1 || strcmp(model,'cheekd')==1 ||
strcmp(model,'cheekb')==1)
    if dep_y<=size(mask_mu,2) && isempty(mask_mu)==0

pho_mat_ex(dep_x,dep_y,1)=pho_mat_ex(dep_x,dep_y,1)+(dW./(mask_mu(dep_x,dep_y)*ma{l
ayer}{2}(lamb_pho+offset)));
else

pho_mat_ex(dep_x,dep_y,1)=pho_mat_ex(dep_x,dep_y,1)+(dW./(ma{layer}{2}(lamb_pho+o
ffset)));
end
pho_mat_ex(dep_x,dep_y,2)=pho_mat_ex(dep_x,dep_y,2)+dW;
else
pho_mat_ex(dep_x,dep_y)=pho_mat_ex(dep_x,dep_y)+dW;
end
W=W-dW;

```

```

        %otherwise lets update my position and angle (via scattering) and
get ready to
        %do it again
        nu=.5/g(layer).*(1+g(layer).^2-(1-g(layer).^2).^2.*(1-
g(layer)+2*g(layer)*rand).^(-2));
        dangle=(2*round(rand)-1).*acosd(nu);
        angle=angle+dangle;
        if strcmp(model, 'ArF, cheek')==1%bc rayleigh scattering is
isotropic
            angle=180*rand*(2*round(rand)-1);
        end
        %did i fluoresce?
        %make sure to load new vectors of optical properties for me
        if lamb_pho==1%still excitation so now test to see if
fluorescence happens
            if depy<=size(mask_mu,2) && isempty(mask_mu)==0
                fluor_check=pfluor(mask_f(depx,depy)*f_layer{layer},
mask_mu(depx,depy)*ma{layer}{2}(lamb_pho+offset),
NADH{1},draw{layer},mask_f(depx,depy)*qy(layer),ms{layer}{2}(lamb_pho));
            else
                fluor_check=pfluor(f_layer{layer},
ma{layer}{2}(lamb_pho+offset),
NADH{1},draw{layer},qy(layer),ms{layer}{2}(lamb_pho));
            end
            if fluor_check{1,1}==1%then fluorescence happend
                lamb_pho=fluor_check{2,2};
                angle=180*rand*(2*round(rand)-1);
                fluor_gen(depx,depy)=fluor_gen(depx,depy)+W;
                f_layer_hold=layer;
                %input('Fluorescence!, click to continue')
            end
        end
    end
%
    if strcmp(model, 'ArF, cheek')==1%check to see if a
photochemical event happend
%
        ArF_check=pArF(layer, W, ma{layer}{2}(2), ms{layer}{2}(2));
%
        if ArF_check{1,1}==1
%
            photochem_pho(i,1)=ArF_check{1};
%
            photochem_pho(i,2)=ArF_check{2};
%
            photochem_pho(i,3)=ArF_check{3};
%
            photochem_pho(i,4)=ArF_check{4};
%
            photochem_pho(i,5)=ArF_check{5};
%
            photochem_pho(i,6)=x_new;
%
            photochem_pho(i,7)=y_new;
%
            photochem_pho(i,8)=layer;
%
            arf_gen(depx,depy,1)=arf_gen(depx,depy,1)+ArF_check{4};
%
            arf_gen(depx,depy,2)=arf_gen(depx,depy,2)+ArF_check{5};
%
            W=0;
%
            break
%
        end
%
    end
    if abs(angle)>180
        %preserves the +/-180 convention
        angle=-(360-abs(angle))*angle/abs(angle);
        %input('angle error found, was it resolved?')
    end
    x=x_new;
    y=y_new;

```

```

        end;
    end

end

%volume corrections to absorbed photon
%weights
x_ax=linspace(-width*1e-4/2,width*1e-4/2,width*res);%tissue width from beam
center in cm
x_ax2=linspace(-width*1e-4/2,width*1e-4/2,width*res+1);
y_ax=linspace(0,d_tot,round(d_tot*res));%tissue depth in um
dz=y_ax(2)*1e-4;%depth of a voxel in cm
delta_x_ax=abs(pi*x_ax2(2:end).^2-pi*x_ax2(1:(end-1)).^2);
%absorbed photon fraction matrix (cm-3)
dfluence=repmat(delta_x_ax,length(y_ax),1);

if strcmp(model, 'ArF, cheek')==1
    out2=cell(5,6);
    out2{1,1}=sum(pho_mat_ex(:))/no_pho;
    out2{1,3}=out2{1,1}*5.5e3/(5.5e3+35*3.5e4/534)*.023;
    out2{1,4}=out2{1,1}*(3.5e4*35/534)/(5.5e3+35*3.5e4/534)*(.104);
    out2{1,2}=out2{1,3}+out2{1,4};
    out2{1,5}=out2{1,4};
    out2{1,6}=out2{1,4}+35/534*out2{1,3};
    %
    out2{1,2}=sum(photochem_pho(1:end,1))/no_pho;
    %
    out2{1,3}=sum(photochem_pho(1:end,2))/no_pho;
    %
    out2{1,4}=sum(photochem_pho(1:end,3))/no_pho;
    %
    out2{1,5}=sum(photochem_pho(1:end,4))/no_pho;
    %
    out2{1,6}=sum(photochem_pho(1:end,5))/no_pho;

    %
    for i=2:5
    %
        for j=1:6
    %
            if j==1
    %
                if i==5
    %
                    out{i,j}=sum(sum(pho_mat_ex(1:end,(res*d3(i-
1)+1):(res*d2(i)))))/no_pho;
    %
                else
    %
                    out{i,j}=sum(sum(pho_mat_ex(1:end,(res*d3(i-
1)+1):(res*d2(i-1)))))/no_pho;
    %
                end
    %
            else
    %
                holder=photochem_pho(1:end,8).*photochem_pho(1:end,(j-1));
    %
                if i==5
    %
                    ind=find(holder>=4);
    %
                else
    %
                    ind=find(holder==(i-1));
    %
                end
    %
                out2{i,j}=length(ind)/no_pho;
    %
            end
    %
        end
    %
    end
    %
    end
    %
    specular=sum(reflect(1:end,1))
    %
    weight_out=sum(fluor_pho(1:end,1))
    %
    photochem=sum(photochem_pho(1:end,1))
    %
    peptides_broken=sum(photochem_pho(1:end,2))

```

```

% aromatics_aas_broken=sum(photochem_pho(1:end,3))
% abs355_broken=sum(photochem_pho(1:end,4))
% fluor355_broken=sum(photochem_pho(1:end,5))
% higher_layers=length(find(photochem_pho(1:end,8)>1))

if no_pho~=0
    pho_mat_ex2=pho_mat_ex./(ma{1}{2}(1)*dz*no_pho.*dfluence');
    %fluor_gen2=fluor_gen./(dz*no_pho.*dfluence');
    figure(4)%fluence and fluence rate and transport used interchangeably
    %divide by dfluence which corrects for the radial cross-sectional
area

pcolor(1e4*x_ax(2000:3000),y_ax(1:res*d2(1)),log10(pho_mat_ex2(2000:3000,1:res*d2(1))))
    xlabel('distance from center of the source (\mum)')
    ylabel('depth in tissue (\mum)')
    %title('ArF log(Fluence) (cm^{-2}) in the Superficial Epithelium')
    shading interp;
    colorbar;
    g=get(colorbar,'YTick');
    set(colorbar,'YTickLabel',10.^g)

    figure(5)

mid_flu=(pho_mat_ex2(round(res*width*.5),1:res*d2(1))+pho_mat_ex2(round(res*width*.5)+1,1:res*d2(1))+pho_mat_ex2(round(res*width*.5)-1,1:res*d2(1))+pho_mat_ex2(round(res*width*.5)+2,1:res*d2(1))+pho_mat_ex2(round(res*width*.5)-2,1:res*d2(1)))/5;
    tot_flu=sum(pho_mat_ex2);
    size(tot_flu)
    size(y_ax(1:res*d2(1)))
    beer_flu=tot_flu(1)*exp(-1e-
4*(ma{1}{2}(1)+ms{1}{2}(1)).*y_ax(1:res*d2(1)));
    [Y,I]=max(mid_flu);
    cross_flu=pho_mat_ex2(1:end,I(1));
    plot(y_ax(1:res*d2(1)),tot_flu(1:res*d2(1)),'-
r',y_ax(1:res*d2(1)),beer_flu,'--k');
    xlabel('tissue depth (\mum)')
    ylabel('Total Fluence Rate, (cm^{-2})')
    figure(6)
    semilogy(x_ax,cross_flu,'r-')
    xlabel('radial distance from source')
    ylabel('Fluence Rate, (cm^{-2})')
    figure(7)
    semilogy(y_ax(1:res*d2(1)),tot_flu(1:res*d2(1)),'-
r',y_ax(1:res*d2(1)),beer_flu,'--k')
    xlabel('tissue depth (\mum)')
    ylabel('Fluence Rate, (cm^{-2})')
    %now adjust the mua and fluorescence response for super epithelium
    mua_old=mua_epi([355:40:555 350:50:650],[4 3 2.5 2 1.7 1.5 4 3.2 2.5
2 1.8 1.7 1.6],lambx);
    fluoro_old=Keratin;
    %mua_bkgd=0.244+85.3*exp(-(Keratin{1}-154)/66.2);
    %figure(8)

```

```

%semilogy(mua_old{1},mua_old{2},fluoro_old{1},fluoro_old{2},Keratin{1},mua_bkgd)

    %find a line of best fit to the experimental data using beer's law

temp_mask1=pho_mat_ex(1:end,1:res*d2(1))/no_pho*(3.5e4*35/534)/(5.5e3+35*3.5e4/534)*(.104);

temp_mask2=pho_mat_ex(1:end,1:res*d2(1))/no_pho*5.5e3/(5.5e3+35*3.5e4/534)*.023*35/534+pho_mat_ex(1:end,1:res*d2(1))/no_pho*(3.5e4*35/534)/(5.5e3+35*3.5e4/534)*(.104);
%
%   tm1=temp_mask1(:,1:10);
%   tm2=temp_mask2(:,1:10);
%   cut1=find(sum(tm1,2)>0);
%   cut2=find(sum(tm2,2)>0);
%   for i=1:length(cut1)
%       t=find(temp_mask1(cut1(i),:)>0);
%       if length(t)>1
%           t2=log(temp_mask1(cut1(i),t));
%           t3=-1e-4*(ma{1}{2}(1)+ms{1}{2}(1))*t/res;
%           p=polyfit(t3,t2,1);
%           fit1=exp(p(2)).*exp(-1e-4*(ma{1}{2}(1)+ms{1}{2}(1))*((1:res*d2(1))-1)/res);
%           temp_mask1(cut1(i),:)=fit1;
%       else
%           fit1=temp_mask1(cut1(i),t).*exp(-1e-4*(ma{1}{2}(1)+ms{1}{2}(1))*((1:res*d2(1))-1)/res);
%           temp_mask1(cut1(i),:)=fit1;
%       end
%   end
%   for i=1:length(cut2)
%       t=find(temp_mask2(cut2(i),:)>0);
%       if length(t)>1
%           t2=log(temp_mask2(cut2(i),t));
%           t3=-1e-4*(ma{1}{2}(1)+ms{1}{2}(1))*t/res;
%           p=polyfit(t3,t2,1);
%           fit1=exp(p(2)).*exp(-1e-4*(ma{1}{2}(1)+ms{1}{2}(1))*((1:res*d2(1))-1)/res);
%           temp_mask2(cut2(i),:)=fit1;
%       else
%           fit1=temp_mask2(cut2(i),t).*exp(-1e-4*(ma{1}{2}(1)+ms{1}{2}(1))*((1:res*d2(1))-1)/res);
%           temp_mask2(cut2(i),:)=fit1;
%       end
%   end
dz2=y_ax(2)*1e-6;%depth of a voxel in m
delta_x_ax2=abs(pi*1e-2*x_ax2(2:end).^2-pi*1e-2*x_ax2(1:(end-1)).^2);%radial area of a voxel in m^2
dfluence2= repmat(delta_x_ax2,length(y_ax(1:res*d2(1))),1);

k_mask1=6.022e23.*dz2.*(35/534).*ones(size(pho_mat_ex2(1:end,1:res*d2(1)))).*dfluence2';%amount of molecules
k_mask2=k_mask1;
pulse=2.4e17;%number of photons for an actual experiment
post_drop1=(k_mask1-pulse*temp_mask1)./k_mask1;%multiplier for mu_a
[row,col]=find(post_drop1<=0);
post_drop1(row,col)=0;

```

```

        post_drop2=(k_mask2-pulse*temp_mask2)./k_mask2;%multiplier for
fluorescence
        [row,col]=find(post_drop2<=0);
        post_drop2(row,col)=0;
        nf=7;
        figure(8)
%         mid_filt=filter2(ones(nf)/(nf.^2),post_drop2,'valid');
%         post_drop2(4:end-3,4:end-3)=mid_filt(1:end,1:end);
%         mid_filt=filter2(ones(nf)/(nf.^2),post_drop1,'valid');
%         post_drop1(4:end-3,4:end-3)=mid_filt(1:end,1:end);
        pcolor(post_drop1')

        shading interp
        colorbar
        out=cell(3,1);
        out{1}=post_drop1';
        out{2}=post_drop2';
        out{3}=out2;
    end

elseif strcmp(model, 'test')==1 || strcmp(model, 'test2')==1
    specular=sum(reflect(1:end,1));
    weight_out=sum(fluor_pho(1:end,1));
    drx=0:.01:(1e-4*width/2);%in cm
    delta_drx=pi*drx(2:end).^2-pi*drx(1:(end-1)).^2;
    f2=1e-4*fluor_pho(1:end,3)-(.5*width*1e-4);%convert to cm and radial
    drW=zeros((length(drx)-1),1);
    for step=1:(length(drx)-1)
        ind2=find(abs(f2)>=drx(step) & abs(f2)<drx(step+1));
        drW(step)=sum(fluor_pho(ind2,1));
    end
    drW=drW./(no_pho.*delta_drx');
%     figure(5)
%     semilogy(drx(1:(end-1)),drW,'-')
%     xlabel('distance from center of the source, r(cm)')
%     ylabel('diffuse reflectance (cm^{-2})')
%     axis tight
    out=cell(2,1);
    out{1}=drx(1:(end-1));
    out{2}=drW;
    %out{3}=weight_out./(no_pho*pi*(1e-4*.5*width).^2);
    out{3}=weight_out./no_pho;

else
    out1=cell(3,5);%things by layers
    out1{1,1}=sum(sum(pho_mat_ex(1:end,1:end,2)))/no_pho; %photons absorbed
    out1{2,1}=sum(fluor_gen(:))/no_pho; %fluorescence photons generated
    out1{3,1}=out1{2,1}./out1{1,1}; %fluor efficiency
    out2=cell(8,1);
    fr=find(fluor_pho(1:end,2)>1);
    fr2=find(fluor_pho(1:end,2)==1);
    out2{1}=sum(reflect(1:end,1))/no_pho; %total reflected off of surface, a
bit of an outlier
    out2{2}=sum(fluor_pho(1:end,1))/no_pho; %total diffuse reflectance
    out2{3}=sum(fluor_pho(fr2,1))/no_pho; %total 355 out

```

```

    out2{4}=sum(fluor_pho(fr,1))/no_pho; %total diffuse fluorescence
reflectance
    out3=cell(8,1);
    ref=sum(reflect(1:end,1));
    rem=sum(fluor_pho(1:end,1));
    out3{1}=ref/(ref+rem); %total reflected off of surface, a bit of an
outlier
    out3{2}=rem/(ref+rem); %total diffuse reflectance
    out3{3}=sum(fluor_pho(fr2,1))/(ref+rem); %total 355 out
    out3{4}=sum(fluor_pho(fr,1))/(ref+rem); %total diffuse fluorescence
reflectance
    for i=2:5%layer
        if i==5
            fr=find(fluor_pho(1:end,2)>1);
            dummy=fluor_pho(fr,[1 5]);
            fr2=find(dummy(1:end,2)>=4);
            out2{8}=sum(dummy(fr2,1))/no_pho;
            out3{8}=sum(dummy(fr2,1))/(ref+rem);
            out1{1,i}=sum(sum(pho_mat_ex(1:end,(round(res*d2(end-
2))+1):round(res*d2(end)),2)))/no_pho;
            out1{2,i}=sum(sum(fluor_gen(1:end,(round(res*d2(end-
2))+1):round(res*d2(end)))))/no_pho;
            out1{3,i}=out1{2,i}/(out1{1,i}+out1{2,i});
        else
            fr=find(fluor_pho(1:end,2)>1);
            dummy=fluor_pho(fr,[1 5]);
            fr2=find(dummy(1:end,2)==(i-1));
            out2{i+3}=sum(dummy(fr2,1))/no_pho;%sort by layer of origin for
remitted fluorescence
            out3{i+3}=sum(dummy(fr2,1))/(ref+rem);%sort by layer of origin
for remitted fluorescence
            out1{1,i}=sum(sum(pho_mat_ex(1:end,(round(res*d3(i-
1))+1):round(res*d2(i-1)),2)))/no_pho;
            out1{2,i}=sum(sum(fluor_gen(1:end,(round(res*d3(i-
1))+1):round(res*d2(i-1)))))/no_pho;
            out1{3,i}=out1{2,i}/(out1{1,i}+out1{2,i});
        end
    end
    % pho_mat_ex2=pho_mat_ex(1:end,1:end,1)./(dz*no_pho.*dfluence');%need
division by mua!!! (handled in the loop bc of fluorescence)
    % fluor_gen2=fluor_gen./(dz*no_pho.*dfluence');
    % figure(5)
    % bar([out2{1:8}])
    % %title('sources of detectable photons')
    % set(gca,'XTickLabel',{'Surface Reflected', 'Total Remittance',
'Excitation', 'Fluorescence','Super Ep Fluor','Inter Ep Fluor','Basal Ep
Fluor','Stroma Fluor'})
    % ylabel('fraction of photons launched')
    figure(6)
    Y=[out1{1,1:end};out1{2,1:end};out1{3,1:end}];
    bar(Y)
    %title('per layer fluorescence metrics')
    set(gca,'XTickLabel',{'photons absorbed', 'fluorescence generated',
'layer efficieny (gen/(abs+gen))'})
    ylabel('fraction of photons launched')
    legend('total','super ep','inter ep','basal ep','stroma')
    % figure(7)

```

```

%     bar([out3{1:8}])
%     title('sources of detectable photons')
%     set(gca,'XTickLabel',{'Surface Reflected', 'Total', 'Excitation',
'Fluorescence','Super Ep Fluor','Inter Ep Fluor','Basal Ep Fluor','Stroma
Fluor'})
%     ylabel('fraction of detectable photons')
figure(8)
X=[out2{4:8}]./[out1{2,1:end}];
bar([out1{2,1:end};out2{4:8}])
legend('total','super ep','inter ep','basal ep','stroma')
set(gca,'XTickLabel',{'fluorescence generated', 'fluorescence remitted'})
ylabel('fraction of photons launched')
%now pull spectra from the total fluor remittance and the
%layer-by-layer data (might need to widen dlambda the reduce noise
%NADH{1} are my relavent wavelengths
out4=cell(6,2);
out4{6,1}=NADH{1};
out4{6,2}=NADH{1};
spect_tot=zeros(length(NADH{1}),1);
spect1=zeros(length(NADH{1}),1);
spect2=zeros(length(NADH{1}),1);
spect3=zeros(length(NADH{1}),1);
spect4=zeros(length(NADH{1}),1);
spect_totb=zeros(length(NADH{1}),1);
spect1b=zeros(length(NADH{1}),1);
spect2b=zeros(length(NADH{1}),1);
spect3b=zeros(length(NADH{1}),1);
spect4b=zeros(length(NADH{1}),1);
for i=2:length(NADH{1})
    fr=find(fluor_pho(1:end,2)==i);%sorts by wavelengths
    spect_tot(i)=sum(fluor_pho(fr,1));
    dummy=fluor_pho(fr,[1 5 3]);
    fr1=find(dummy(1:end,2)==1);
    fr2=find(dummy(1:end,2)==2);
    fr3=find(dummy(1:end,2)==3);
    fr4=find(dummy(1:end,2)>=4);
    spect1(i)=sum(dummy(fr1,1));
    spect2(i)=sum(dummy(fr2,1));
    spect3(i)=sum(dummy(fr3,1));
    spect4(i)=sum(dummy(fr4,1));
    frb=find(abs(dummy(1:end,3))<=5000);
    dummy2=dummy(frb,[1 2]);
    spect_totb(i)=sum(dummy2(:,1));
    fr1b=find(dummy2(1:end,2)==1);
    fr2b=find(dummy2(1:end,2)==2);
    fr3b=find(dummy2(1:end,2)==3);
    fr4b=find(dummy2(1:end,2)>=4);
    spect1b(i)=sum(dummy2(fr1b,1));
    spect2b(i)=sum(dummy2(fr2b,1));
    spect3b(i)=sum(dummy2(fr3b,1));
    spect4b(i)=sum(dummy2(fr4b,1));
end
nf=7;
out4{1,1}=filter(ones(1,nf)/nf,1,spect_tot/no_pho);
out4{2,1}=filter(ones(1,nf)/nf,1,spect1/no_pho);
out4{3,1}=filter(ones(1,nf)/nf,1,spect2/no_pho);
out4{4,1}=filter(ones(1,nf)/nf,1,spect3/no_pho);

```

```

out4{5,1}=filter(ones(1,nf)/nf,1,spect4/no_pho);
out4{1,2}=filter(ones(1,nf)/nf,1,spect_totb/no_pho);
out4{2,2}=filter(ones(1,nf)/nf,1,spect1b/no_pho);
out4{3,2}=filter(ones(1,nf)/nf,1,spect2b/no_pho);
out4{4,2}=filter(ones(1,nf)/nf,1,spect3b/no_pho);
out4{5,2}=filter(ones(1,nf)/nf,1,spect4b/no_pho);
out=out4;

figure(9)

plot(NADH{1},out4{1},NADH{1},out4{2},NADH{1},out4{3},NADH{1},out4{4},NADH{1},
out4{5})
xlabel('wavelength (nm)')
ylabel('Relative Fluorescence Intensity (au)')
legend('Total','Super Ep','Inter Ep','Basal Ep','Stroma')
ylabel('fractional photon count (wrt total injected)');
axis tight
length(find(fluor_pho(:,5)==1))
length(find(fluor_pho(:,5)==2))
length(find(fluor_pho(:,5)==3))
length(find(fluor_pho(:,5)>=4))
%then fit to each layers data and sum the fits to see how it looks for
%the total spectrum

% figure(10)%fluence, in terms of photon weight currently
% x_ax=linspace(-width*1e-4/2,width*1e-4/2,width*res);
% y_ax=linspace(0,d_tot,d_tot*res);
% top=4*res*d2(4);
%
%pcolor(1e4*x_ax,y_ax(1:4*res*d2(4)),log10(medfilt2(pho_mat_ex2(1:end,1:4*res
*d2(4))'),[3,3])))
% %pcolor(1e4*x_ax,y_ax(1:top),log10(pho_mat_ex2(1:end,1:top)))
%
pcolor(1e4*x_ax,y_ax(1:round(top)),log10(filter2(ones(3)/9,pho_mat_ex2(1:end,
1:round(top)))))
% %colormap gray
% shading interp;
% colorbar;
% g=get(colorbar,'YTick');
% set(colorbar,'YTickLabel',10.^g)
% xlabel('distance from center of the source (\mum)')
% ylabel('depth in tissue (\mum)')
% %title('Total photon log(Fluence) (cm^{-2}) in the epithelium and upper
stroma')
% hold on
% plot(1e4*[x_ax(1) x_ax(end)],[d2(1) d2(1)],'k--',1e4*[x_ax(1)
x_ax(end)],[d2(3) d2(3)],'k--',1e4*[x_ax(1) x_ax(end)],[d2(2) d2(2)],'k--
',1e4*[x_ax(1) x_ax(end)],[d2(4) d2(4)],'k--',[-500 -500],[0
y_ax(round(top))], 'k--',[500 500],[0 y_ax(round(top))], 'k--')
% hold off

end
end
%this is the end of the main function

```

```

function out=fresnel(n1,n2,theta) %returns P(refraction) and
P(reflection) for propagation into 2 from 1
out=cell(2);
%first make sure the angle is usable (ie: + and less than 90)
if abs(theta)==90 || abs(theta)==270
    out{1,1}=1;
    out{2,1}=0;
    out{1,2}=theta;
elseif n1==n2
    %check for actual boundary
    out{1,1}=1;
    out{2,1}=0;
    out{1,2}=theta;%transmission at the same directional angle
    %out{2,2}=sqrt(-1);
else
    %condition theta to conform w stds for fresnel eq and snells law
    if abs(theta)>90
        thetab=180-abs(theta);
    elseif abs(theta)==180
        thetab=0;
    else
        thetab=abs(theta);
    end

    if (n1 > n2) && ~isreal(asind(n1*sind(thetab)/n2))
        %check for TIR
        out{1,1}=0;
        out{2,1}=1;
        %out{1,2}=sqrt(-1);
        if theta==0
            out{2,2}=180;
        elseif theta==180
            out{2,2}=0;
        else
            out{2,2}=theta*(180-abs(theta))/abs(theta);
        end
    else
        %actually det R and T here
        theta2b=asind(n1*sind(thetab)/n2);
        R1=((n1*cosd(thetab)-
n2*cosd(theta2b))./(n1*cosd(thetab)+n2*cosd(theta2b))).^2;
        R2=((n2*cosd(thetab)-
n1*cosd(theta2b))./(n2*cosd(thetab)+n1*cosd(theta2b))).^2;
        R=(R1+R2)/2;
        T=1-R;
        r=rand;
        if r<=R%reflection
            out{1,1}=0;
            out{2,1}=1;
        else%transmission
            out{1,1}=1;
            out{2,1}=0;
        end
        out{2,2}=theta*(180-abs(theta))/abs(theta);
        if theta > 0 && theta < 90
            out{1,2}=theta2b;
        elseif theta > 90 && theta < 180

```

```

        out{1,2}=180-theta2b;
    elseif theta > -90 && theta < 0
        out{1,2}=-theta2b;
    elseif theta > -180 && theta < -90
        out{1,2}=-(180-theta2b);
    elseif abs(theta)==0
        out{2,2}=180;
        out{1,2}=0;
    elseif abs(theta)==180
        out{2,2}=0;
        out{1,2}=180;
    end
    %now consider how to re-condition the angle to conform w the
    %direction stds of the MC code (should be done above
end
end
end

function out=fluoro_fit(wave, em, ex)
    out=cell(2,1);
    if wave(1) ~= ex
        xgrid=(wave(1):2:580)-wave(1);
        wave=wave-wave(1)+1;
        modelFun = @(p,x) p(3).*(x./p(1)).^(p(2)-1).*exp(-(x./p(1)).^p(2));
        startingVals=[10 2 1];
        coefEsts=nlinfit(wave,em,modelFun,startingVals);
        temp_em=modelFun(coefEsts,xgrid);
        buffer=length(ex:2:580)-length(xgrid);
        out{1}=ex:2:580;
        out{2}=[zeros(buffer,1); temp_em'];
    else
        wave=wave-ex+1;
        xgrid=(ex:2:580)-ex;
        modelFun = @(p,x) p(3).*(x./p(1)).^(p(2)-1).*exp(-(x./p(1)).^p(2));
        startingVals=[10 2 1];
        coefEsts=nlinfit(wave,em,modelFun,startingVals);
        temp_em=modelFun(coefEsts,xgrid);
        out{1}=ex:2:580;
        out{2}=temp_em;
    end
end

function out=mus_spec(wave, mus, ex)
    out=cell(3,1);
    xgrid=ex:2:580;
    %modelFun = @(p,x) p(1).*x.^(-p(2))+p(3).*x.^(-4);
    %startingVals=[73 .2 2e12];
    modelFun = @(p,x) p(1).*x.^(-.22)+p(2).*x.^(-4);
    startingVals=[75 2e12];
    coefEsts=nlinfit(wave,mus,modelFun,startingVals);
    out{2}=modelFun(coefEsts,xgrid);
    out{1}=xgrid;
    out{3}=[coefEsts(1) -.22 coefEsts(2) -4];
end

function out=mua_epi(wave, mua, ex)

```

```

    out=cell(3,1);
    xgrid=250:2:1000;
    modelFun = @(p,x) p(1)+p(2).*exp(-(x-p(3))./p(4));
    startingVals=[.244 85.3 154 66.2];
    coefEsts=nlinfit(wave,mua,modelFun,startingVals);
    out{1}=xgrid;
    out{2}=modelFun(coefEsts,xgrid);
    out{3}=coefEsts;
end

function out=launch_angle(NA, n)
    r=-1+2*rand;
    out=r.*asind(NA./n);
end

function out=pfluor(fluor, mua, wave, draw, qy, ms)
    out=cell(2,2);
    dy=fluor(2:end)-fluor(1:(end-1));
    dx=wave(2:end)-wave(1:(end-1));
    auc=sum(dy.*dx)/2;
    %p=auc./mua;%probability of fluorescence (or should I leave mu_a total
out of it?), account for other absorbers in this case
    p=qy*mua/(mua+ms);
    r=rand;
    if r<=p
        out{1,1}=1;
        out{2,1}=0;
        wave_new=draw(round((length(draw)-1)*rand+1));
        out{1,2}=wave_new;
        out{2,2}=find(wave==wave_new);
    else
        out{1,1}=0;
        out{2,1}=1;
    end
end

function out=make_draw(fluor, wave)%makes a distribution of wavelengths for
emission that can be drawn with "rand"
    I=find(fluor>realmin);
    [Y,I2]=min(fluor(I));
    fluor=round(fluor./Y(1));
    draw=zeros(sum(fluor),1);
    top=cumsum(fluor);
    bottom=[1,(top(1:(end-1))+1)];
    length(top)
    length(wave)
    for n=1:length(top)
        if top(n)==0
            %skip that wavelength
        else
            draw(bottom(n):top(n))=wave(n);
        end
    end
    out=draw;
end

```

```

function out=ms193(mua, wave, mus)
    out=cell(2,1);
    %implied reduced scattering coeff at 193nm, assuming penetration depth
    %of all tissues approx 1um
    %mu_eff=10e3;%cm-1 prolly only holds in the mus > mua range
    %mus_reduced=mu_eff^2/(3*mua)-mua
    p=polyfit(wave.^-4,mus,1);
    out{1}=p(1).*(193^-4)+p(2);
    out{2}=p;
end

function out=pArF(layer, W, ma, ms)
    %returns flags for any photochem being done and if the optical
    %properties (mua(355), emission from 355ex) have changed and how for
    %each
    out=cell(5,1);%flags for photochem, 193pep, 193aro, 355abs, 355fluor
    out{1}=0;
    out{2}=0;
    out{3}=0;
    out{4}=0;
    out{5}=0;
    p_pchem=W*ma/(ma+ms);
    r=rand;
    if r<=p_pchem
        %some photochem was done
        out{1,1}=1;
        %now figure out what happened
        r2=rand;
        if layer==1%keratin
            p_aro_k=35/534;
            if r2<=p_aro_k
                out{3,1}=1;%193aro
                out{4,1}=1;%355abs
                out{5,1}=1;%355fluor
            else
                out{2,1}=1;%193pep
                r3=rand;
                if r3<=p_aro_k
                    out{5,1}=1;%355fluor
                end
            end
        end
        elseif layer==2 || layer==3%fad & nadh but cytosolic proteins absorb
at 193 before those fluorophores
            p_aro_cyto=.1/1;
            if r2<=p_aro_cyto
                out{4,1}=1;%355abs
                out{3,1}=1;%193aro
            else
                out{2,1}=1;%193pep
            end
        elseif layer==4 || layer==4%collagen (20%) and other proteins (5%)
and 75% water
            p_coll=20/(20+5);
            if r2<=p_coll
                p_crosslink=.2;%??? Need a reference for this
                r3=rand;
                if r3<=p_crosslink

```

```

        out{4,1}=1;%355abs
        out{5,1}=1;%355fluor
    else
        p_aro_coll=.1/1;%??? need a ref for this
        r3=rand;
        if r3<=p_aro_coll
            out{4,1}=1;%355abs
            out{3,1}=1;%193aro
        else
            out{2,1}=1;%193pep
        end
    end
else
    p_aro_cyto=.1/1;
    r3=rand;
    if r3<=p_aro_cyto
        out{4,1}=1;%355abs
        out{3,1}=1;%193aro
    else
        out{2,1}=1;%193pep
    end
end
end
else
    out{1,1}=0;
    out{2,1}=0;
    out{3,1}=0;
    out{4,1}=0;
    out{5,1}=0;
end
end
end

```

## LIST OF REFERENCES

1. M. C. Skala, G. M. Palmer, C. Zhu, Q. Liu, K. M. Vrotsos, C. L. Marshek-Stone, A. Gendron-Fitzpatrick, and N. Ramanujam, "Investigation of fiber-optic probe designs for optical spectroscopic diagnosis of epithelial pre-cancers," *Lasers in Surgery and Medicine* **34**, 25-38 (2004).
2. S. E. Waggoner, "Cervical Cancer," *Lancet* **361**, 2217-2225 (2003).
3. M. W. Lingen, J. R. Kalmar, T. Karrison, and P. M. Speight, "Critical evaluation of diagnostic aids for the detection of oral cancer," *Oral Oncology* **44**, 10-22 (2008).
4. S. N. Rogers, J. S. Brown, J. A. Woolgar, D. Lowe, P. Magennis, R. J. Shaw, D. Sutton, D. Errington, and D. Vaughan, "Survival following primary surgery for oral cancer," *Oral Oncology* **45**, 201-211 (2009).
5. W. Saman, "Global epidemiology of oral and oropharyngeal cancer," *Oral Oncology* **45**, 309-316 (2009).
6. R. Sankaranarayanan, K. Dinshaw, B. M. Nene, K. Ramadas, P. O. Esmay, K. Jayant, T. Somanathan, and S. Shastri, "Cervical and oral cancer screening in India," *Journal of Medical Screening* **13**, 35-38 (2006).
7. C. A. Squier, and M. J. Kremer, "Biology of Oral Mucosa and Esophagus," *J Natl Cancer Inst Monogr* **29**, 7-15 (2001).
8. T. A. Winning, and G. C. Townsend, "Oral mucosa embryology and histology," *Clinics in Dermatology* **18**, (2000).
9. I. Pavlova, C. R. Weber, R. A. Schwarz, M. D. Williams, A. M. Gillenwater, and R. Richards-Kortum, "Fluorescence Spectroscopy of Oral Tissue: Monte Carlo Modeling with Site-Specific Tissue Properties," *Journal of Biomedical Optics* **14**, (2009).
10. D. R. Eyre, M. A. Paz, and P. M. Gallop, "Cross-linking in collagen and elastin," *Ann Rev Biochem* **53**, 717-748 (1984).
11. L. J. Kleinsmith, *Principles of Cancer Biology* (Benjamin Cummings, San Francisco, 2006).
12. "WHO Collaborating Centre for Oral Precancerous Lesions. Definition of leukoplakia and related lesions: an aid to studies on oral precancer," *Oral Surg Oral Med Oral Pathol* **46**, 518-539 (1978).

13. L. L. Patton, J. B. Epstein, and A. R. Kerr, "Adjunctive Techniques for Oral Cancer Examination and Lesion Diagnosis: A Systemic Review of the Literature," *Journal of the American Dental Association* **139**, 896-905 (2008).
14. V. Thomas, S. R. Devi, V. Jeyaseelan, and L. Jeyseelan, "Mucosal Disorders with Oral Epithelial Dysplasia risk- Development of a simple screening tool for general health care setting," *Oral Oncology in press*, (2012).
15. P. Wilder-Smith, J. Holtzman, J. Epstein, and A. Le, "Optical diagnostics in the oral cavity: an overview," *Oral Diseases* **16**, 717-728 (2010).
16. K. Huff, P. C. Stark, and L. W. Solomon, "Sensitivity of direct tissue fluorescence visualization in screening for oral premalignant lesions in general practice," *General Dentistry*, 34-38 (2009).
17. K. H. Awan, P. R. Morgan, and S. Warnakulasuriya, "Evaluation of an autofluorescence based imaging system (VELscope) in the detection of oral potentially malignant disorders and benign keratoses," *Oral oncology* **47**, 274-277 (2011).
18. C. Scully, J. V. Bagan, C. Hopper, and J. B. Epstein, "Oral cancer: current and future diagnostic techniques," *Am J Dent* **21**, 199-209 (2008).
19. M. A. Jaber, "Oral epithelial dysplasia in non-users of tobacco and alcohol: An analysis of clinicopathological characteristics and treatment outcome," *J Oral Sci* **52**, 13-21 (2010).
20. E. L. Truelove, D. Dean, S. Maltby, M. Griffith, K. Huggins, M. Griffith, and S. Taylor, "Narrow band (light) imaging of oral mucosa in routine dental patients. Part I: Assessment of value in detection of mucosal changes," *General Dentistry*, 281-291 (2011).
21. A. J. Welch, and M. J. C. v. Gemert, *Optical-Thermal Response of Laser-Irradiated Tissue* (Springer, New York, 2011).
22. L. V. Wang, and H. I. Wu, *Biomedical Optics* (Wiley, 2007).
23. W.-F. Cheong, S. A. Prahl, and A. J. Welch, "A Review of the Optical Properties of Biological Tissues," *IEEE Journal of Quantum Electronics* **26**, 2166-2185 (1990).
24. R. Steiner, "Laser-Tissue Interactions," in *Laser and IPL Technology in Dermatology and Aesthetic Medicine*, C. Raulin, and S. Karsai, eds. (Springer-Verlag, Berlin, 2011), pp. 23-35.

25. R. Richards-Kortum, and E. Sevick-Muraca, "Quantitative Optical Spectroscopy for Tissue Diagnosis," *Annual Review of Physical Chemistry* **47**, 555-606 (1996).
26. R. Alfano, D. Tata, J. Cordero, P. Tomashefsky, F. Longo, and M. Alfano, "Laser induced fluorescence spectroscopy from native cancerous and normal tissue," *Quantum Electronics, IEEE Journal of* **20**, 1507-1511 (1984).
27. A. Policard, "Etude sur les aspects offerts par des tumeurs experimentales examinees a la lumiere de Wood," *CR Soc. Biol.* **91**, 742-743 (1924).
28. S. K. Chang, N. Marin, M. Follen, and R. Richards-Kortum, "Model-based analysis of clinical fluorescence spectroscopy for in vivo detection of cervical intraepithelial dysplasia," *Journal of Biomedical Optics* **11**, 1-12 (2006).
29. I. Pavlova, C. R. Weber, R. A. Schwarz, M. Williams, A. El-Naggar, A. Gillenwater, and R. Richards-Kortum, "Monte Carlo model to describe depth selective fluorescence spectra of epithelial tissue: applications for diagnosis of oral precancer," *Journal of Biomedical Optics* **13**, (2008).
30. C. R. Weber, R. A. Schwarz, E. N. Atkinson, D. D. Cox, C. MacAulay, M. Follen, and R. Richards-Kortum, "Model-based analysis of reflectance and fluorescence spectra for in vivo detection of cervical dysplasia and cancer," *Journal of Biomedical Optics* **13**, 1-10 (2008).
31. I. E. Kochevar, "Biological Effects of Excimer Laser Radiation," *Proceedings of the IEEE* **80**, 833-837 (1992).
32. G. H. Pettit, and M. N. Ediger, "Corneal-tissue absorption coefficients for 193- and 213-nm ultraviolet radiation," *Applied Optics* **35**, 3386-3391 (1996).
33. H. Gorner, "Photochemistry of DNA and related biomolecules: quantum yields and consequences of photoionization," *Journal of Photochemistry and Photobiology* **26**, 117-139 (1994).
34. M. Mulcahy, J. G. McInerney, D. N. Nikogosyan, and H. Gorner, "193 nm Photolysis of Aromatic and Aliphatic Dipeptides in Aqueous Solution: Dependence of Decomposition Quantum Yield on the Amino Acid Sequence," *Biol. Chem.* **381**, 1259-1262 (2000).
35. D. N. Nikogosyan, and H. Gorner, "Laser-induced photodecomposition of amino acids and peptides: extrapolation to corneal collagen," *IEEE J. Selected Topics Quantum Electron.* **5**, 1107-1115 (1999).

36. S. E. Smith, L. M. Shanyfelt, K. D. Buchanan, and D. W. Hahn, "Differential laser-induced perturbation spectroscopy using a deep-ultraviolet excimer laser," *Opt. Lett.* **36**, 2116-2118 (2011).
37. S. E. Smith, K. D. Buchanan, and D. W. Hahn, "Excimer laser-induced perturbation spectroscopy: an approach to biosensing," journal article **7674**, 767409 (2010).
38. R. T. Kozikowski, S. E. Smith, J. A. Lee, W. L. Castleman, B. S. Sorg, and D. W. Hahn, "Differential laser-induced perturbation spectroscopy: demonstration of a new spectroscopic technique in a murine model of emerging skin pathology," *Journal of Biomedical Optics* **17**, 067002 (2012).
39. M. Brownstein, R. A. Hoffman, R. Levenson, T. E. Milner, M. L. Dowell, P. A. Williams, G. S. White, A. K. Gaigalas, and J. C. Hwang, "Biophotonic Tools in Cell and Tissue Diagnostics," *Journal of Research of the National Institute of Standards and Technology* **112**, 139-152 (2007).
40. J. R. Lakowicz, *Principles of Fluorescence Spectroscopy* (Springer, New York, 2006).
41. B. W. Chwirot, M. Kowalska, N. Sypniewska, Z. Michniewicz, and M. Gradziel, "Spectrally resolved fluorescence imaging of human colonic adenomas," *Journal of Photochemistry and Photobiology B: Biology* **50**, 174-183 (1999).
42. D. C. G. De Veld, M. J. H. Witjes, H. J. C. M. Sterenberg, and J. L. N. Roodenburg, "The status of in vivo autofluorescence spectroscopy and imaging for oral oncology," *Oral oncology* **41**, 117-131 (2005).
43. J. Haringsma, and G. N. J. Tytgat, "Fluorescence and autofluorescence," *Bailliere's Clinical Gastroenterology* **13**, 1-10 (1999).
44. M. A. Funovics, R. Weissleder, and U. Mahmood, "Catheter-based in Vivo Imaging of Enzyme Activity and Gene Expression: Feasibility Study in Mice<sup>1</sup>," *Radiology* **231**, 659-666 (2004).
45. N. Ramanujam, "Fluorescence Spectroscopy of Neoplastic and Non-neoplastic Tissues," *Neoplasia* **2**, 89-117 (2000).
46. L. Gortzak-Uzan, W. Jimenez, S. Nofech-Mozes, N. Ismiil, M. A. Khalifa, V. Dubé, B. Rosen, J. Murphy, S. Laframboise, and A. Covens, "Sentinel lymph node biopsy vs. pelvic lymphadenectomy in early stage cervical cancer: Is it time to change the gold standard?," *Gynecologic Oncology* **116**, 28-32 (2010).

47. M. F. Mitchell, S. B. Cantor, N. Ramanujam, G. Tortolero-Luna, and R. Richards-Kortum, "Fluorescence Spectroscopy for Diagnosis of Squamous Intraepithelial Lesions of the Cervix," *Obstetrics & Gynecology* **93**, 462-470 (1999).
48. V. Ravery, S. Dominique, X. Panhard, M. Toubanc, L. Boccon-Gibod, and L. Boccon-Gibod, "The 20-Core Prostate Biopsy Protocol--A New Gold Standard?," *The Journal of Urology* **179**, 504-507 (2008).
49. C. Brookner, U. Utzinger, M. Follen, R. Richards-Kortum, D. Cox, and E. N. Atkinson, "Effects of biographical variables on cervical fluorescence emission spectra," *Journal of Biomedical Optics* **8**, 479-483 (2003).
50. S. F. Martin, A. D. Wood, M. M. McRobbie, M. Mazilu, M. P. McDonald, I. D. W. Samuel, and C. S. Herrington, "Fluorescence spectroscopy of an in vitro model of human cervical precancer identifies neoplastic phenotype," *International Journal of Cancer* **120**, 1964-1970 (2007).
51. A. J. Bailey, R. G. Paul, and L. Knott, "Mechanisms of maturation and ageing of collagen," *Mech Ageing Dev* **106**, 1-56 (1998).
52. K. Calabro, A. Curtis, J.-R. Galarneau, T. Krucker, and I. J. Bigio, "Gender variations in the optical properties of skin in murine animal models," *Journal of Biomedical Optics* **16**, 011008 (2011).
53. N. Kollias, R. Gillies, M. Moran, I. E. Kochevar, and R. R. Anderson, "Endogenous Skin Fluorescence Includes Bands that may Serve as Quantitative Markers of Aging and Photoaging," **111**, 776-780 (1998).
54. A. C. Meyer, B. J. Meyer, J. F. Morrison, and W. J. Pepler, "Calcium, Collagen, Elastin and hexosamine levels in the arteries of whites and Bantu," *S A Med J* **39**, 1017-1020 (1965).
55. A. Moragas, M. Garcia-Bonafe, M. Sans, N. Toran, P. Huguet, and C. Martin-Plata, "Image analysis of dermal collagen changes during skin aging," *Anal Quant Cytol Histol* **20**, 493-499 (1998).
56. T. Rechberger, K. Postawski, J. A. Jakowicki, Z. Gunja-Smith, and J. F. Woessner, "Role of fascial collagen in stress urinary incontinence," *Am J Obst Gynecol* **179**, 1511-1514 (1998).
57. S.-H. Tseng, P. Bargo, A. Durkin, and N. Kollias, "Chromophore concentrations, absorption and scattering properties of human skin in-vivo," *Opt. Express* **17**, 14599-14617 (2009).

58. D. Chakravarti, J. C. Pelling, E. L. Cavalieri, and E. G. Rogan, "Relating aromatic hydrocarbon-induced DNA adducts and c-H-ras mutations in mouse skin papillomas: The role of apurinic sites," *Proc Natl Acad Sci* **92**, 10422-10426 (1995).
59. L. Coghlan, U. Utzinger, R. Drezek, D. Heintzelmann, A. Zuluaga, C. Brookner, R. Richards-Kortum, I. Gimenez-Conti, and M. Follen, "Optimal fluorescence excitation wavelengths for detection of squamous intra-epithelial neoplasia: results from an animal model," *Opt. Express* **7**, 436-446 (2000).
60. L. Coghlan, U. Utzinger, R. Richards-Kortum, C. Brookner, A. Zuluaga, I. Gimenez-Conti, and M. Follen, "Fluorescence Spectroscopy of Epithelial Tissue Throughout the Dysplasia-Carcinoma Sequence in an Animal Model: Spectroscopic Changes Precede Morphologic Changes," *Lasers in Surgery and Medicine* **29**, 1-10 (2001).
61. O. H. Iverson, "A course of very small doses of DMBA, each of them allegedl with no promoting potency, acts with clear synergistic effect as a strong promoter of DMBA-initiated mouse skin carcinogenesis. A comparison of the tumorigenic and carcinogenic effects of DMBA (7,12-dimethylbenz-alpha-anthracene) and TPA (12-O-tetradecanoyl-phorbol-13-acetate) used as initiators and promoters in classical two-stage experimental protocols," *APMIS Suppl* **41**, 1-38 (1994).
62. X. Li, J. Eckard, R. Shah, C. Malluck, and K. Frenkel, "Interleukin-1alpha Up-Regulation In Vivo by a Potent Carcinogen 7,12-Dimethylbenz(a)anthracene (DMBA) and Control of DMBA-induced Inflammatory Responses," *Cancer Research* **62**, 417-423 (2002).
63. M. A. Nelson, B. W. Futscher, T. Kinsella, J. Wymer, and G. T. Bowden, "Detection of mutant Ha-ras genes in chemically initiated mouse skin epidermis before the development of benign tumors," *Proc Natl Acad Sci* **92**, 6398-6402 (1992).
64. M. Quintanilla, K. Brown, M. Ramsden, and A. Balmain, "Carcinogen-specific mutation and amplification of Ha-ras during mouse skin carcinogenesis," *Nature* **322**, 78-80 (1986).
65. A. C. Rencher, *Methods of Multivariate Analysis* (Wiley, New York, 1995).
66. K. Thumanu, W. Tanthanuch, D. Ye, A. Sangmalee, C. Lorthongpanich, R. Parnpai, and P. Heraud, "Spectroscopic signature of mouse embryonic stem cell-derived hepatocytes using synchrotron Fourier transform infrared microspectroscopy," *Journal of Biomedical Optics* **16**, 057005 (2011).

67. J. L. Jesneck, L. W. Nolte, J. A. Baker, C. E. Floyd, and J. Y. Lo, "Optimized approach to decision fusion of heterogeneous data for breast cancer diagnosis," *Med Phys* **33**, 2945-2954 (2006).
68. H. L. VanTrees, *Detection, Estimation, and Modulation Theory (Part I)* (Wiley, New York, 1968).
69. Z. I. Botev, J. F. Grotowski, and D. P. Kroese, "Kernel density estimation via diffusion," *Annals of Statistics* **38**, 2916-2957 (2010).
70. C. Zhu, E. S. Burnside, G. A. Sisney, L. R. Salkowski, J. M. Harter, B. Yu, and N. Ramanujam, "Fluorescence Spectroscopy: An Adjunct Diagnostic Tool to Image-Guided Core Needle Biopsy of the Breast," *IEEE Transactions on Biomedical Engineering* **56**, 2518-2528 (2009).
71. Y. Liao, L. W. Nolte, and L. M. Collins, "Decision Fusion of Ground-Penetrating Radar and Metal Detector Algorithms- A Robust Approach," *IEEE Transactions on Geoscience and Remote Sensing* **45**, 398-409 (2007).
72. G. Bottiroli, A. C. Croce, D. Locatelli, R. Marchesini, E. Pignoli, S. Tomatis, C. Cuzzoni, S. Di Palma, M. Dalfante, and P. Spinelli, "Natural fluorescence of normal and neoplastic human colon: A comprehensive "ex vivo" study," *Lasers in Surgery and Medicine* **16**, 48-60 (1995).
73. C. Eker, R. Rydell, K. Svanberg, and S. Andersson-Engels, "Multivariate analysis of laryngeal fluorescence spectra recorded in vivo," *Lasers in Surgery and Medicine* **28**, 259-266 (2001).
74. C.-Y. Wang, T. Tsai, H.-C. Chen, S.-C. Chang, C.-T. Chen, and C.-P. Chiang, "Autofluorescence spectroscopy for in vivo diagnosis of DMBA-induced hamster buccal pouch pre-cancers and cancers," *J Oral Path Med* **32**, 18-24 (2003).
75. M. F. Haque, M. Harris, S. Meghji, and A. W. Barrett, "Immunolocalization of cytokines and growth factors in oral submucous fibrosis," *Cytokine* **10**, 713-719 (1998).
76. P. Diagaradjane, M. A. Yaseen, J. Yu, M. S. Wong, and B. Anvari, "Autofluorescence Characterization for the Early Diagnosis of Neoplastic Changes in DMBA/TPA-Induced Mouse Skin Carcinogenesis," *Lasers in Surgery and Medicine* **37**, 382-395 (2005).
77. I. Pathak, N. L. Davis, Y. N. Hsiang, N. F. Quenville, and B. Palcic, "Detection of squamous neoplasia by fluorescence imaging comparing porfimer sodium fluorescence to tissue autofluorescence in the hamster cheek-pouch model," *American journal of surgery* **170**, 423-426 (1995).

78. C.-Y. Wang, C.-T. Chen, C.-P. Chiang, S.-T. Young, S.-N. Chow, and H. K. Chiang, "A Probability-based Multivariate Statistical Algorithm for Autofluorescence Spectroscopic Identification of Oral Carcinogenesis," *Photochemistry and Photobiology* **69**, 471-477 (1999).
79. G. M. Palmer, C. Zhu, T. M. Breslin, F. Xu, K. W. Gilchrist, and N. Ramanujam, "Comparison of Multiexcitation Fluorescence and Diffuse Reflectance Spectroscopy for the Diagnosis of Breast Cancer," *IEEE Transactions on Biomedical Engineering* **50**, 1233-1242 (2003).
80. N. Ramanujam, M. Follen-Mitchell, A. Mahadevan-Jansen, S. Thomsen, G. Staerckel, A. Malpica, T. Wright, N. Atkinson, and R. Richards-Kortum, "Cervical precancer detection using multivariate statistical algorithm based on laser-induced fluorescence spectra at multiple excitation wavelengths," *Photochem Photobiol* **64**, 720-735 (1996).
81. G. R. Lanckreit, T. DeBie, N. Cristianini, M. I. Jordan, and W. S. Noble, "A statistical framework for genomic data fusion," *Bioinformatics* **20**, (2004).
82. G. R. Lanckreit, M. Deng, N. Cristianini, M. I. Jordan, and W. S. Noble, "Kernel-based data fusion and its application to protein function prediction in yeast," in *Proceedings of the Pacific Symposium on Biocomputing*, (World Scientific Press, Kohala Coast, Hawaii, 2004), pp. 300-311.
83. P. Pavlidis, J. Weston, J. Cai, and W. S. Noble, "Learning gene functional classifications from multiple data types," *J Comp Biol* **9**, 401-411 (2002).
84. C. S. Herrington, and M. Wells, *Premalignant and malignant squamous lesions of the cervix* (Churchill Livingstone, Edinburgh, 2002).
85. C. Scully, and S. Porter, "ABC of oral health: swellings and red, white, and pigmented lesions," *British Medical Journal* **321**, 225-228 (2000).
86. W. G. Shafer, M. K. Hine, and B. M. Levy, *Textbook of Oral Pathology* (W. B. Saunders, Philadelphia, 1983).
87. R. Drezek, K. Sokolov, U. Utzinger, I. Boiko, A. Malpica, and M. F. R. Richards-Kortum, "Understanding the contributions of NADH and collagen to cervical tissue fluorescence spectra: Modeling, measurements, and implications," *Journal of Biomedical Optics* **6**, 385-396 (2001).
88. Q. Liu, C. Zhu, and N. Ramanujam, "Experimental validation of Monte Carlo modeling of fluorescence in tissues in the UV-visible spectrum," *Journal of Biomedical Optics* **8**, 223-236 (2003).
89. Y. Wu, and J. Y. Qu, "Combined depth- and time-resolved autofluorescence spectroscopy of epithelial tissue," *Optics Letters* **31**, 1833-1835 (2006).

90. Y. Wu, P. Xi, J. Y. Qu, T.-H. Cheung, and M.-Y. Yu, "Depth-resolved fluorescence spectroscopy of normal and dysplastic cervical tissue," *Opt. Express* **13**, 382-387 (2005).
91. D. Y. Churmakov, I. V. Meglinski, S. A. Piletsky, and D. A. Greenhalgh, "Analysis of skin tissue spatial fluorescence distribution by the Monte Carlo simulation," *Journal of Physics D* **36**, 1722-1728 (2003).
92. I. Pavlova, M. Williams, A. El-Naggar, R. Richards-Kortum, and A. Gillenwater, "Understanding the Biological Basis of Autofluorescence Imaging for Oral Cancer Detection: High Resolution Fluorescence Microscopy in Viable Tissue," *Clinical Cancer Research* **14**, 2396-2404 (2008).
93. T. Collier, M. Follen, A. Malpica, and R. Richards-Kortum, "Sources of scattering in cervical tissue: determination of the scattering coefficient by confocal microscopy," *Applied Optics* **44**, 2072-2081 (2005).
94. S. L. Jacques, "Skin Optics Summary," Oregon Medical Laser Center News, (1998).
95. I. Georgakoudi, B. C. Jacobson, M. G. Muller, E. E. Sheets, K. Badizadegan, D. L. Carr-Locke, C. P. Crum, C. W. Boone, R. R. Dasari, J. V. Dam, and M. S. Feld, "NAD(P)H and Collagen as in Vivo Quantitative Fluorescent Biomarkers of Epithelial Precancerous Changes," *Cancer Research* **62**, 682-687 (2002).
96. P. Marefaat, and G. Shklar, "Experimental production of lingual leukoplakia and carcinoma," *Oral Surg* **44**, 578-586 (1977).
97. M. C. Skala, G. M. Palmer, K. M. Vrotsos, A. Gendron-Fitzpatrick, and N. Ramanujam, "Comparison of a physical model and principal component analysis for the diagnosis of epithelial neoplasias in vivo using diffuse reflectance spectroscopy," *Optics Express* **15**, 7863-7875 (2007).
98. K. Sokolov, J. Galvan, A. Myakov, A. Lacy, R. Lotan, and R. Richards-Kortum, "Realistic three-dimensional epithelial tissue phantoms for biomedical optics," *Journal of Biomedical Optics* **7**, 148-156 (2002).
99. R. Zhang, W. Verkruyse, B. Choi, J. A. Viator, B. Jung, L. O. Svaasand, G. Aguilar, and J. S. Nelson, "Determination of human skin optical properties from spectrophotometric measurements based on optimization by genetic algorithms," *Journal of Biomedical Optics* **10**, 024030 (2005).
100. J. H. Baert, R. J. Veys, K. Ampe, and J. A. D. Boever, "The effect of sodium lauryl sulphate and triclosan on hamster cheek pouch mucosa," *Int J Exp Pathol* **77**, 73-78 (1996).

101. R. J. Veys, J. H. Baert, and J. A. D. Boever, "Histological changes in the hamster cheek pouch epithelium induced by topical application of sodium lauryl sulphate " *Int J Exp Pathol* **75**, 203-209 (1994).
102. C. M. Bishop, *Pattern Recognition and Machine Learning* (Spring Science+Business Media, Singapore, 2006).
103. T. A. Schonhoff, and A. A. Giordano, *Detection and Estimation Theory and its Applications* (Pearson Education, New Jersey, 2006).
104. G. J. Hahn, and S. S. Shapiro, *Statistical Models in Engineering* (John Wiley and Sons, New York, 1967).
105. N. L. Johnson, "Systems of frequency curves generated by methods of translation," *Biometrika* **36**, 149-176 (1949).
106. K. Tang, R. Wang, and T. Chen, "Towards Maximizing the Area Under the ROC Curve for Multi-Class Classification Problems," *Proceedings of the Twenty-Fifth AAAI Conference on Artificial Intelligence*, 483-488 (2011).
107. A. Santoro, G. Pannone, M. Contaldo, F. Sanguedolce, V. Esposito, R. Serpico, L. L. Muzio, S. Papagerakis, and P. Bufo, "A Troubling Diagnosis of Verrucous Squamous Cell Carcinoma ("the Bad Kind" of Keratosis) and the Need of Clinical and Pathological Correlations: A Review of the Literature with a Case Report," *Journal of Skin Cancer* **2011**, 1-4 (2011).

## BIOGRAPHICAL SKETCH

Raymond received his Ph.D. in the fall of 2012 from the University of Florida's J. Crayton Pruitt Department of Biomedical Engineering. While there, his research spanned multiple disciplines; fusing imaging and spectroscopy, signal processing, nanotechnology, and molecular medicine into a synergistic focus on improving cancer diagnosis and treatment. He is the recent recipient of a CIMIT Prize for Primary Healthcare Finalist Award for his work developing a new laser-based differential spectroscopy technique for diagnosing superficial cancers. Other work at Florida includes developing next-generation liposomal and polymeric nanoparticle drug formulation designed to selectively deliver therapeutic payloads in the tumor interstitium as well as describing a new functional imaging modality, blood supply time, to study how vessel growth responds to tumor formation or treatment. Before coming to UF, he worked at Advanced Liquid Logic, designing and validating of microfluidic cartridges for miniaturized point-of-care diagnostics. Prior to that, he was employed as a scientist at GlaxoSmithKline developing embedded sensing solutions for pharmaceutical manufacturing, drug discovery, and development. He received his master's and bachelor's degrees from Duke University in Electrical and Biomedical Engineering.